DEVELOPMENT OF MAGNESIUM BOROHYDRIDE ETHERATES AS HYDROGEN STORAGE MATERIALS

A DISSERTATION SUBMITTED TO THE GRADUATE DIVISION OF THE UNIVERSITY OF HAWAI'I AT MANOA IN PARTIAL FULFILLMENT OF THE REQUIREMENTS FOR THE DEGREE OF

DOCTOR IN PHILOSOPHY

IN

CHEMISTRY

December 2019

By

Phuong Quang Hoang Nguyen

Dissertation Committee:

Craig Jensen, Chairperson
John Head
Matthew Cain
Tom Autrey
Klaus Sattler

DEDICATION

I dedicate this book to those who were and have been with me on this long journey of my life, to those who inspire and continue to encourage me to pursue everything with love, passion, and enthusiasm

ACKNOWLEDGEMENT

First and foremost, I would like to thank my advisor, Professor Craig M. Jensen, for his guidance and support throughout my graduate school. I thank my committee members, Professor John Head, Professor Matthew F. Cain, Dr. Tom Autrey, and Professor Klaus Sattler for bearing with me and maintaining the high educational standards. I also want to thank our research collaborators: Dr. Bjørn Hauback, Dr. Magnus Sørby at Institute for Energy Technology; Dr. Thomas Gennett at National Renewable Energy Laboratory; Dr. Annalisa Paolone, Dr. Oriele Palumbo at National Research Council - Institute for Complex Systems, Italy; Dr. Mark Bowden at Pacific Northwest National Laboratory. Additionally, I express my thanks to all the Jensen Group members, past and present, for their guidance, advice, and friendship. I would also like to acknowledge Dr. Walter Niemczura and Wesley Yoshida for all their invaluable help with the NMR analyses. Finally, I want to thank my family, especially my parents, for supporting my education endeavors endlessly and any choices I made in this long journey.

ABSTRACT

The studies presented in this dissertation are to aim at understanding the kinetic enhancement of Lewis base THF-adduct of $Mg(BH_4)_2$ and evaluating the potential for hydrogen storage under moderate reaction conditions. The physiochemical properties of independently synthesized $Mg(BH_4)_2(THF)_x$ (x = 0.25 - 3) are studied using *in-situ* XRD and NMR spectroscopy, and differential scanning calorimetry (DSC). We find that the complex mixture undergoes solid-solid phase transformation and endothermic melting at temperature <100 ^oC. Further heating to 180 - 200 ^oC results in release of H_2 to form $MgB_{10}H_{10}$ as the major product. Using Pressure-Composition-Temperature (PCT), the reaction can be cycled between $MgB_{10}H_{10}$ and $Mg(BH_4)_2$ by maintaining the supervicous state of the material. *Ca.* 25% conversion through 3 cycles, dehydrogenation at 4 bar H_2 back pressure and rehydrogenation at 90 bar H_2, is observed. It is noted that crystallization of the dehydrogenated state at reaction times longer than 10 hours or cooling of the melt to room temperature curtails the reversibility. We also examine the role of magnesium tetrabutoxyborate, proposed to arise from the ring opening of THF by $Mg(BH_4)_2$ attack, in the reversible cycling between $MgB_{10}H_{10}$ and $Mg(BH_4)_2$. No reversibility of $MgB_{10}H_{10}$ is observed upon introducing independently synthesized $Mg[B(OBu)_4]_2$ (Bu = C_4H_9) in the hydrogenation attempts. Intrigued by the reversibility of THF-solvate $Mg(BH_4)_2$/ $MgB_{10}H_{10}$, similar approach is conducted for newly independently synthesized $MgB_{12}H_{12}(THF)_3$. No melting of $MgB_{12}H_{12}(THF)_3$ upon heating and no formation of BH_4^-, characterized by NMR analysis, is observed.

TABLE OF CONTENTS

LIST OF TABLES

LIST OF FIGURES

This page is intentionally left blank

CHAPTER 1: INTRODUCTION

1.1 Environmental Impact of Energy Consumption

The continued prosperity and economic development of the world has been linked closely to the growth in energy consumption. At present, all economic, social, and physical welfare are highly dependent on the availability of low-cost energy. In the next few decades, fossil fuels will continue to be the primary energy source driving economic development. The increasing in industrialization of developing countries such as China and India have accelerated the rate of consumption of finite supply in fossil fuels, predicted to be depleted by 2060.[1] It is projected that the world energy consumption increases from 575 quadrillion British thermal unit (Btu) in 2015 to 663 quadrillion Btu by 2030 and then to 736 quadrillion Btu by 2040. Most of the increase in energy demand is expected to come from non-OECD countries, where strong economic growth, increased access to marketed energy, and quickly growth populations leading to rising demand in energy (Figure 1.1).[2]

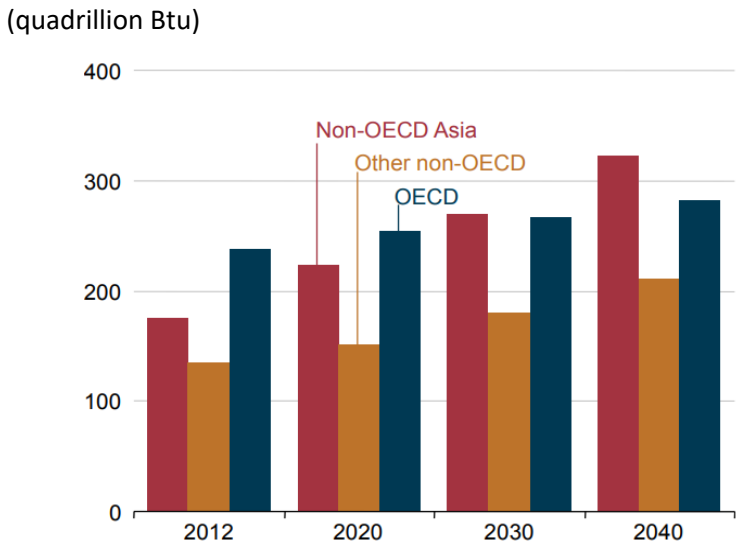

Figure 1.1: World energy consumption, 2012-2040.[2] OECD = Organization For Economic Cooperation and Development

With greater energy consumption, however, comes with the realization of the negative effects of burning fossil fuels on the environment, commonly accepted to be caused by the release of pollutants, especially carbon dioxide (CO_2). The amount of carbon on Earth is fixed and circulates in dynamic cycle, where carbon is being released into and sequestered from oceans, atmosphere, ecosystem, and geosphere. In the atmosphere, carbon is present primarily as carbon dioxide, which functions as a major greenhouse gas (GHG), absorbs the thermal radiation that reflects up into the atmosphere. As the amount of CO_2 increases, so will its warming effect. Since the early 20th century, carbon dioxide concentration level has consistently risen as a direct result of fossil fuels usage. Global average temperature, depicted as one of the most-cited indicators of global climate change, shows an increase of approximately 1.4^{o}F for the same period (Figure 1.2).[3] Impacts on climate change have already begun to affect climate patterns. These effects range in scope from sea level rise due to glacier retreat, ocean acidification, to an increase in extreme weather events.

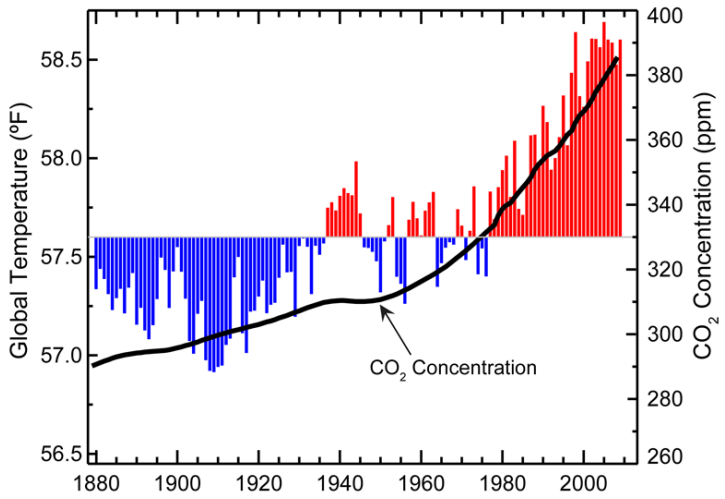

Figure 1.2: Global annual average temperature, measured overland and oceans, and carbon dioxide concentration. Red bars and blue bars indicate temperatures above and below the 1901-2000 average temperature, respectively.[3]

Clean and renewable energy sources, wind, solar, and tidal energy have the potential to outstrip the energy demand and replace fossil fuel as the primary energy source. There has been strong scientific and industrial interest in the implementation of these energy sources through development of advanced energy conversion technologies that utilizes hydrogen as a major carrier in the energy supply cycle.

1.2 Hydrogen as an Alternative Fuel

Hydrogen is the lightest and the most abundant element in the universe. It has an extremely high gravimetric density (120 MJ/kg), nearly three times larger than of gasoline (44 MJ/kg).[4] Hydrogen, however, is highly reactive and not found chemically free in nature with its availability on Earth largely in the form of water and hydrocarbons. As a result, hydrogen is not a primary energy source and must be separated from other compounds before it can act as an energy carrier. The research on hydrogen driven technologies now focuses on a wide range of developments to produce hydrogen economically and in environmentally friendly ways. At present, approximately 96% of hydrogen is produced commercially from steam reformation of natural gas as it is the most economical route from hydrocarbon feedstock (Eqn. 1.1-1.2).[24-25]

$$CH_4 + H_2O_{(g)} \longrightarrow CO + 3H_{2(g)} \quad \textbf{(1.1)}$$

$$CO + H_2O_{(g)} \longrightarrow CO_2 + H_{2(g)} \quad \textbf{(1.2)}$$

Hydrogen produced from this process, however, costs approximately three times the cost of natural gas per unit of energy produced. From the environmental perspective, increased production of H_2 by current technologies will consume greater amounts of conventional hydrocarbons, which in turn will generate greater greenhouse gas emission.

Manufacturing hydrogen from other common processes *e.g.* electrolysis, photolysis, or biochemical using renewable sources derived from agricultural or waste streams offers the possibility to the production capacity with lower greenhouse gas emission impact, poses similar cost issues and land space requirements.

Although the production of hydrogen may generate greenhouse gases, depending on the source, fuel cell vehicles (FCVs) running on hydrogen produce zero tailpipe emissions, with water vapor and warm air as exhaust. Hydrogen fuel cell vehicles, which use electric motors, are much more energy efficient (use 60% or higher of the fuel's energy) in comparison to conventional vehicle with a gasoline internal combustion engine (use less than 20% in converting the chemical energy in gasoline into power).[5] There are several different types of fuel cells but only proton exchange membrane fuel cell (PEMFC) is more suitable for transportation applications due to its low operation temperature (around 80^{o}C) which allows fast start up and results in less wear on the system components.[6,7] While significant technical advances have been made, fuel cells are currently not cost competitive with traditional power sources due to the high cost of platinum, Pt, catalyst, low durability attributed to membrane degradation, platinum particles sintering, and carbon support corrosion.[8]

1.3 Hydrogen Storage

In addition to the challenge of developing a cost-effective and environmentally friendly hydrogen production method, storing hydrogen onboard a vehicle as a gas is a key barrier to the realization of a hydrogen economy. Despite decades of extensive research effort, no material has been found which has the combination of high gravimetric and

volumetric capacities; adequate thermodynamic properties; as well as dehydrogenation and rehydrogenation kinetics that allow hydrogen cycling at moderate conditions. In recent years, the U.S. Department of Energy (US DOE) has invested significant effort in the research and development of hydrogen storage for vehicular applications and published set of important targets mainly based on present day vehicles as well as demands from the automobile industry. Technical targets include a gravimetric capacity of 4.5 wt.% and a volumetric capacity of 30 g/L for 2020 with the ultimate targets of 6.5 wt.% and 50 g/L for gravimetric volumetric densities, respectively (Table 1.1).[9] Thus, at least 5 kg of hydrogen, occupy a volume of 45 m^3 at standard temperature and pressure, STP, are needed onboard a vehicle to meet the expected 300 mile-driving range.[10]

Thermodynamic and kinetic factors determine the cycling conditions of the hydrogen storage materials. The thermodynamics of hydrogen adsorption/desorption govern their temperature and pressure range of applicability, described by pressure-composition isotherms (Figure 1.3).[15] The host material initially dissolves some hydrogen as a solid solution (α -phase), after the dissociation of molecular H_2 into atomic hydrogen at the surface of the material. As hydrogen pressure increases, the concentration of H in the metal undergoes slight increase until the nucleation process and the growth of hydride (β) phase begins. When solid solution and hydride phase coexist, a plateau pressure is observed in the isotherms; the length is determined by the concentration of hydrogen stored. In the pure β-phase, the hydrogen pressure rises steeply with the concentration. The two-phase region ends in a critical point, T_c, above which the transition from the α- to β-phase is continuous.

Table 1.1: *U.S. DOE Onboard Hydrogen Storage Targets*[9]

STORAGE PARAMETER	UNITS	2020	2025	ULTIMATE
System Gravimetric Capacity				
Usable, specific-energy from H_2 (net useful energy/max system mass)	kWh/kg (kg H_2/kg system)	1.5 (0.045)	1.8 (0.055)	2.2 (0.065)
System Volumetric Capacity				
Usable energy density from H_2 (net useful energy/max system volume)	kWh/L (kg H_2/L system)	1.0 (0.030)	1.3 (0.040)	1.7 (0.050)
Storage System Cost				
Fuel cost	$/gge at pump	4	4	4
Durability/Operability				
Min/max delivery temperature	ºC	-40/85	-40/85	-40/85
Operational cycle life (1/4 tank to full)	Cycles	1,500	1,500	1,500
Min delivery pressure from storage system	bar (abs)	5	5	5
Max delivery pressure from storage system	bar (abs)	12	12	12
Charging/Discharging Rates				
System fill time	min	3–5	3–5	3–5
Fuel Quality				
Fuel quality (H_2 from storage)	% H_2	Meet or exceed SAE J2719		
Environmental Health and Safety				
Permeation and leakage	–	Meet or exceed SAE J2579 for system safety		
Toxicity	–	Meet or exceed applicable standards		
Safety	–	Conduct and evaluate failure analysis		

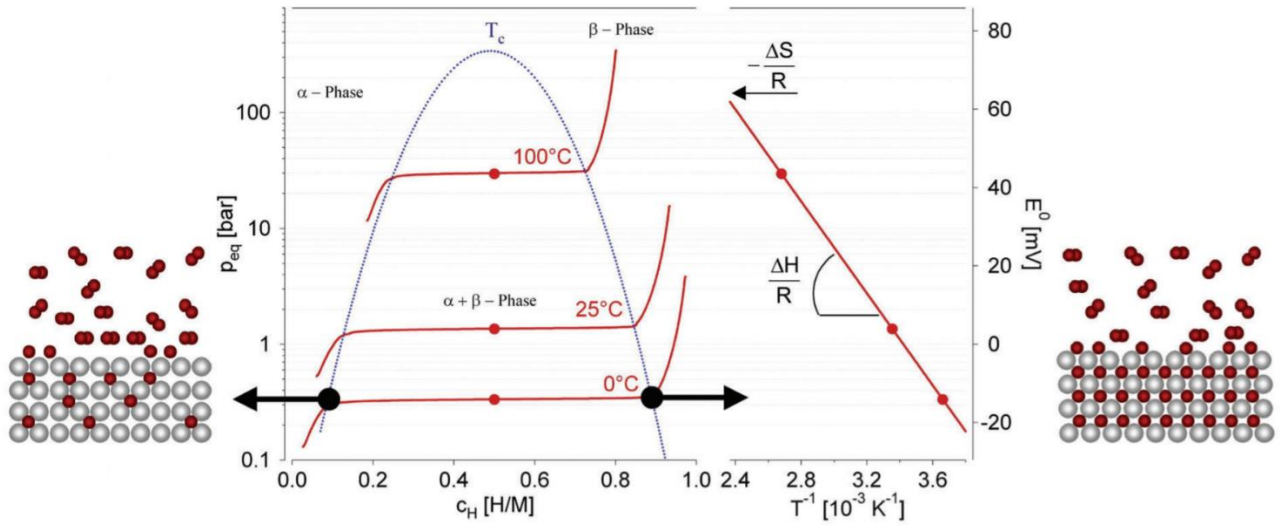

Figure 1.3: Pressure-composition isotherms (PCI) for the hydrogen absorption in a typical intermetallic compound on the left-hand side with the construction of the Van't Hoff plot on the right-hand side. H/M is the hydrogen to metal stochiometric ratio and is a measure of the amount of absorbed hydrogen. α and β are metal hydride phases, T_c is the critical temperature. The slope of the line is equal to the enthalpy of formation divided by the gas constant and the intercept is equal to the entropy of formation divided by the gas constant.[15]

A noteworthy thermodynamic property of the system is the change in free enthalpy, determining the favorability of the reaction, described by the standard equation for Gibbs free energy (Eqn. 1.3).

$$\Delta G^0 = \Delta H^0 - T\Delta S^0 \quad \textbf{(1.3)}$$

Here, ΔG is the free energy change, T is the absolute temperature, ΔH and ΔS are change in enthalpy and entropy, respectively. The equilibrium constant, K, can be calculated as shown in Eqn. 1.4, where R is the gas constant.

$$\Delta G^0 = -RT\ln K \quad \textbf{(1.4)}$$

The equilibrium constant can be further extrapolated to account for gas pressure. The equilibrium pressure (or plateau pressure, P_{eq}) is related to the changes in enthalpy and

entropy as a function of temperature by the Van't Hoff equation, where P_{eq} is the equilibrium pressure, P_0 is the atmospheric pressure (Eqn 1.5).[26]

$$\ln\left(\frac{P_{eq}}{P_0}\right) = \frac{-\Delta H}{RT} + \frac{\Delta S}{R} \qquad \textbf{(1.5)}$$

This relates the equilibrium pressure to the inverse temperature at constant hydrogen to metal concentration. With a series of equilibrium pressures at different temperature, a plot of $\ln\left(\frac{P_{eq}}{P_0}\right)$ versus $\frac{1}{T}$ will produce a straight line such that ΔH and ΔS can be determined from the slope and the y-intercept, respectively. As the entropy change corresponds mostly to the change from molecular hydrogen gas to dissolve solid hydrogen, it is approximately the standard entropy of hydrogen (S_0 = 130 J/K·mol) and is, therefore, $\Delta S_f \approx$ -130 J/K·mol H_2 for all metal-hydrogen systems.[27] The enthalpy term, ΔH, characterizes the thermochemical stability. The van' t Hoff equation dictates that for practical on-board hydrogen storage at 1-10 bar H_2 pressure, P, and fuel cell temperature, T, of 25-125 °C, the enthalpy of reaction, $\Delta_r H$, of an ideal material should be within the range of 20-50 kJ/mol H_2.[28,29] Low values represent low stability, high desorption pressures, and low temperatures. On the other hand, large values represent high stability, desorption at low pressures and high temperatures. Furthermore, if the magnitude of $\Delta_r H$ is too high, it will result in heat management problems.[30]

Thermodynamics is not the only concern for hydrogen storage materials. Kinetic factors determine how fast the de-/re-hydrogenation reactions occur, hence, governs the refueling and start up times. Having good thermodynamic parameters do not imply that a material is suitable for hydrogen storage. For example, α-AlH_3 has a highly favorable enthalpy of dehydrogenation of 7.5 kJ/mol H_2, but is kinetically sluggish, so it requires

temperature up to 100°C to achieve reasonable desorption rates.[31] Therefore, a good hydrogen storage material should possess both good kinetic and thermodynamic properties.

1.3.1 High pressure gas cylinders and cryogenic liquid hydrogen

The use of compressed natural gas fuels (250 bar) onboard vehicles is well-established and has been integrated into many commercial applications such as trucks and buses.[11] Due to relatively low energy density, however, hydrogen requires much higher pressure in order to store a sufficient amount of fuel for vehicle usage. The volumetric density of normal hydrogen as a function of pressure is depicted in Figure 1.4.[12] It is observed that hydrogen density does not follow a linear function, unlike of ideal gas, over the increase of pressure. A hydrogen density of 20 kg/m^3 is reached at 300 bar with an increase in hydrogen density up to 30 kg/m^3 at 700 bar. The most mature technology is physical storage with light weight and low volume carbon fiber-reinforced composite materials being developed to store compressed hydrogen at 700 bar. Regardless of the reduction in volume, however, compression introduces additional problems such as suitable hydrogen-inert materials for tank design, energy penalties associated with compressing the gas to very high pressure, and safety concerns to the general public with regard to rapid loss of H_2 in an accident.

A different way to store hydrogen is as a liquid at cryogenic temperature, -253°C. Liquid hydrogen has high energy density per unit volume compared to gaseous hydrogen, even at low and atmospheric pressures. Significant problems, however, including thermal insulation of storage vessel to limit liquid hydrogen boil off, liquefaction issues, and volumetric constrains limit this type of storage from widespread adaptation in automobiles.[12]

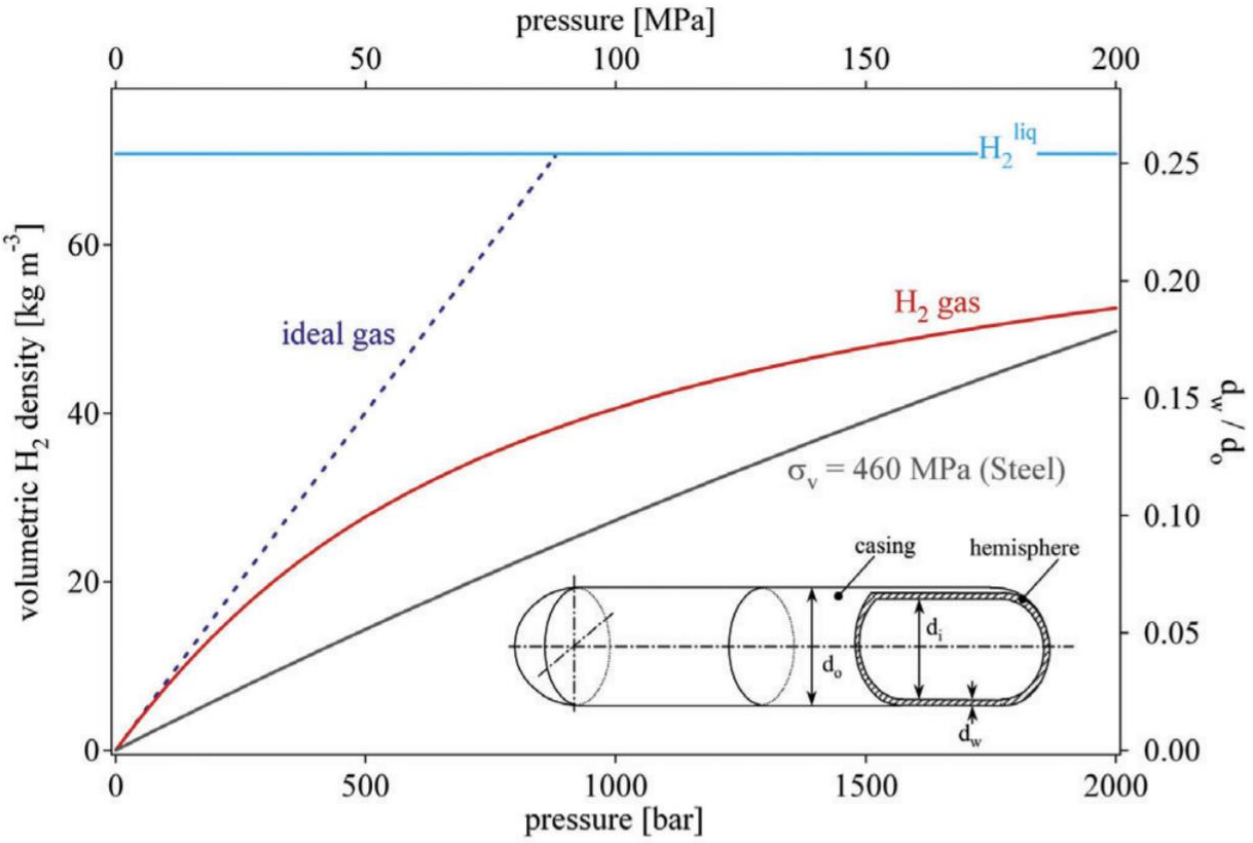

Figure 1.4: Volumetric density of compressed hydrogen gas as a function of gas pressure[12]

In light of this fact, intensive research efforts have been focused on exploring material based-hydrogen storage, since the materials have the potential to store larger quantities of hydrogen in smaller volumes at low pressures and at temperatures close to room temperature. It is also possible to achieve greater volumetric energy content relative to compressed gas or liquid.[13,14] Table 1.2 summarizes the six main methods that can be used to store hydrogen, categorized by physical-based storage to the way hydrogen is bound ranges from weak van der Waals interactions (*i.e.* physisorptive binding of molecular H_2) to the stronger chemisorptive binding of formal chemical bond between atomic hydrogen and other atoms.[15]

Table 1.2: *Basic hydrogen storage methods. The gravimetric density ρ_m, the volumetric density ρ_v, the working temperature T and pressure P are listed.*[12]

Storage Method	ρ_m (mass%)	ρ_v (kg H_2 m^{-3})	T (ºC)	P (bar)	Phenomena and remarks
High-pressure gas cylinder	13	40	RT	800	Compressed gas (molecular H_2) in lightweight composite cylinder
Liquid hydrogen in cryogenic tanks	Size dependent	70.8	-252	1	Liquid hydrogen (molecular H_2), continuous loss of a few % per day of hydrogen at RT
Adsorbed hydrogen	~2	150	RT	1	Physisorption (molecular H_2) on materials e.g. carbon with a very large specific surface area, fully reversible
Absorbed in interstitial sites in a host metal	~2	150	RT	Material dependent	Hydrogen (atomic H) intercalation in host metals, metallic hydrides working at RT are fully reversible
Complex hydride	<18	150	>100	Material dependent	Complex compounds ($[AlH_4]^-$ or $[BH_4]^-$), desorption at elevated temperature, adsorption at high pressures

1.3.2 Physisorption materials

Physisorption or adsorption of hydrogen onto the surface of materials (*i.e.* metal-organic frameworks (MOFs), activated carbons, carbon nanotubes, zeolites and clathrates), *via* dispersive van der Waals interactions and electrostatic forces, has been studied intensively in recent years. As it does not involve bulk solid diffusion or chemical dissociation, the adsorption process is completely reversible and the kinetics of the adsorption are rapid.[16,17] The binding energy of hydrogen molecule on the substrate at room

temperature, however, is very low (ΔH_{ad} of 4-10 kJ/mol^{-1}), as a result, cryogenic temperature (-196^{o}C) is required.[12,18]

For any adsorbent material, an empirical relation, Chahine rule, relates the gravimetric capacity of the material to the specific surface area so that an increase of 1 wt.% H gravimetric capacity for every 500 m^2/g of surface area, although deviation exists due to the differences in the framework density of the sorbent structures.[19-21] However, realizing high volumetric capacity, a critical attribute for maximizing driving range of fuel cell vehicles, remains a challenge and is often omitted in the characterization of porous materials.

The highest hydrogen storage capacity at room temperature in carbon nanotubes is less than 2 wt.% while the highest reported hydrogen capacity in MOF, microporous materials consisting of transition metals linked together by organic ligands, is ~7 wt.% at 77K with a room temperature capacity of ~1 wt.%.[22,23] With the low gravimetric and volumetric densities together with storage at cryogenic temperature, thus, sorbent materials fall short of the DOE targets for vehicular applications.

1.3.3 Chemical hydrogen storage

The category of chemical hydrogen storage materials generally refers covalently bound hydrogen in either solid or liquid form, in which hydrogen is generated through a chemical reaction, for example the reaction of metal hydrides with water or alcohol. These materials have unfavorable thermodynamics for reversiblity, that is, the decomposition reaction is usually exothermic; thus, re-hydrogenation typically requires the dehydrogenated product to be re-hydrogenated off-board by chemical processes other than

through the application of hydrogen pressure.[32,33] One of the chemical hydrides that has garnered a lot of attention in the recent years is ammonia borane (AB) which has very gravimetric and volumetric H_2 density (19.6 wt.% H and 120 g/L, respectively). Interest in utilization for hydrogen storage, however, has waned as its regeneration cannot be accomplished by direct hydrogenation or economical chemical process.

Recently, hydrolysis of chemical hydrides gained renewed interest as a promising on-board hydrogen storage technology. Among the chemical hydrides of interest, sodium borohydride, $NaBH_4$, receives the most extensive studies as a hydrogen generator. $NaBH_4$ is a white, hygroscopic crystalline material that is stable in a vacuum up to 400^oC, but readily undergoes hydrolysis at ambient temperature to generate hydrogen (Eqn. 1.6).[38,39]

$$NaBH_4 + 4H_2O \longrightarrow NaBO_2 \bullet 2H_2O + 4H_2 \qquad \textbf{(1.6)}$$

This reaction, which yields 10.8 wt. % H, is sensitive to pH change due to the increase in amount of $NaBO_2$ and results in decrease in reaction rate. The release rate of hydrogen, however, can be regulated by controlling the amount of solution in contact with the catalyst (e.g. Pt-$LiCoO_2$), allowing the system to meet the dynamic power demands of a fuel cell vehicle. Certain limitations such as excess water required to dissolve $NaBH_4$ and its by-product, $NaBO_2$, results in lower than the theoretical 10.8 wt.%, and uneconomical regeneration of $NaBH_4$ from the spent sodium borate through multiple chemical processes, hinder the commercial application of this system.[48]

1.3.4 Metal hydrides

Considered to be the simplest and most thoroughly studied method of storing hydrogen in solid involves the reaction of H_2 with a metal or metal alloy to form a metal hydride (Eqn. 1.7).

$$M + (x/2)\ H_2 \rightleftharpoons MH_x \qquad \textbf{(1.7)}$$

where M is a metal or alloy and MH_x is the metal hydride. Many metal hydrides are stable at ambient conditions, and the exothermic formation enthalpy for these compounds reflects the stability of metal-hydrogen bond.[15] Metal hydrides are often classified according to the nature of the bonding between hydrogen and the metal. Ionic hydrides (e.g. LiH, NaH, MgH_2, and CaH_2) are formed by alkali or alkaline earth metals. Their bonding has strong ionic character and therefore very stable. Magnesium hydride, MgH_2, has been a favored material in this class based on its high gravimetric hydrogen storage capacity (7.6 wt.% H_2) and its relatively low cost and abundance.[41] As for other potential hydrogen storage materials, unmodified MgH_2 is not suitable for on-board vehicular applications due to its high dehydrogenation enthalpy (75 kJ/mol),[42] dissociation or hydrogen release only occurs at 320 ^oC,[43] and kinetic limitation at moderate temperature and pressure,[44] While attempts to improve the kinetics of dehydrogenation by structure refinement through ball-milling[40] and alloying with transition metal catalysts[45-47] have been successful, its high enthalpy of dehydrogenation prevents its application for hydrogen storage in connection with an onboard PEM fuel cell.

Alane also attracts a lot of interest due to its high hydrogen capacity and its low decomposition temperature, gives off 10 wt.% H_2 at 100 ^oC. The main drawback to using alane in hydrogen storage applications is unfavorable hydriding thermodynamics,[31,35]

requiring impractical hydrogen pressure for direct hydrogenation. Attempt to lower the impractical high pressure needed to form alane and avoid the chemical reaction route of alane that leads to the formation of alkali halide salts highlights the reversible cycle utilizing electrochemistry.[34] Other attempt to lower hydrogenation conditions of spent Al product highlights the work in utilizing Lewis bases and TEDA to aid the formation of aluminum hydride.[36,37] Progress has been made, however, none of these processes is proven to be amiable to commercial development.

Interstitial hydrides (e.g. $LaNi_5H_6$, TiH_2, PdH_x, and $TiFeH_2$) originate from metallic bonding between hydrogen and either transition metal, a rare earth metal or metal alloy. The hydrogen occupies the interstitial sites in the metallic (alloy) matrix such that the crystal structure of the metal (alloy) does not topologically change upon hydrogen absorption. These metallic alloys can release and absorb hydrogen reversibly around ambient temperature and hydrogen pressure. Due to the presence of heavy metals in their structure, however, interstitial hydrides are limited by low gravimetric hydrogen capacity (<2.5 wt. % H_2).

1.3.5 Complex metal hydrides

Group I and II salts of $[AlH_4]^-$, $[NH_2]^-$, and $[BH_4]^-$ (alanates, amides, and borohydrides), referred to as "complex metal hydrides", although only the alanates contain anionic metal complexes, have recently received considerable attention as potential hydrogen storage materials. These materials primarily compose of light elements ($Z \leq 13$), possess high hydrogen capacities, however, the use of such materials was considered to be impractical due to their apparent irreversibility of their dehydrogenation. The three major

classes of these compounds include the alanates, the amides, and the borohydrides. The pioneering study of Bogdanovic and Schwickardi on the reversibility and kinetic improvement of alanates $[AlH_4]^-$ upon doping with titanium based compounds has drastically changed the prospects of complex metal hydrides for hydrogen storage.[50-52] Since this breakthrough, intensive research efforts have been focused on discovering new complex hydrides with favorable hydrogen storage properties and tailoring the thermodynamics and kinetics of the hydrogen sorption in existing ones.[53-56] Doping with titanium dramatically lowers the kinetic barrier to its reversible loss of hydrogen. Dehydrogenation was found to occur at 423 K and re-hydrogenation at 443 K. However, Ti-doped $NaAlH_4$ material is not suitable for practical on-board application due to its low proven cycling capacity of 4.2 wt.%. Additionally, its high enthalpy of hydrogenation (56.5 kJ/mol) makes heat rejection during rapid charging technically difficult while the kinetics observed for hydrogen release at 423K are not adequate for fully meet the demands of an operating automotive PEM fuel cell.[53,57]

In addition to $NaAlH_4$, there are numbers of other alanates that are less stable than $NaAlH_4$ and also exhibit high gravimetric hydrogen densities such as $LiAlH_4$. Thermolysis of $LiAlH_4$ is initiated by the melting of $LiAlH_4$ at 125^oC, which subsequently decomposes into solid Li_3AlH_6 and Al by the release of H_2 in the temperature range 150-220^oC (Eqn. 1.8, 1.9).[58-60] The exothermic decomposition in this first step, however, hinders the full reversibility of the system.

$$3LiAlH_4 \longrightarrow Li_3AlH_6 + 2Al + 3H_2 \quad \textbf{(1.8)}$$

$$Li_3AlH_6 \longrightarrow 3LiH + Al + \frac{3}{2}H_2 \quad \textbf{(1.9)}$$

Thus, ball milling $LiAlH_4$ as well as addition of $TiCl_3$ lowers the decomposition temperature but does not enable rehydrogenation.[62] A way to overcome the energy barrier to the re-hydrogenation of $LiAlH_4$ is to use a solvent-mediated synthesis route, hence LiH and Al stirred in, *e.g.*, THF.[63,64] However, THF binds very tightly to the Li and separation of the coordinated THF from the Ti doped $LiAlH_4$ is difficult. Jensen *et al.* found that this challenge could be overcome by using less strongly coordinating Me_2O as in place of THF.[61]

The pioneering effort of Chen *et al.* in 2002 towards the use of amide-hydride, where they observed 10.5 wt.% H_2 reversibly stored in lithium nitride, Li_3N, motivated extensive studies on the reversible hydrogen storage properties of such system (Eqn. 1.10).[62]

$$LiNH_2 + 2LiH \Leftrightarrow Li_2NH + LiH + H_2 \Leftrightarrow Li_3N + 2H_2 \quad \textbf{(1.10)}$$

The first and second reactions release 5.1 and 5.4 wt.% H_2, respectively. The decomposition reaction initiates at 180^{o}C, lower than those of the individual reactants, i.e. 300^{o}C for lithium amide, $LiNH_2$, and 600^{o}C for lithium hydride, LiH. Dehydrogenation of the imide, Li_2NH, which requires high vacuum and temperature above 600 K, and the liberation of NH_3, which leads to the contamination of fuel cells, hinder the system's practical application for reversible hydrogen storage.

1.3.5.1 Borohydrides

The final class of complex hydrides is comprised of the borohydrides, $M[BH_4]$, which possesses the highest theoretical hydrogen storage capacities of all metal hydrides. The first report of a pure alkali metal borohydride appeared in 1940 by Schlesinger and

Brown,[66] who synthesized lithium borohydride, $LiBH_4$, by the reaction of ethyl lithium with diborane, B_2H_6. Since then, many metal borohydrides have been synthesized either through the direct synthesis from an alkali or alkaline earth hydride with a triethylamine borane complex under argon atmosphere,[67,68] or through the solid-state metathesis reaction by mechanical milling of metal halides with an alkali borohydride in an inert gas atmosphere.[69,70]

In view of their high hydrogen capacities, Group I and II borohydrides have been explored as hydrogen storage materials. While the bonding within the tetrahedral BH_4^- is covalent, the bonding between the metal and the complex is ionic, resulting in thermodynamically stable compounds, thus requires high hydrogen cycling temperatures. Detailed studies on hydrogen release in borohydrides began with $LiBH_4$, possessing 18.5 wt. % H_2 in capacity, and observed to release hydrogen over multiple steps at a minimum temperature of 380°C with 4.5 wt.% of hydrogen bound as LiH in the final desorbed product (Eqn. 1.11).[71,72]

$$LiBH_4 \longrightarrow \frac{1}{12} Li_2B_{12}H_{12} + \frac{5}{6} LiH + \frac{13}{12} H_2 \longrightarrow LiH + B + \frac{3}{2} H_2 \qquad \textbf{(1.11)}$$

Partial reversibility of the dehydrogenated product from $LiBH_4$, owing to the high kinetic barrier of $Li_2B_{12}H_{12}$ toward hydrogen absorption, was reported to occur under extreme temperature (600°C) and pressure (35 MPa H_2).[56] The harsh conditions required to facilitate dehydrogenation and subsequent re-hydrogenation exemplify considerable challenges associated with the use of complex hydrides that are due to intrinsic physical barriers. Over the last decade, there has been an extensive effort to find a species with more appropriate thermodynamic properties. Researchers have focused on other Group I, II, and III salts of BH_4^-. The same considerations as for $LiBH_4$ are valid for $NaBH_4$ and KBH_4,

which possesses 10.6 and 7.4 wt.% H_2, respectively. These systems, however, have been found to require temperature higher than 430°C to facilitate complete dehydrogenation.[73]

Of the Group II metal borohydride complexes, $Be(BH_4)_2$, despite of possessing 20.8 wt.% H_2 and low decomposition temperature, is unsuitable for hydrogen storage due to its extreme toxicity and high reactivity. Other prospective borohydrides in this group are magnesium and calcium borohydrides, possess 14.8 and 11.6 wt.% H, respectively. $Ca(BH_4)_2$, formed by reacting ballmilled mixture of CaB_6 + $2CaH_2$ + 8 wt.% $TiCl_3$/Pd at 700 bar H_2 and 400°C, demonstrated a reversible capacity of 9.6 wt.% H_2.[75] In another report, $Ca(BH_4)_2$ can be re-hydrogenated under 90 bar of hydrogen at 350°C after undergoing a dehydrogenation reaction, but lower yield of $Ca(BH_4)_2$ was obtained.[76] Aluminum borohydride, $Al(BH_4)_3$, possesses 16.8 wt.% H, is a liquid and delivers hydrogen spontaneously at room temperature. Little attention has been paid to this complex hydride as hydrogen storage material due to its instability and pyrophoric nature.[53]

On the other hand, $Mg(BH_4)_2$ has been the subject of many intensive studies due to its attractive theoretical gravimetric hydrogen capacity (14.8 wt. %), higher than the targets for on-board hydrogen storage.[9] The thermodynamic dehydrogenation enthalpy and entropy of $Mg(BH_4)_2$ to MgB_2 are 38.6 kJ/mol H_2 and 111.5 J/K•mol H_2, respectively, predicting a plateau pressure of 1 bar H_2 at 73°C using van' t Hoff equation.[73,84]

The decomposition reaction pathways of $Mg(BH_4)_2$ and their mixtures have been studied extensively, however, the experimental findings are still in some discrepancies. It has been shown that the onset T_{dec} is above 200 °C if the initial phase at room temperature is α-$Mg(BH_4)_2$, β-$Mg(BH_4)_2$,[78,79,113,127] or amorphous $Mg(BH_4)_2$ synthesized from ball-milling.[112] However, a small weight loss below 200 °C was observed for the α-$Mg(BH_4)_2$

in the α → β transition and for amorphous $Mg(BH_4)_2$.[122] For the porous γ- $Mg(BH_4)_2$, significant desorption was observed at <150 ^oC.[128] In another study, Chong *et al.* reported 2.5 wt.% H_2 desorption for the sample decomposed at ~200 ^oC with very slow kinetics.[83]

The overall dehydrogenation of $Mg(BH_4)_2$ follows a complex pathway with the formation of intermediate amorphous phases alongside with the crystalline reaction products. The DSC data reported at least four endothermic events in the 250-450 ^oC region.[128] The *ex-situ* and *in-situ* PXD analysis indicate amorphous intermediates in the ~280-320 ^oC region with melting of $Mg(BH_4)_2$.[131] Valuable information on amorphous phases can be drawn from solid state NMR and vibrational spectroscopy studies. Both techniques, however, produce complex spectra with broad signals that leave room for different interpretations. Thus, solution NMR was employed to achieve high resolution signal.[83,87,120,131] Species such as $Mg(B_3H_8)_2$, $MgB_{12}H_{12}$ have been successfully elucidated from the combination of these techniques. It has been proposed that the dehydrogenation of $Mg(BH_4)_2$, follows the multi-step pathway seen Eqn. 1.12-1.14 with $MgB_{12}H_{12}$ as an important intermediate.[77-80]

$$6Mg(BH_4)_2 \longrightarrow 5MgH_2 + MgB_{12}H_{12} + 13H_2 \quad \textbf{(1.12)}$$

$$5MgH_2 + MgB_{12}H_{12} \longrightarrow 5Mg + MgB_{12}H_{12} + 5H_2 \quad \textbf{(1.13)}$$

$$5Mg + MgB_{12}H_{12} \longrightarrow 6MgB_2 + 6H_2 \quad \textbf{(1.14)}$$

Understanding the nature of amorphous intermediates is crucial in order to achieve reversibility of hydrogen desorption. In view of the high stability of the closed B_{12}-caged, the stable intermediate compound such as $MgB_{12}H_{12}$ has been the challenge with respect to reversibility. Attempts to completely regenerate from the fully decomposed $Mg(BH_4)_2$ at moderate conditions were unsuccessful, attributed to the high kinetic barrier to

hydrogenation of the $MgB_{12}H_{12}$.[81] Severa *et al.* demonstrated the direct hydrogenation of MgB_2 to $Mg(BH_4)_2$ under 900 bar H_2 at 400^oC. Less than 5% of $MgB_{12}H_{12}$ was detected as side product suggesting that the high-pressure reaction pathway circumvented the formation of stable boranes (*i.e.* $MgB_{12}H_{12}$).[82] Regardless of the extreme re-hydrogenation condition, MgB_2-$Mg(BH_4)_2$ cycling system demonstrated the potential for high capacity hydrogen storage applications. On the other hand, the amorphous phases formed below 300 ^oC have proven to be partially reversible, cycling of ~2 wt.% H_2 for three cycles.[133] The desorption reaction was carried out at 285 ^oC under 3 bar H_2, yielded an unidentified amorphous phase, and the absorption reaction was performed at 285 ^oC 120 bar H_2. Prior to this study, reversibility of intermediate species back to $Mg(BH_4)_2$ highlighted by the work of Chong *et al.* demonstrated (dehydrogenation 200 ^oC; re-hydrogenation 250 ^oC, 120 bar H_2) $Mg(BH_4)_2$-$Mg(B_3H_8)_2$ cycling system. Although the low cycling capacity, 2.5 wt.% H_2, and kinetic constraint (dehydrogenation 200^oC, 5 weeks, 50% yield) are impractical for on-board hydrogen storage applications, it establishes that the cycling of magnesium borohydride to magnesium boranes, can be accomplished at moderate temperatures and pressures.[83] Furthermore, detailed investigation of the hydrogenation of independently synthesized $Mg(B_3H_8)_2(THF)_2$ (THF = tetrahydrofuran), upon finding that it was not possible to remove the THF solvate, demonstrated the improvement in cycling conditions back to $Mg(BH_4)_2$ (50 bar H_2, 5 hours, 200^oC), relative to of the aforementioned solvent free $Mg(B_3H_8)_2$.[87]

1.4 Motivation for this Dissertation

The primary focus described in this body of work was to enhance the understanding of the interaction of the THF molecules and the $B_3H_8^-$ ions with Mg, a foundation to further explore the effect of solvent coordination on the dehydrogenation pathways and cycling capabilities of different boranes systems back to $Mg(BH_4)_2$. Chapter 2 of this dissertation presents the structure characterization of $Mg(B_3H_8)_2(THF)_2$ using infrared spectroscopy and computational studies. The NMR measurements indicate the presence of octahydrotriborate, $B_3H_8^-$ ion, and tetrahydrofuran, THF. The material melts under mild heating to remove partial THF results in an amorphous state upon cooling to room temperature, thus, prevents the use of diffraction for the determination of its structure. Various geometries for the $Mg(B_3H_8)_2(THF)_2$ were explored. Similar systems in which Mg^{2+} was coordinated to the $B_3H_8^-$ ion and some other organic molecules were used as a starting point.

The kinetic enhancement of THF on the reversibility of $Mg(B_3H_8)_2$ back to $Mg(BH_4)_2$ was revisited in chapter 3, led to the surprise observation of THF remain in the hydrogenated $Mg(BH_4)_2$. This piqued our interest to further explore the subsequent dehydrogenation, results in the selective formation of $MgB_{10}H_{10}$. Various THF-solvated $Mg(BH_4)_2$ with different THF:Mg ratio were prepared and moderate-temperature-dehydrogenation trials were carried out. In all trials, selective formation of $MgB_{10}H_{10}$ intermediate species was confirmed. Dehydrogenation kinetics at different temperature were also reported.

In chapter 4, the THF-ring opening process and the formation of magnesium tetrabutoxyborate, $Mg[B(OBu)_4]_2$ (Bu = C_4H_9) are discussed in detail. To further understand the effect of additives on the reversibility of dehydrogenated $MgB_{10}H_{10}$, a method for the synthesis of $Mg[B(OBu)_4]_2$ was developed. Subsequent hydrogenation trials of $MgB_{10}H_{10}$ in the presence of excess $Mg[B(OBu)_4]_2$ or MgH_2 were carried out by Pressure-Composition-Temperature, PCT. Characterization of the products was accomplished through NMR. Moreover, the kinetic analysis based on PCT cycling data is also reported. In chapter 5, the reversibility between $MgB_{10}H_{10}$ and $Mg(BH_4)_2$ was reported. A process that was successfully carried out by continuous heating and fluctuating hydrogen pressure between de-/re-hydrogenation half cycle, using Pressure-Composition-Temperature (PCT).

Chapter 6 presents the independent synthesis magnesium dodecaborane followed by structure determination using group theory calculation and X-Ray Diffraction (XRD), proposed a $MgB_{12}H_{12}(THF)_3$ molecular structure. Alternative synthesis approach, dehydrogenation of $Mg(B_3H_8)_2(THF)_3$, was also developed results in selective formation of THF-solvated *closo* boranes, 4:1 $MgB_{12}H_{12}$ to $MgB_{10}H_{10}$. Hydrogenation trials of these boranes was investigated using PCT and final products were characterized by NMR.

CHAPTER 2: MOLECULAR STRUCTURE OF AMORPHOUS THF-SOLVATED MAGNESIUM OCTAHYDROTRIBORATE

2.1 Introduction

Group I and II borohydrides possess some of the highest hydrogen contents of all the known compounds. Thus, they have been widely explored as potential hydrogen carrier materials for onboard applications of polymer electrolyte membrane fuel cells. $Mg(BH_4)_2$ has attracted recent interest due to its combinations of a high hydrogen capacity and favorable (~40 kJ/mole) enthalpy of dehydrogenation.[53] The reversible dehydrogenation of $Mg(BH_4)_2$ to MgB_2, with 11.2 wt.% hydrogen, stands as the highest hydrogen storage capacity for any materials that can be directly hydrogenated.[82] The forcing conditions (dehydrogenation >400^{o}C; rehydrogenation 400^{o}C, 900 bar H_2) render this system impractical for on-board vehicular hydrogen storage applications. Reversible dehydrogenation between $Mg(BH_4)_2$ and $Mg(B_3H_8)_2$, has been demonstrated to occur under milder conditions (dehydrogenation 200^{o}C, 5 weeks; rehydrogenation 200^{o}C, 50 bar H_2, 48 hours) however this system has only a maximum 2.5 wt.% hydrogen cycling capacity, (Eqn. 2.1):[83]

$$3Mg(BH_4)_2 \Leftrightarrow Mg(B_3H_8)_2 + 2MgH_2 + 2H_2 \quad \textbf{(2.1)}$$

Recently, a 1:2 molar mixture of independently synthesized $Mg(B_3H_8)_2(THF)_2$ and MgH_2 was found to undergo hydrogenation to $Mg(BH_4)_2$ in only 2 hours at 200^{o}C under 50 bar H_2.[87] It was noted that the solvated material undergoes a phase change to a super-

viscous melt at temperatures below 80˚C suggesting that the observed enhancement of the kinetics of hydrogenation are the result of the transition to the molten state. However, *a priori* it is also possible that the coordination of THF to Mg might also give rise to a kinetic enhancement of the hydrogenation of $B_3H_8^-$ particularly if THF and $B_3H_8^-$ are coordinated to the same Mg and thus resulting in electronic perturbation of the $B_3H_8^-$. In order to probe this possibility, we undertook a molecule structure determination of amorphous $Mg(B_3H_8)_2(THF)_2$ using a combination of infrared spectroscopy and density function theory (DFT) calculations.

Infrared (IR) spectra of molecules containing B-H bonds have been extensively studied and a systematic attribution of B-H stretching bands to different molecular structures has been reported.[88] Magnesium and $B_3H_8^-$ compounds containing ether solvates can have either an ionic or a non-ionic character.[89] In the former case, Mg is coordinated only to the ether molecules (*e.g.* in $Mg(THF)_6(B_3H_8)_2$[90] and $Mg(diglyme)_2(B_3H_8)_2$[91]) with the observation of the stretching bands due to bridging B-H-B (~2100 cm^{-1}) and to terminal B-H (>2400 cm^{-1}) in the IR spectrum. On the other hand, $Mg(B_3H_8)_2$, $Mg(B_3H_8)_2(Et_2O)_2$, and $Mg(B_3H_8)_2(Me_2O)_2$ (Et = C_2H_5, Me = CH_3) are molecular species with a direct bond of Mg to the $B_3H_8^-$ ions, display an additional stretching band at ~2300 cm^{-1} due to the bridging Mg-H-B movements.[89] Moreover, $B_3H_8^-$ ions can be coordinated to an atom, M, by means of one or more B-M chemical bonds, with additional H-M bonds. For example, in $Mg(B_3H_8)_2(Et_2O)_2$, and $Mg(B_3H_8)_2(Me_2O)_2$, there are two B-Mg and two H-Mg bonds for each $B_3H_8^-$ ion.[89] However, in $Ag(CNB_3H_7)_2$, there is one B-N and two H-N bonds.[92] In the crystal structure of NaB_3H_8, each Na is surrounded by four $B_3H_8^-$ anions: for two of them, Na is closer to two B atoms, while for the other $B_3H_8^-$ ions, Na is closer to a single

B.[92,93] Finally, the low temperature solid phase of $(CO)_3MnB_3H_8$ contains three Mn-H-B bridging hydrides, one bridge bond for each boron atom.[94] Studies of the structures of the isolated $B_3H_8^-$ ion and the $ClCuB_3H_8$ complex have been reported using ab-initio calculations at the MP2 level of theory and density function theory (DFT) methods at the B3LYP level.[95,96] It is indicated that the most stable complex displayed the coordination of two boron atoms to the Cu atom *via* two B-H-Cu hydrogen bonds. Guided by these previous studies, we have utilized a combination of infrared spectroscopy measurements, ab-initio, and DFT calculations to determine the most stable structure of the $Mg(B_3H_8)_2(THF)_2$ molecule. We have found that Mg is directly linked to each $B_3H_8^-$ ion by two B-Mg and two bridging B-H-Mg bonds.

2.2 Experimental

2.2.1 Preparation of $Mg(B_3H_8)_2(THF)_2$

$Mg(B_3H_8)_2(THF)_2$ was prepared by the established synthesis procedure reported in the literature with slight modification in the final drying step.[87] Under N_2 flow, magnesium turnings (0.5g) were added to 20 mL of purified mercury in a 250 mL Schlenk flask followed by heating to 180^{o}C for 4 hours with vigorous stirring. The flask was then allowed to cool to room temperature. BH_3•THF (100 mL) was added to the Mg/Hg amalgam with a syringe and the solution was stirred for 5 days. Upon the appearance of white precipitate, the magnesium octahydrotriborate was isolated using medium Schlenk frit filter followed by washing with THF to remove residual $Mg(BH_4)_2$. The white powder was dried for 4 hours at 50^{o}C under vacuum.

2.2.2. Infrared Vibrational Spectroscopy

Preliminary IR spectra were obtained in house at the University of Hawai'i at Manoa while the ATR spectra were obtained by the group of Analisa Paolone, CNR-ISC, U.O.S. La Sapienza. Recent studies borohydrides have avoided the KBr technique because BH_4^- can exchange with Br^- which has a similar ionic radii.[97] In the present case, the radius of $B_3H_8^-$ is much larger and should not give this problem. To exclude spurious effects, however, we performed infrared spectroscopy measurements in two different configurations: in transmission geometry using a pure pellet (without KBr or other salts) or by means of an Attenuated Total Reflectance accessory (ATR) on the hydride powders. The first method gives saturated bands in the B-H stretching region but provides well-defined spectra below 1700 cm^{-1}, where the intensity of bands is much lower. On the other hand, the second method is well-suited in the B-H stretching region. It must be noted, however, that ATR displays the same features obtained in the case of the pure pellet below 1700 cm^{-1}, but with a lower quality of the measurement. Therefore, in the following, we report data obtained by ATR between 1800 and 3300 cm^{-1} and by transmission measurements on the pure pellet in the frequency range 600-1700 cm^{-1}. In this framework, infrared spectroscopy measurements below 1800 cm^{-1} were performed at room temperature by means of an Agilent Cary 660 spectrometer equipped with a ceramic source, a MCT detector, and a KBr beam splitter. A small amount of the sample was pressed in a dye to obtain a self-standing pellet. The pellet was placed in a vacuum tight cell during measurements due to the pyrophoric nature of $Mg(B_3H_8)_2(THF)_2$. Above 1800 cm^{-1}, data were collected by means of a Bruker Alpha spectrometer equipped with an ATR accessory.

Sample handling was performed in a Ar glovebox to avoid contamination.[98,99] All absorption spectra were collected with a spectral resolution of 2 cm^{-1}.

2.2.3 Density Functional Theory Calculation

The DFT calculations were carried out by the group of Analisa Paolone, CNR-ISC, U.O.S. La Sapienza. Preliminary geometries of the isolated $B_3H_8^-$, THF and $Mg(B_3H_8)_2(THF)_2$ were obtained by means of the Avogadro software using the universal force field energy minimization routine.[100] Ab-initio and DFT calculations were performed starting from those geometries by means of the Firefly package.[101] In all cases, the 6-31G** basis set was used. The wxMacMolPlt software was used to visualize the molecular geometries and vibrations.[102] After calculation of the infrared active vibrations, the IR spectrum was simulated by summing Lorentzian curves centered at each calculated IR vibration frequency with a fixed 10 cm^{-1} peak width.

2.3 Results and Discussion

2.3.1 The isolated $B_3H_8^-$ ion

Preliminary ab-initio and DFT calculations were performed on isolated $B_3H_8^-$ and THF to verify that the geometries agree with those found experimentally: *i.e.* in THF the four C atoms reside in the same plane, while the O atom is located outside; for $B_3H_8^-$ two H atoms reside in the plane of the three B atoms (Figure 2.1-2.2):

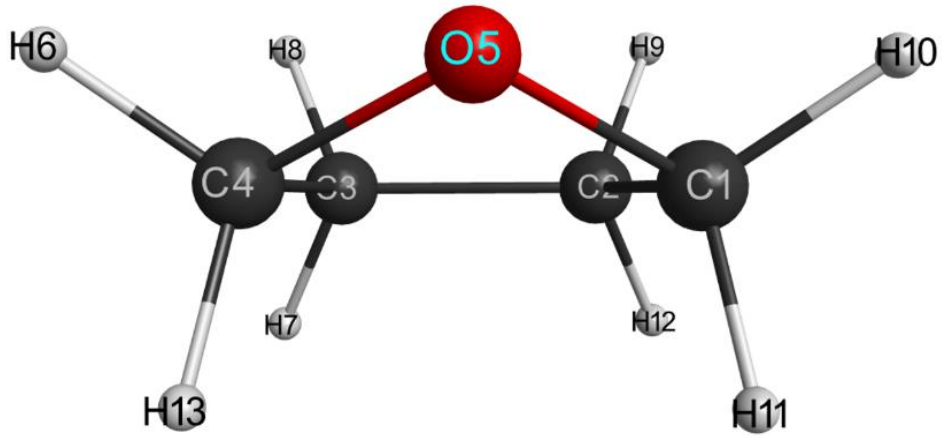

Figure 2.1: Optimized geometries of isolated THF

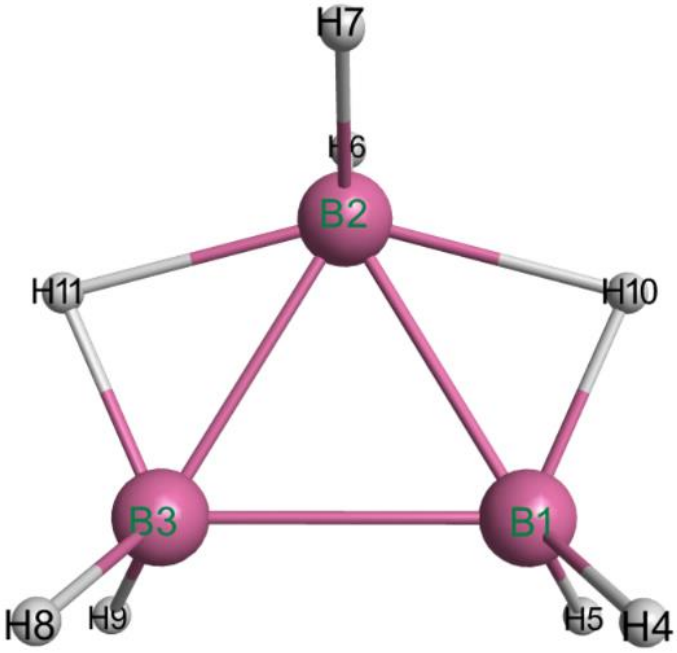

Figure 2.2: Optimized geometries of isolated $B_3H_8^-$

Table 2.1: *Bond lengths of the isolated $B_3H_8^-$ ion*

	This work			Literature			
	MP2	B3LYP	B97D	MP2[103]	B3LYP[103]	Experimental[104]	Experimental[105]
B1-H4	1.20	1.21	1.22	1.20	1.21	1.07	1.05-1.20
B1-H10	1.26	1.26	1.28	1.26	1.26	1.15	1.20
B2-H10	1.47	1.50	1.51	1.47	1.49	1.43	1.50
B2-H6	1.20	1.21	1.22	1.21	1.21		1.05-1.20
B1-B2	1.78	1.79	1.80	1.78	1.79	1.78	1.77
B1-B3	1.82	1.85	1.86	1.82	1.85	1.82	1.80

In the present work, we optimized geometries with the following theories: MP2, B3LYP and B97-D.[134] Table 2.1 reports the main bond lengths found in this study. One can note a good agreement with those reported in a previous DFT study[103,106] and those found experimentally.[104,105] The infrared active vibrations of isolated $B_3H_8^-$ were calculated with the various theories and the simulated absorbance curves are reported in Figure 2.3.

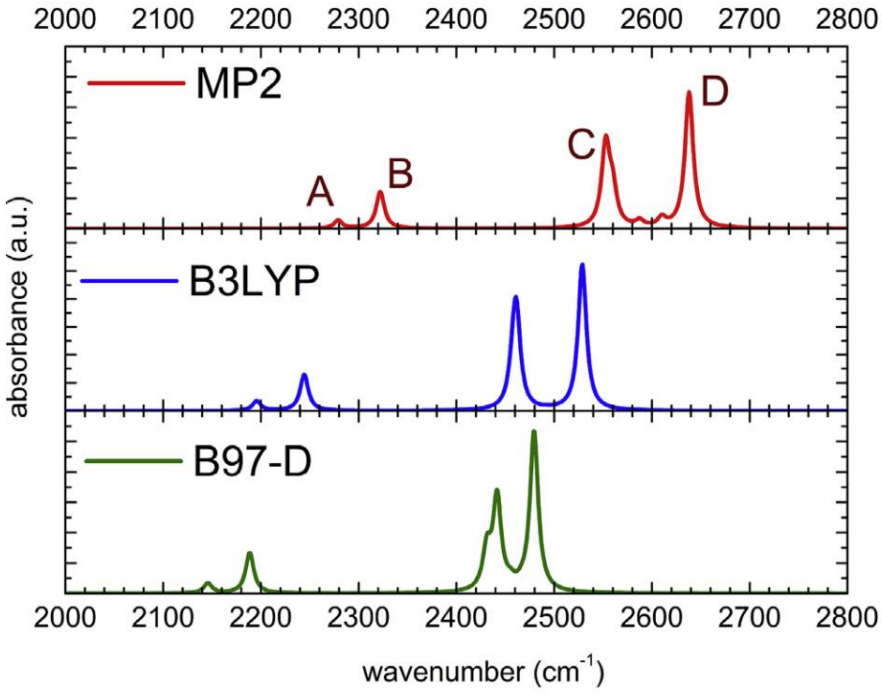

Figure 2.3: Calculated infrared absorption of isolated $B_3H_8^-$ at the MP2, B3LYP and B97D level of theories

In all the three used theories, in the region of the B-H stretching, one finds two less intense bands below 2400 cm^{-1} (band A and B) which are due to bridging B-H-B movements and two structured bands (C and D) in the frequency region between 2450 and 2700 cm^{-1}, which can be attributed to terminal B-H stretches. The spectra calculated by the different theories look similar but are rigidly shifted toward lower frequency in the following order: MP2, B3LYP and B97-D. All theories are able to give the main features of the infrared spectrum of isolated $B_3H_8^-$ ion. It should be noted that in most samples, the experimental bands A and B are centered between 2050 and 2150 cm^{-1}, while bands C and D are found between 2400 and 2600 cm^{-1}.[89] In Figure 2.3, it seems that the frequencies calculated by the theory B97-D are in closer agreement with the experimental values. One must keep in mind, however, that experimental infrared spectra of molecules in which the octahydrotriborate ion is linked to an atom display additional bands in the frequency range between lines A-B and C-D.[89]

The IR active vibrations of isolated THF are above this spectral range. Experimentally, THF displays intense IR bands at 2975, 2960, 2891, 1460, 1450 cm^{-1} and below.[107] Computationally, those bands are shifted 100 cm^{-1} toward higher energies.

2.3.2 The $Mg(B_3H_8)_2(THF)_2$

Figure 2.4 displays the experimental absorption spectrum of $Mg(B_3H_8)_2(THF)_2$ in the B-H stretching region. No OH stretch (>3000 cm^{-1}), indicates contamination from water, is observed; the absorption bands at 2800 and 3100 cm^{-1} are due to the vibrations of the THF molecules in $Mg(B_3H_8)_2(THF)_2$. Moreover, ^{11}B NMR displays only one nonet

signal of $B_3H_8^-$ (Figure 2.5). Both observations suggest the occurrence of a pure sample, without significant contamination.

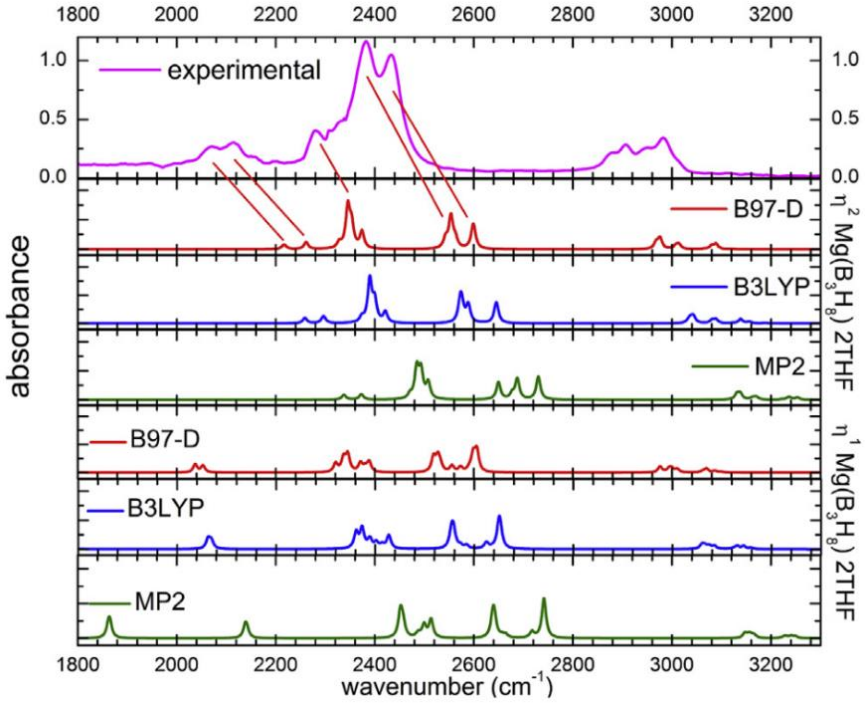

Figure 2.4: Measured infrared absorption with calculations for η1-$Mg(B_3H_8)_2(THF)_2$ and η2-$Mg(B_3H_8)_2(THF)_2$ at the MP2, B3LYP and B97-D level of theories

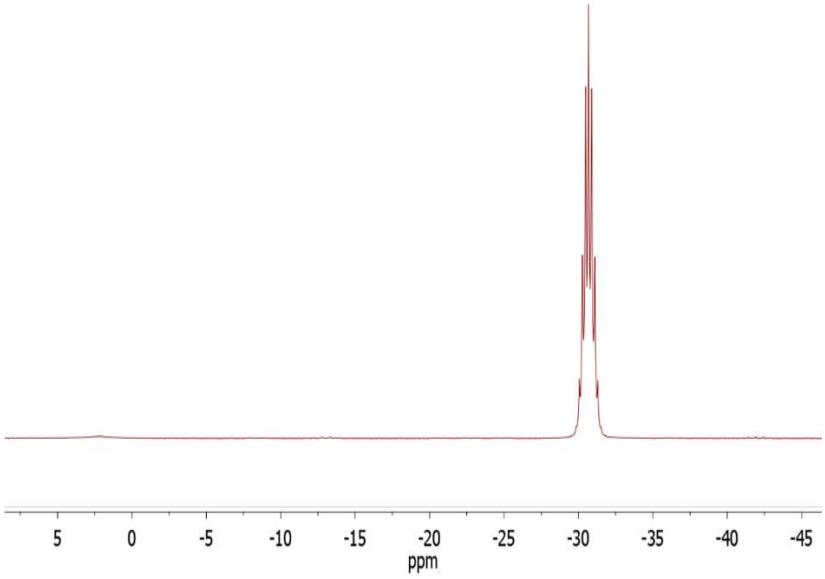

Figure 2.5: ^{11}B NMR in D_2O of the synthesized $Mg(B_3H_8)_2(THF)_2$

In Figure 2.4, one can note the presence of two weaker bands around 2069 and 2115 cm^{-1} and two strong bands around 2385 and 2432 cm^{-1}. Moreover, a large and structured band around 2300 cm^{-1} is clearly visible. This band was attributed to the stretching vibrations of the B-H-Mg in similar compounds.[89] Therefore, our compound has a molecular structure with Mg directly linked to the octahydrotriborate ion. Recently, it has been shown that the newly synthesized $LiB_3H_8(THF)$ complex shows infrared absorption bands due to Li-H-B bridging bonds.[108]

Computational work, however, could be used to identify the most stable structure of $Mg(B_3H_8)_2(THF)_2$, *i.e.* whether Mg is linked to one, two or three B atoms and how many H bridging bonds are present. We explored these various geometries for the $Mg(B_3H_8)_2(THF)_2$ complex. Similar systems in which a metal atom was linked to the $B_3H_8^-$ ion and some other organic molecules, such as Et_2O, Me_2O, cyclopentadienyl (Cp), or THF were used as starting points.[89,92] In the compounds containing THF, tetrahydrofuran coordinated to the metal atom through the O atom.[89] Therefore, we started the optimizing procedure from a geometry with the two THF molecules pointing towards Mg through the O atom. $B_3H_8^-$ groups can be attached to Mg by means of one, two or three B-Mg chemical bonds ($\eta1$, $\eta2$ and $\eta3$ structures).[89,92] We could not obtain any stable structure in which there are three boron atoms for each $B_3H_8^-$ group linked to Mg atom. Indeed, during the attempted optimization procedure, the octahydrotriborate broke up. Table S1 reports the energies of the optimized geometries of $\eta1$- and $\eta2$-$Mg(B_3H_8)_2(THF)_2$ at the MP2, B97-D, and B3LYP level of theory, while Figure 2.6 displays the optimized geometries at the MP2 level.

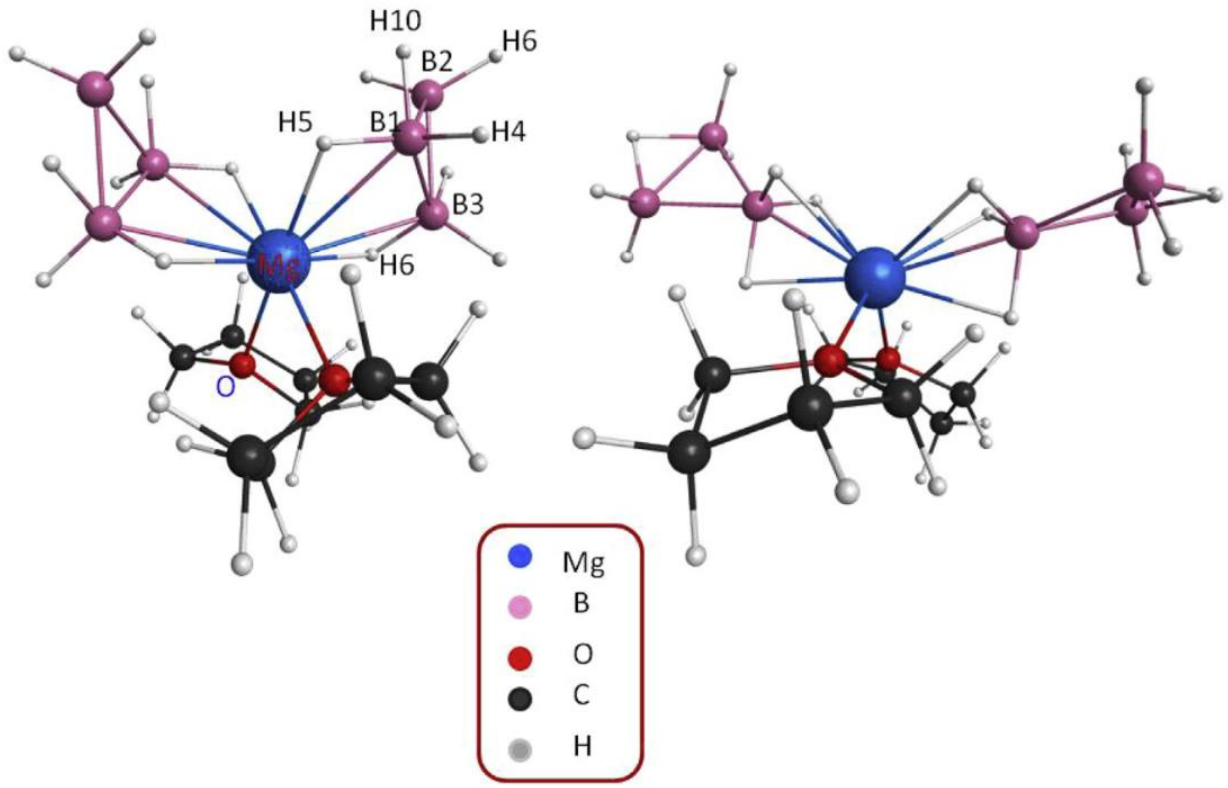

Figure 2.6: Optimized geometries for η1-$Mg(B_3H_8)_2(THF)_2$ (on the right) and η2-$Mg(B_3H_8)_2(THF)_2$ (on the left) at the MP2 level

Regardless of level of theory being used for calculations, the η2 structure always has a lower energy than the η1 and, therefore, the former is the most thermodynamically stable (Table S1, Appendix). The length of the main bonds found for $Mg(B_3H_8)_2(THF)_2$ at different levels of theory (Table S2, Appendix). The B-H bond lengths are generally overestimated but there is a general good agreement between calculated and experimental B-B, Mg-B, Mg-H, and Mg-O bond lengths measured in similar systems.

To confirm that the compound has an η2 structure, we calculated the infrared absorption spectrum of both η1- $Mg(B_3H_8)_2(THF)_2$ and η2-$Mg(B_3H_8)_2(THF)_2$ at the three theory levels (MP2, B3LYP and B97-D). The calculated absorptions are seen in Figure 2.4. The spectra obtained by means of different theories for each structure are very similar,

except that they are shifted toward higher frequencies as one proceeds from B97-D, to B3LYP, and finally to MP2. For the η1 structure, the frequencies of the bridged B-H-B vibrations are usually underestimated; moreover, for B3LYP and MP2, the B-H-B stretching frequencies are so close that they could not be resolved and would appear as a single band in an infrared spectrum. Generally, for each level of computation, the calculated absorbance of the η2 structure is much less structured than that of the η1 structure and more closely resembles the experimental absorption spectrum. These features and the results of the minimization of energy suggest that the most plausible structure of $Mg(B_3H_8)_2(THF)_2$ is the η2.

Figure 2.4 displays the infrared active stretching vibrations frequencies found at the MP2, B3LYP, and B97-D level for η2-$Mg(B_3H_8)_2(THF)_2$. The vibrational frequencies calculated at the B97-D level of theory are the closer to the experimental ones. Despite the succession of infrared lines is correctly described by calculations, however, all experimental frequencies are lower than those calculated by all models. Possibly this fact can be due to the anharmonicity of the B-H bonds, similarly to the case of alkali borohydrides containing BH_4^- ions.[109]

Table 2.2: *Calculated infrared vibration frequencies and intensities of η2-$Mg(B_3H_8)_2(THF)_2$ at different level of theory in the region of the B-H stretching vibrations and comparison with the frequencies of the experimental bands.*

Attribution	MP2		B3LYP		B97D		Experimental
	ω (cm^{-1})	I (km/mol)	ω (cm^{-1})	I (km/mol)	ω (cm^{-1})	I (km/mol)	ω (cm^{-1})
Bridged B-H-B stretching	2336	31.4	2259	21.1	2214	23.3	2069
	2337	23.7	2259	40.2	2217	28.9	2115
	2372	37.7	2295	43.8	2260	39.3	
	2372	25.5	2298	42.7	2260	35.3	
Bridged Mg-H-B stretching	2470	48.2	2374	59.2	2327	64.2	2280
	2484	343.4	2390	505.2	2344	460.5	2325
	2492	307.5	2400	249.5	2352	251	
	2507	181	2421	123.8	2373	187.9	
Terminal B-H stretching	2648	125.1	2572	145.6	2542	58.8	2383
	2649	71.7	2574	142.9	2542	45.9	2432
	2676	28.9	2576	41	2552	237.2	
	2677	30.5	2577	62.8	2553	125.4	
	2686	215	2588	179.4	2561	44.4	
	2689	23.1	2591	28	2562	53.7	
	2729	240.8	2645	161.9	2597	180.4	
	2730	22	2647	91.2	2599	112.8	

Figure 2.7 displays the typical movements occurring in the three types of stretching vibrations: bridged B-H-B, bridged Mg-H-B, and terminal B-H. The investigation of the IR spectrum of the $Mg(B_3H_8)_2(THF)_2$ compound was extended to lower frequencies.

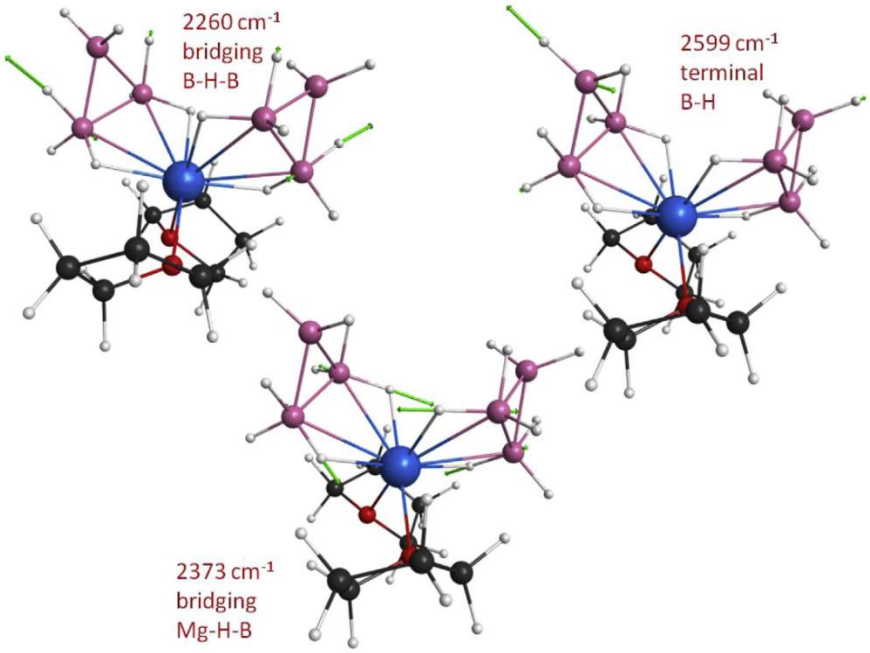

Figure 2.7: Atomic displacements corresponding to selected vibrations calculated at the B97-D level, representing B-H-B bridging, Mg-H-B bridging and terminal B-H stretching movements.

Figure 2.8 reports the experimental IR spectrum between 600 and 1700 cm^{-1}. Well-defined peaks are visible around 678, 707, 846, 868, 922, 966, 1010, 1040, 1138, 1180, 1250, 1297, 1315, 1348, 1456 cm^{-1}, while a broad band extends up to ~1600 cm^{-1}. No band centered around 1630 cm^{-1} is observed, due to possible water contamination. There is a general good agreement of the calculated and experimental bands below 1200 cm^{-1}. Above this frequency, the experimental spectrum becomes less well-defined and a comparison with calculations is more difficult, possibly because of the amorphous nature of the compound, which broadens the absorption bands. This behavior is different from that of other hydrides, like for example NH_3BH_3, which due to their crystalline structure display very well-defined absorption bands in the whole infrared range.[110]

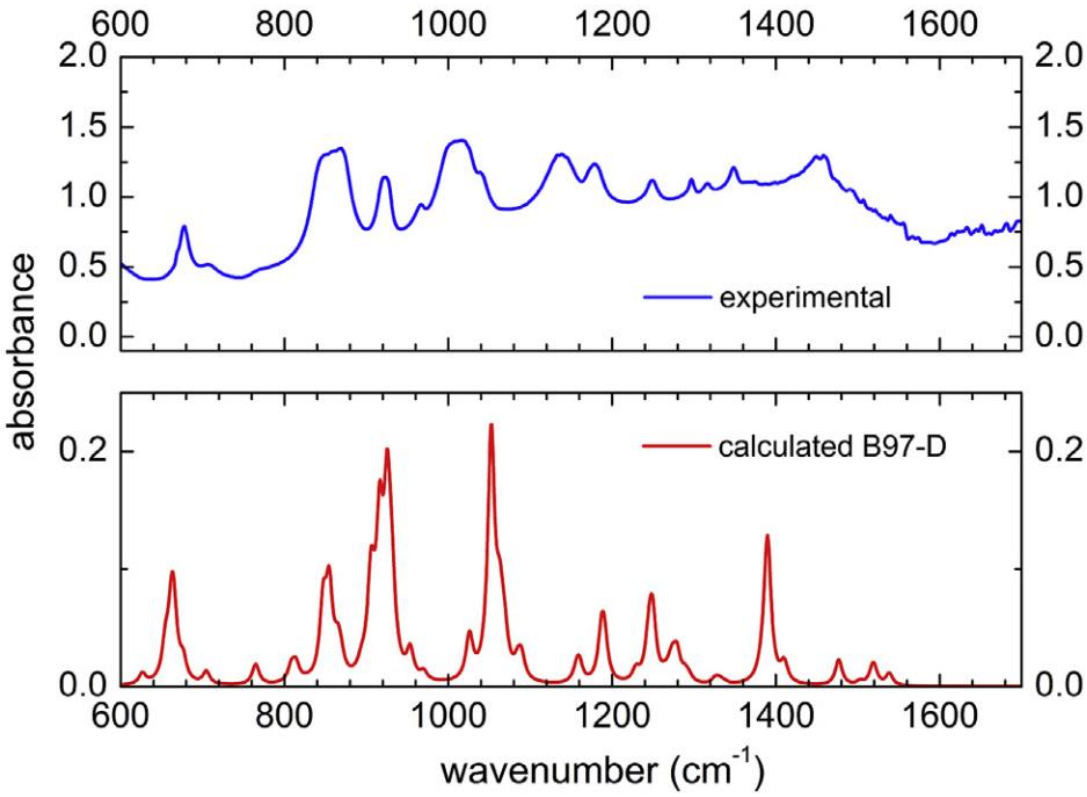

Figure 2.8: Comparison of the experimental and calculated absorption spectrum of $Mg(B_3H_8)_2(THF)_2$, in the frequency range between 600 and 1700 cm^{-1}.

Once the structure of the new $Mg(B_3H_8)_2(THF)_2$ compound is proposed, we proceeded to calculate the formation energy of $Mg(B_3H_8)_2M_2$ as following:

$$E_{form} = E(Mg(B_3H_8)_2S_2) - E(Mg(B_3H_8)_2) - 2E(S)$$

where S = THF, Me_2O, or Et_2O. Magnesium octahydrotriborate has been recently reported to be an amorphous solid.[111] However, a detailed structural investigation is not available. We minimized the energy of a hypothetical $Mg(B_3H_8)_2$ molecule, starting from the $Mg(B_3H_8)_2(THF)_2$ compound and removing THF. For this purpose, we adopted ab-initio calculations at the MP2 level of theory (Table S3, Appendix). The stable structure of magnesium octahydrotriborate shows that each B_3H_8 ion is linked to Mg by three B-Mg

and three B-H-Mg bonds (Figure 2.9). Conversely, both $Mg(B_3H_8)_2(Et_2O)_2$ and $Mg(B_3H_8)_2(Me_2O)_2$ show an η2 structure, similar to that here proposed for $Mg(B_3H_8)_2(THF)_2$, in agreement with the structures proposed by Kim *et al.*[89] on the basis of diffraction studies.

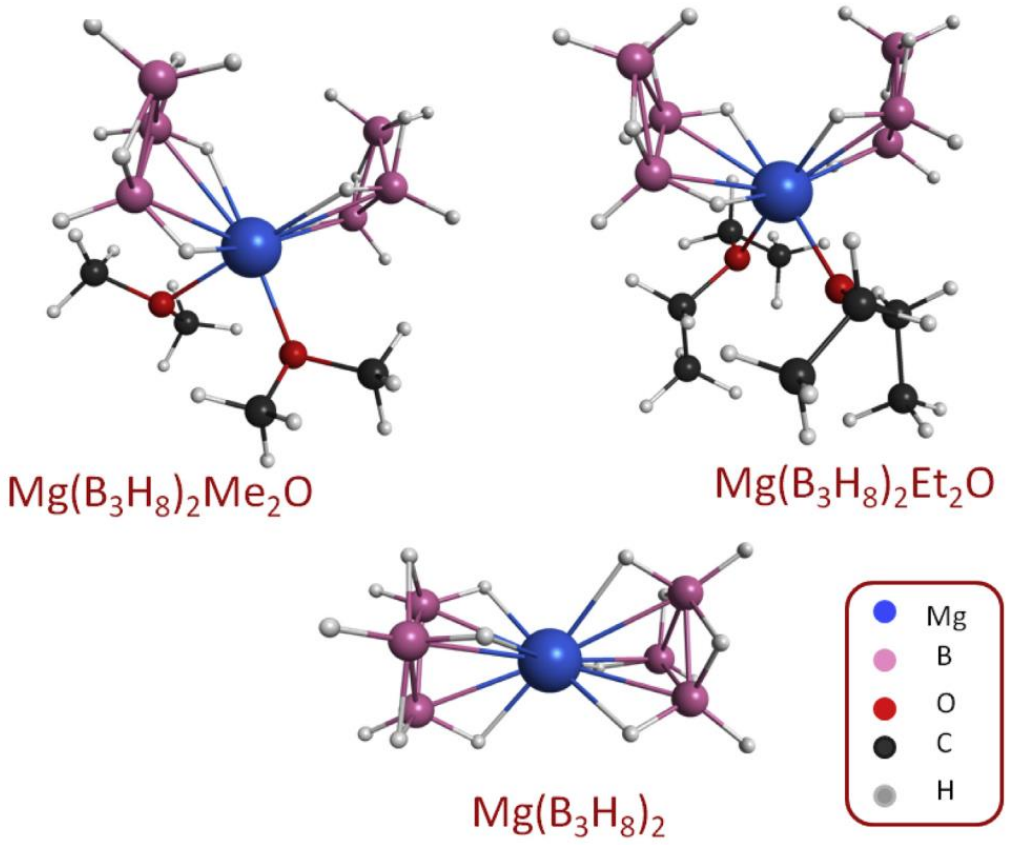

Figure 2.9: Optimized geometries of $Mg(B_3H_8)_2$, $Mg(B_3H_8)_2(Me_2O)_2$ and $Mg(B_3H_8)_2(Et_2O)_2$ at the MP2 level.

The obtained formation energies of the two ether complexes are quite similar (199 and 203 kJ/mol for Me_2O and Et_2O, respectively), while 227 kJ/mol is calculated for $Mg(B_3H_8)_2(THF)_2$. THF is, therefore, the molecule more strongly bound to magnesium octahydrotriborate.

2.4 Conclusions

The combination of IR spectroscopy, ab-initio (MP2), and DFT (B3LYP, B97-D) calculations have proven to be applicable methods for the determination of the molecular structure of amorphous $Mg(B_3H_8)_2(THF)_2$. We have found that Mg is directly linked to each octahydrotriborate ion by means of two B-Mg and two bridging B-H-Mg bonds. B97-D functional seems to be the best choice to reproduce the experimental spectrum in the mid infrared range between 600 and 3300 cm^{-1}, even though anharmonicity of the B-H stretching vibrations should be present. Moreover, calculations provide evidence of the stabilization of the THF solvate of $Mg(B_3H_8)_2$ and indicate that the THF complex has greater stabilization energy than other dialkyl ethers complexes by ~25 kJ/mol.

CHAPTER 3: DEHYDROGENATION STUDIES OF THF-SOLVATED MAGNESIUM BOROHYDRIDE

3.1. Introduction

Development of advanced hydrogen storage materials for onboard hydrogen storage systems is a key technology for the realization of a hydrogen economy. A viable onboard hydrogen carrier must possess all of the following capabilities: high gravimetric and volumetric hydrogen densities, adequate operating pressure and temperature, good cycling stability/kinetics, and low cost.[10] Only a few of the thousands of materials investigated have garnered as much interest as $Mg(BH_4)_2$, possesses appropriate thermodynamics and hydrogen capacity to meet these criteria.[73]

Magnesium borohydride is a promising material with a 14.8 wt.% hydrogen capacity. Investigation on the dehydrogenation properties of $Mg(BH_4)_2$ found that temperatures up to 600 ^oC were required to release all the hydrogen, proposed to proceed through multi steps together with the formation of intermediate compounds.[81,112,113] Early X-ray Diffraction measurements of $Mg(BH_4)_2$ after heat treatment at 320 ^oC and 350 ^oC pointed towards the formation of MgH_2 and Mg in two distinct steps as following (Eqn. 3.1-3.2):[112]

$$Mg(BH_4)_2 \longrightarrow MgH_2 + 2B + 3H_2 \quad \textbf{(3.1)}$$

$$MgH_2 \longrightarrow Mg + H_2 \quad \textbf{(3.2)}$$

Follow up studies on the dehydrogenation of $Mg(BH_4)_2$ using Thermogravimetric Analysis (TGA) and Pressure-Composition-Temperature (PCT) revealed that the initial decomposition to MgH_2 actually consisted of multi-step reactions, suggesting a more

complicated mechanism than previously proposed.[79] To further investigating into the detail mechanism of the $Mg(BH_4)_2$ dehydrogenation process, Nuclear Magnetic Resonance (NMR) spectroscopy was employed to take into account the absence of discernible X-ray or neutron diffraction peaks from the reacted samples, phases that were presumed to be amorphous or nanocrystalline.[115] Recent reports suggest that polyboranes, *i.e. arachno*-$B_3H_8^-$, *closo*-$B_{10}H_{10}^{2-}$ and *closo*-$B_{12}H_{12}^{2-}$ are significant intermediate products of the dehydrogenation.[83,127]

The formation of intermediate boranes is known to occur during the decomposition of BH_4^- in solution.[126] In this process, either BH_4^- or a polyborane reacts with diborane upon dissolution, condensing into larger boranes, until $B_{12}H_{12}^{2-}$, is formed. On the other hand, *in situ* infrared analysis[116] and DFT calculations[116] indicate that only trace levels of diborane are released during the solid-state dehydrogenation of $Mg(BH_4)_2$, implying that it immediately reacts upon formation or the decomposition mechanism in the solid phase is different than of solution phase.

NMR studies concluded that $MgB_{12}H_{12}$, forming at temperatures above 250 ^oC, is a thermodynamic endpoint, preventing re-hydrogenation to $Mg(BH_4)_2$.[115] Thus, it is logical to investigate the decomposition of $Mg(BH_4)_2$ under moderate conditions (*i.e.* $\leq 250^oC$) or discover de-/re-hydrogenation pathway that circumvents the formation of $MgB_{12}H_{12}$. The former case highlights the work of Chong *et al.* on the reversible dehydrogenation of $Mg(BH_4)_2$ to $Mg(B_3H_8)_2$ where $Mg(B_3H_8)_2$ is formed selectively at 250^oC and can be cycled back to $Mg(BH_4)_2$ at 200^oC under 120 bar H_2.[83] One should note that, however, the low cycling capacity, 2.5 wt.% and slow kinetics (dehydrogenation, 200^oC, 5 weeks, 50% yield) render this system impractical. In the latter case, Severa *et al.* demonstrated the

direct hydrogenation of MgB_2 to $Mg(BH_4)_2$ under 900 bar H_2 at 400 °C.[82] Less than 5% of $MgB_{12}H_{12}$ was detected as side product suggesting that the high-pressure reaction pathway circumvented the formation of stable boranes (*i.e.* $MgB_{12}H_{12}$). Although it is not clear whether the minor amount of $MgB_{12}H_{12}$ is a side product resulting from the competition of other reaction pathways, these results confirm the plausibility of finding pathways for the full reversibility of $Mg(BH_4)_2$ that avoid the thermodynamic and kinetic pitfalls of polyborane intermediates (*e.g.* $MgB_{12}H_{12}$).

A follow-up study on $Mg(BH_4)_2$-$Mg(B_3H_8)_2$ cycling system demonstrated the hydrogenation of independently synthesized $Mg(B_3H_8)_2(THF)_2$ to $Mg(BH_4)_2$ could be achieved at 200°C for 2 hours under 50 bar H_2.[87] DSC reaction profile indicated that the THF coordinated $Mg(B_3H_8)_2$ underwent a phase change, from a free-flowing powder to a gel upon hydrogenation, a plausible explanation for the kinetic enhancement of solvated over solvent-free $Mg(B_3H_8)_2$. These findings prompt us to further explore the beneficial effect of solvent coordination on hydrogen release or uptake. Herein, this chapter explores THF modified hydrogenation of $Mg(B_3H_8)_2$ to $Mg(BH_4)_2$ as well as the discovery that the subsequent dehydrogenation of the obtained from this reaction $Mg(BH_4)_2$, results in the selective formation of $MgB_{10}H_{10}$ rather than $Mg(B_3H_8)_2$.

3.2 Experimental

All sample preparations and handling were conducted in a nitrogen glovebox or on a Schlenk line. Solvents were purified by a SPS system.

3.2.1 Preparation of crystalline $Mg(B_3H_8)_2(THF)_3$

Similar synthesis procedure to the aforementioned $Mg(B_3H_8)_2(THF)_2$ in chapter 2 was carried out with minor modification. The white precipitate was dried overnight under vacuum without the applied heat.

3.2.2. Preparation of $Mg(BH_4)_2(THF)_x$ (x = 0.25, 0.3, 0.5, 1, 3)

In general, the methodology for preparation followed the same basic prescription for all the synthesis differing only in the amounts of THF solvent added (Table 3.1). $Mg(BH_4)_2(THF)_x$ (x=0.25-3) were prepared by adding calculated volumes of THF, 11-84 μL (0.14-1.68 mmol), using a micropipette, directly onto 30 mg (0.56 mmol) of $Mg(BH_4)_2$. Products were then grinded with mortar and pestle. The synthesized products were later characterized by ^1H and ^{11}B NMR analysis.

Table 3.1: *Preparation of $Mg(BH_4)_2(THF)_x$ (x =0.25, 0.5, 1, 3)*

THF/Mg Ratio	**$Mg(BH_4)_2$ mg (mmol)**	**THF μL (mmol)**	**wt.% H_2**
0.25 : 1	30 (0.56)	11 (0.14)	6.1
0.3 : 1	30 (0.56)	14 (0.17)	5.8
0.5 : 1	30 (0.56)	23 (0.28)	4.9
1 : 1	30 (0.56)	45 (0.56)	3.5
3 : 1	30 (0.56)	135 (1.68)	1.6

3.2.3 NMR Characterization

Solution ^1H and ^{11}B NMR spectra were collected at room temperature using a Varian Unity Innova 500 MHz spectrometer, with resonance frequencies of 500.13 and 160.46 MHz, respectively. ^1H chemical shifts referenced to TMS (δ =0 ppm) and ^{11}B to $BF_3{\cdot}OEt_2$ (δ =0 ppm), both at 293 K. ^{11}B NMR spectra were recorded both with and without

^{1}H coupling. Deuterium oxide (D_2O) and 2:1 mixture of D_2O:THF were chosen as NMR solvents. A relaxation delay of 10 seconds was used for all ^{11}B analysis with 16^{o} pulse width.

Due to quadrupolar effects on the accuracies of integration values of different boron species, standards for integration in ^{11}B and ^{1}H NMR were prepared according to the following procedures. 0.05g $(CH_3)_4NBH_4$ and 0.18g $[(C_2H_5)_3NH]_2B_{10}H_{10}$ (1:1 molar ratio) were dissolved in 15 mL D_2O. 1 mL of solution was drawn for ^{11}B NMR analysis. Summary of results was reported in Table 3.2. ^{11}B NMR analysis indicated that $B_{10}H_{10}^{2-}$ distribution was underestimated (~8%) relative to BH_4^-. ^{1}H NMR analysis was carried for separately prepared $(CH_3)_4NBH_4$ and $[(C_2H_5)_3NH]_2B_{10}H_{10}$ followed the same procedure shown above. In the case of $[(C_2H_5)_3NH]_2B_{10}H_{10}$, no significant difference between experimental and calculated integration values was observed. However, in the case of $(CH_3)4NBH4$, experimental integration values of CH_3 relative to BH_4^- was observed to be ~21% higher relative to calculated integration values. Thus, it is crucial to take this difference into account when integrating any signal(s) against BH_4^- in ^{1}H NMR, *i.e.* determining amount of THF coordinate to $Mg(BH_4)_2$ in starting materials. Summary of results are reported in Table 3.2.

Table 3.2: *Standards for integration in solution ^{11}B and ^{1}H NMR*

NMR solvent			Calculated		Experimental			
D_2O	**Sample**	**Signal**	**# Proton**	**# Boron**	**# Proton**	**# Boron (1st trial)**	**# Boron (2nd trial)**	**# Boron (3rd trial)**
	$(CH_3)_4NBH_4$	$4CH_3$	12		14.56			
		BH_4	4		4			
	$[(C_2H_5)_3NH]_2B_{10}H_{10}$	$6CH_3$	18		17.78			
		$6CH_2$	12		12			
		eq. $B_{10}H_{10}$	8	8	8	8		
		ap. $B_{10}H_{10}$	2	2	1.93	1.98		
	$(CH_3)_4NBH_4$ +	BH_4	4	1		1	1	1
	$[(C_2H_5)_3NH]_2B_{10}H_{10}$	eq. $B_{10}H_{10}$	8	8		7.13	7.48	7.57
		ap. $B_{10}H_{10}$	2	2		1.77	1.88	1.87
					eq. + ap. B	8.9	9.36	9.44
					Average		9.23	

3.2.4 Pressure-Composition-Temperature isothermal de-/re-hydrogenation

Experiments were carried out in a stainless-steel reactor, either under static vacuum or 4 bar H_2 back pressure for dehydrogenation studies on a Suzuki Shokan PCT-2SDWIN Sievert type apparatus. The reactor was placed in a Glas-Col 125W heating mantle sleeve with a high temperature fabric. The temperature ramp rate was 5^{o}C/min from room temperature to desired temperature using a Glas-Col temperature controller. The weight percent of H_2 was calculated based on the pressure change. In a similar manner for hydrogenation studies, the PCT sample vessel was pressurized for 5 bar H_2 and held isotherm at 200 ^{o}C to desired time.

3.2.5 General mechanochemical/ball milling procedure

Unless stated otherwise, preparation mixtures of $Mg(BH_4)_2$-THF were added to 80 mL stainless steel vessels and milled under a nitrogen atmosphere in a Fritsch Pulverisette 7 planetary mill, at 300 RPM, 5 minutes per cycle for 6 cycles with 1-minute break then reversed direction, using 10 mm ball with sample mass ratio of approximately 20:1.

3.2.6 In-situ synchrotron Powder X-Ray Diffraction of THF-solvated $Mg(BH_4)_2$

Synchrotron radiation powder X-ray diffraction (SR-PXD) data were collected at the Swiss-Norwegian Beam Lines (SNBL, BM01) at ESRF, Grenoble, France. The sample was filled in a sapphire tube (inner diameter 1.2 mm and 0.2 mm wall thickness) under Ar atmosphere and connected via Vespel ferrules to a in-house manufactured Swagelok high-pressure sample cell and remote controlled gas rig. The sample was heated with a hot air blower, and the sample temperature was calibrated from melting point measurements of In, Sn and Zn. Data were collected using a Pilatus 2M detector. The exposure time was set to 20s and the sample rotated 10° during exposure to improve powdered averaging. 15s were needed to rotate the sample back between the exposures, thus giving a time resolution of 35s. Single crystal reflections from the sapphire tube were masked manually and the data were integrated to 1D diffraction patterns with the program Bubble. The sample-to-detector distances was 446.3 mm and the wavelength was 0.7454 Å, both calibrated from a NIST LaB_6 standard. Measurement were performed while heating the sample under 1 bar Ar from ambient temperature to 180 °C with a heating rate of 5 °C/min and then isothermally at 178 °C. After 12 hours, 88 bar H_2 was introduced into the sample cell and the SR-PXD measurement was continued from another 12 hours.

3.2.7 In-situ MAS ^{11}B NMR

VT MAS ^{11}B NMR data was collected at the Environmental Molecular Sciences Laboratory (EMSL) at the Pacific Northwest National Laboratory (PNNL) at Richland, USA. The characterization of THF-adduct $Mg(BH_4)_2$ during heating to 200 ^oC was conducted by variable temperature (VT) solid state magic angle spin (MAS) NMR in a Varian 500 MHz spectrometer 5 mm HXY probe. ^1H and ^{11}B shifts were referenced to tetramethylsilane at 0 ppm and lithium borohydride at −41.6 ppm and measured at 499.87 and 160.37 MHz respectively. ^1H and ^{11}B spectra were obtained with a 2s and 5s relaxation delay and 90^o pulse width of 6 µs. The sample powder was packed in a 5 mm zirconia rotor under 1 atm N_2 with a Teflon spacer and then capped with a customized plastic bushing capable of withstanding pressures up to 200 bar. The details of the rotor design are given in detail elsewhere[121,127] and have been modified to accommodate 5 mm rotors. The rotors were spun at 5 kHz at room temperature and subsequently heated at a rate of about 6 ^oC/min and held at specific temperatures during the ramp at which ^{11}B and ^1H spectra were obtained. The duration of the analyses at the set temperatures was approximately 45 min.

3.3 Results and Discussion

3.3.1 $Mg(B_3H_8)_2(THF)_3$ synthesis

Follow the same synthesis procedure of the reported $Mg(B_3H_8)_2(THF)_2$ with minor modification in the final drying step, crystalline $Mg(B_3H_8)_2(THF)_3$ was obtained. Solution ^{11}B NMR, taken in D_2O solvent, shows the characteristic nonet resonance of $B_3H_8^-$ at -31 ppm due to the coupling of the boron to the eight time-averaged hydrogens (Figure 3.1).

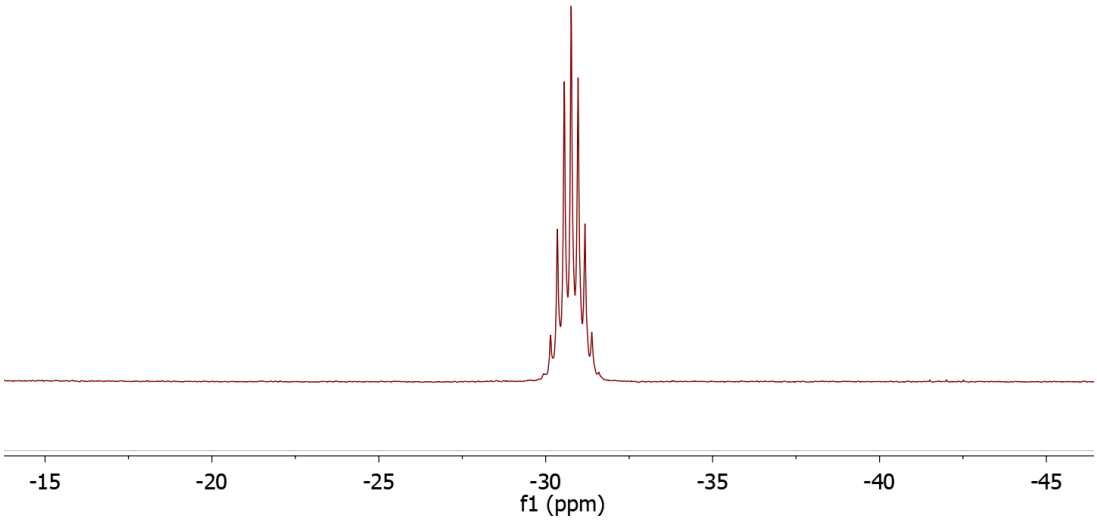

Figure 3.1: Solution ^{11}B of $Mg(B_3H_8)_2(THF)_3$ in D_2O

The ^1H NMR, taken in D_2O, of the product contained the 10-line pattern signal of $B_3H_8^-$ at 0.2 ppm, due to the coupling of the proton to the three equivalent borons (Figure 3.2). Two prominent signals of THF, 1.75 and 3.6 ppm, were also observed besides signal for D_2O solvent at 4.7 ppm. On the basis of ^1H NMR integration the Mg complex had the chemical formula of $Mg(B_3H_8)_2(THF)_3$.

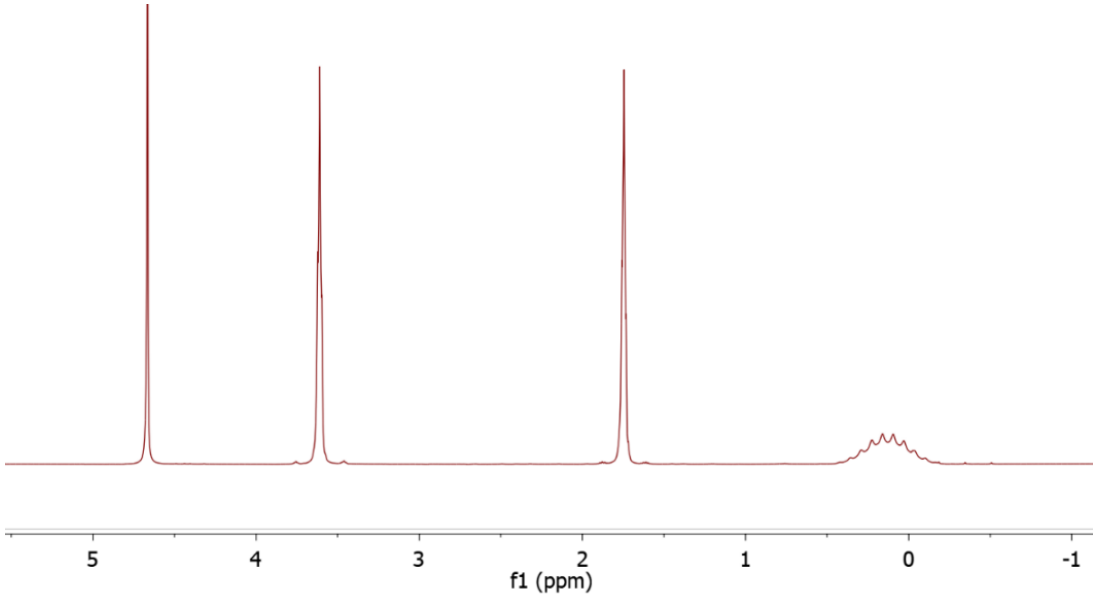

Figure 3.2: Solution ^1H NMR of $Mg(B_3H_8)_2(THF)_3$ in D_2O

3.3.2 $Mg(B_3H_8)_2(THF)_3$ molecular structure

To further understand the molecular structure of the synthesized complex, powder XRD and Rietveld analysis were performed at Pacific Northwest National Laboratory by Dr. Mark Bowden. The crystal structure is shown in Figure 3.3. It is noted that both an octahedral $[Mg(THF)_6]^{2+}$ complex and a tetrahedral edge-on $[Mg(B_3H_8)_4]^{2-}$ complex ions packed in a face-centered cubic (FCC) lattice with cell parameters; a = b = c = 15.275 Å and V = 3564 Å. The $B_3H_8^-$ anions occupy several different orientations due to either static or dynamic disorder. As displayed in Figure 3.6, $B_3H_8^-$ ions are shown face-on to the Mg^{2+}. There are 9 H atoms (B_3H_9) due to crystallographic symmetry, *aka* only 3 H atoms in the same plane as the 3 B atoms as being $^2/_3$ occupied, only 2 of the 3 are there at any one time.

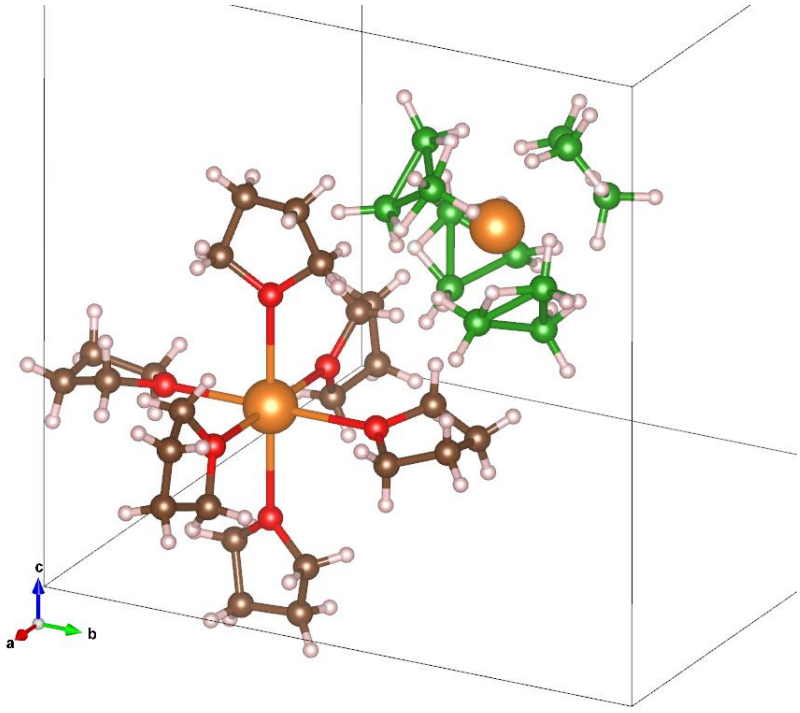

Figure 3.3: Crystal structure of $Mg(B_3H_8)_2(THF)_3$

3.3.3 $Mg(B_3H_8)_2(THF)_3$-2MgH_2 hydrogenation - The revelation of $MgB_{10}H_{10}$ and $Mg[B(OBu)_4]_2$

A 1:2 ball-milled mixture of $Mg(B_3H_8)_2(THF)_3$ and MgH_2 was hydrogenated at 200°C under 5 bar H_2 for 4 hours. Solution $^{11}B\{^1H\}$ NMR, taken in D_2O, of the mixture after hydrogenation contained one resonance at -42 ppm, a characteristic signal of BH_4^-, and a signal at 2 ppm for $Mg[B(OBu)_4]_2$, (Figure 3.4).[87] The solution ^1H NMR, Figure 3.5, of the product showed the formation of BH_4^- with prevalent 4 peak-pattern signal centered δ -0.25. To our surprise, small amount of THF remained after the hydrogenation, signals δ 1.75 and 3.6 ppm. We also observed 4 signals at 1.17, 1.40, 1.68, and 3.50 ppm, corresponds to 3 CH_2 and 1 CH_3 signals of $Mg[B(OBu)_4]_2$, where Bu = C_4H_9. Further synthesis and analysis of the THF-ring-opening species, $Mg[B(OC_4H_9)_4]_2$, is provided in Chapter 4.

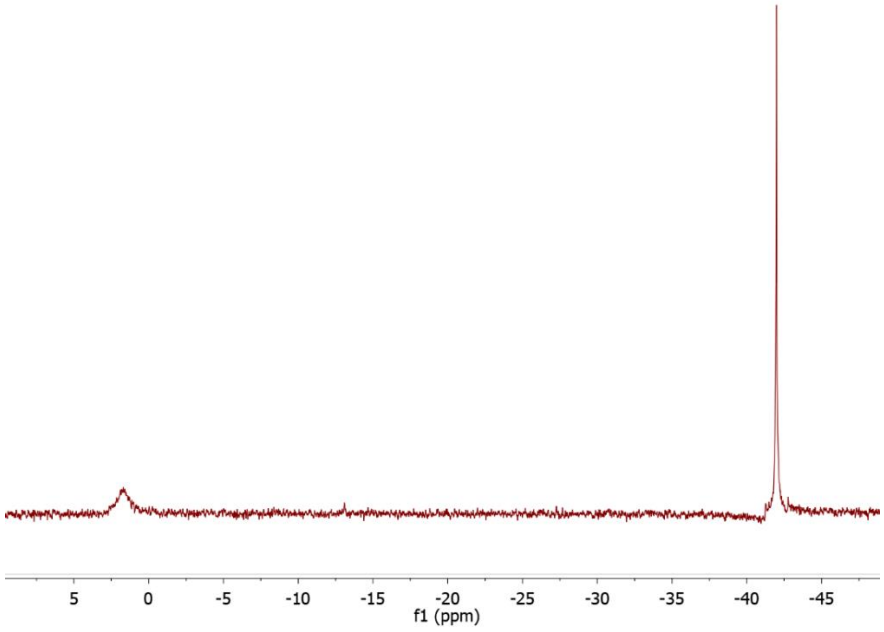

Figure 3.4: Solution $^{11}B\{^1H\}$ NMR of hydrogenated $Mg(B_3H_8)_2(THF)_3$ - 2MgH_2 mixture

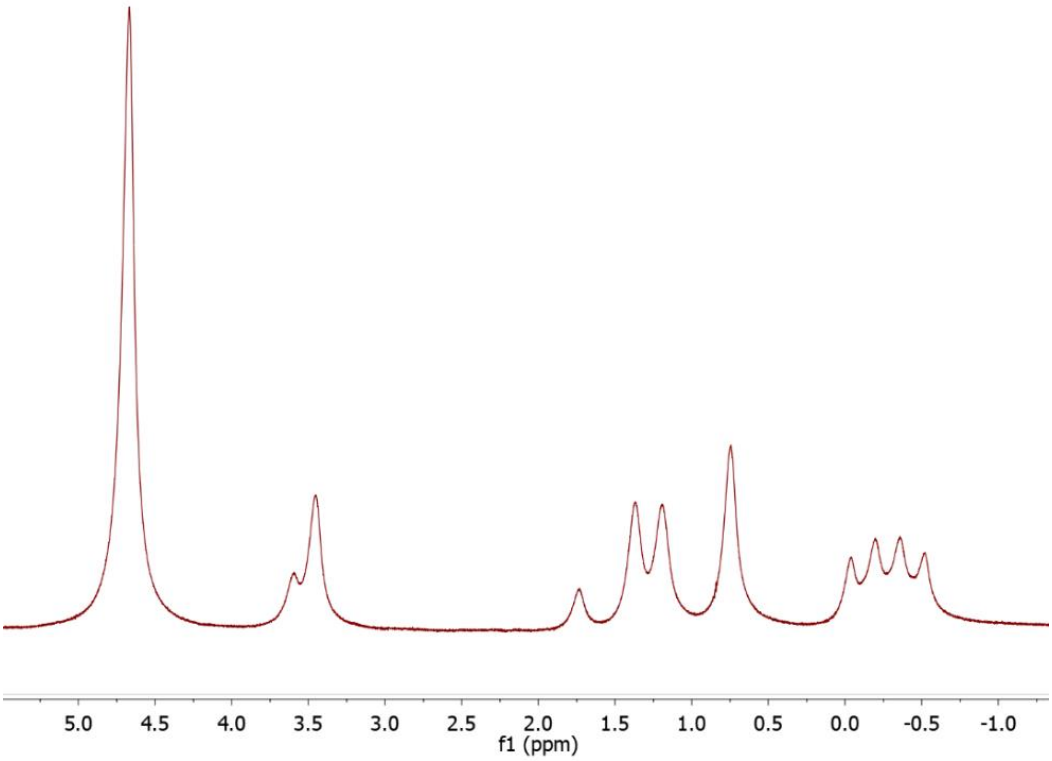

Figure 3.5: Solution ^{1}H NMR in D_2O of hydrogenated $Mg(B_3H_8)_2(THF)_3$ - $2MgH_2$ mixture

In order to test for reversibility of the hydrogenation reaction, the $Mg(BH_4)_2(THF)_x$ product was dehydrogenated at 200 ^{o}C for 24 h under static vacuum. ^{11}B NMR (Figure 3.6) analysis surprisingly indicated that the primary product obtained was $MgB_{10}H_{10}$. Only trace amount of $B_3H_8^-$ was obtained. The high product selectivity for $B_{10}H_{10}^{2-}$ vs. $B_3H_8^-$ and the kinetic enhancement of the dehydrogenation reaction (24 hours versus 5 weeks[83]) were apparently due to the coordination of the THF solvent to $Mg(BH_4)_2$.

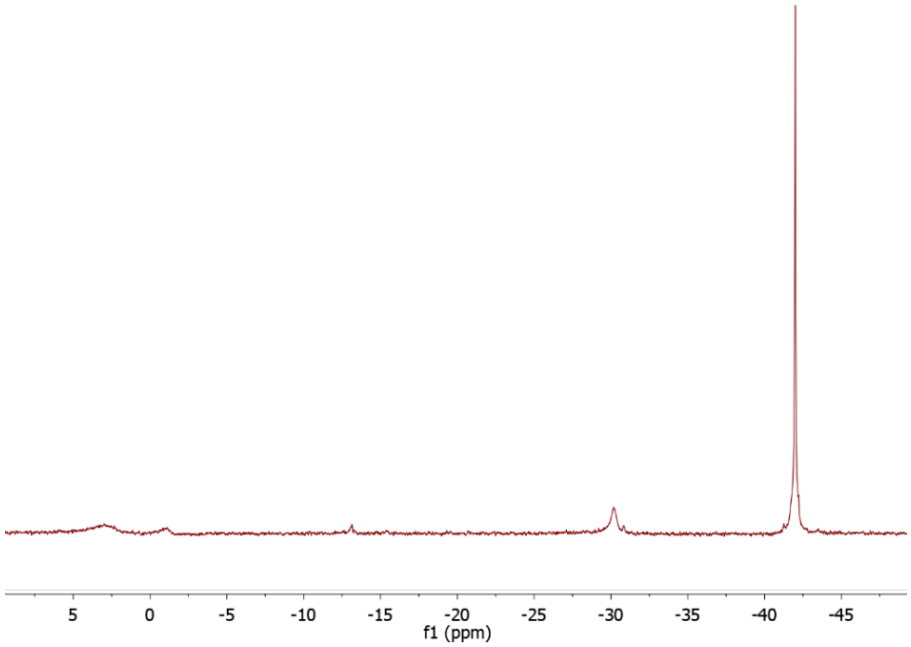

Figure 3.6: Solution $^{11}B\{^{1}H\}$ NMR in D_2O of hydrogenated $Mg(B_3H_8)_2(THF)_3$-$2MgH_2$ followed by dehydrogenation at 200°C for 24 hours

To better understand the role of THF in the hydrogen desorption process, we prepared an array of samples of $Mg(BH_4)_2$ which were treated with a varied amounts of THF (0.25, 0.5, 1, 3 equivalents). Dehydrogenation trials were carried out at 150 °C, 180 °C, and 200 °C. In order to allow direct comparison, dehydrogenation of unsolvated $Mg(BH_4)_2$ was also carried out accordingly at 180 °C under static vacuum as the reference experiment. The resulting distributions borane products were determined by ^{11}B NMR and are shown in Table 3.1. Entry 1 shows that only low reactivity was observed for unsolvated $Mg(BH_4)_2$ at 180°C as 93% the BH_4^- was found to be unreacted. In general, we found that the samples of the THF adducts showed high levels of dehydrogenation at temperatures range from 150 °C to 200 °C, with high selectivity of $MgB_{10}H_{10}$, Heating of $Mg(BH_4)_2(THF)_{0.25}$ at 150 °C under static vacuum for 48 h gave rise to 11% yield of $B_{10}H_{10}^{2-}$, 2%. $B_3H_8^-$, and a trace amount of $B_{12}H_{12}^{2-}$. It is notable that highest conversion to

$B_{10}H_{10}^{2-}$, 68%, was achieved at 200 °C after 48 hours. However, 13% conversion to $B_3H_8^-$ was also observed. The high selectivity for the formation of $B_{10}H_{10}^{2-}$ rather than $B_{12}H_{12}^{2-}$ was also found for dehydrogenation of $Mg(BH_4)_2(THF)_{0.5}$ and only 8% conversion to $B_3H_8^-$ was observed. Despite the high selectivity for $B_{10}H_{10}^{2-}$, for the presence of $B_3H_8^-$ in all product mixtures suggests a competing dehydrogenation pathway.

We probed whether a hydrogen back pressure would subside the competing reaction pathway leading to $B_3H_8^-$ formation. Starting with $Mg(BH_4)_2(THF)_{1.0}$, 50% conversion to $B_{10}H_{10}^{2-}$ was observed upon dehydrogenation of at 200 °C under 4 bar H_2 for 3 hours. This finding indicates that the formation of $B_3H_8^-$ but not $B_{10}H_{10}^{2-}$ can be suppressed a modest over pressure of hydrogen.

Table 3.3: *Borane species of $Mg(BH_4)_2(THF)_x$ ($x = 0.25$ - 3) after dehydrogenation*

		Amount/Mol%								
		Species / δ ^{11}B (ppm)							**NMR solvent**	
Sample	**Conditions**	$B(OBu)_4^-$ (3)	$[B_{10}H_{10}]^{2-}$ (0 & -30)	-13 ppm	$B_{12}H_{12}^{2-}$ (-15)	-27 ppm	$B_3H_8^-$ (-31)	BH_4^- (-41)	D_2O	$2D_2O$/THF
$Mg(BH_4)_2$	180 °C-24h-static vacuum	3	-	-	-	-	4	93	x	
$Mg(BH_4)_2(THF)_{0.25}$	150 °C-48h-static vacuum	24	11	1	2	-	-	62	x	
$Mg(BH_4)_2(THF)_{0.25}$	200 °C-48h-static vacuum	13	68	1	1	4	13	-	x	
$Mg(BH_4)_2(THF)_{0.5}$	200 °C-48h-static vacuum	27	52	-	-	-	8	13	x	
$Mg(BH_4)_2(THF)$	180 °C-24h-4bar H_2	-	31	7	-	-	-	62		x
$Mg(BH_4)_2(THF)$	200 °C-24h-4bar H_2	-	54	3	4	-	-	39		x
$Mg(BH_4)_2(THF)$	200 °C-3h-4bar H_2	-	50	-	1	-	-	49		x
$Mg(BH_4)_2(THF)_3$	200 °C-48h-static vacuum	8	13	3	-	-	-	76	x	

Clearly, a contributing factor to kinetic enhancement of the dehydrogenation of the $Mg(BH_4)_2(THF)_x$ may the melting of the complex. The Differential Scanning Calorimetry data of $Mg(BH_4)_2(THF)_{0.5}$ (Figure 3.7) obtained by the group of Dr. Thomas Gennett at the National Renewable Energy Laboratory (NREL) shows two endothermic features at 45 ^oC and 100 ^oC, corresponding to phase changes, one of which being the melting of the material. We have visually studied the melting phenomenon of the THF solvate using melting point apparatus, which confirmed the transformation form a microcrystalline power to a super-viscous melt between 80-100 ^oC, which is much below the observed requisite temperature for the onset of dehydrogenation. This is underscored by the NREL DSC study in which the onset of dehydrogenation was not observed until 250 ^oC. The NREL experiment utilized an aggressive, 5˚C/min ramping of temperature, which given the relative slow rate of hydrogen elimination from the material, may have result in an indication of an artifactually high temperature required to induced hydrogen release. However, it is clear the while the kinetics of hydrogen release are promoted in a melt, the melting of the material alone is does not induce hydrogen release. Thus, THF apparently reduces the activation energy of clustering to form more deeply dehydrogenated products by altering the coordination mode between Mg^{2+} and borane intermediates as shown in Chapter 2. It is also likely that THF coordination with BH_3 may also play a role the observed kinetic enhancement of the dehydrogenation of BH_4^- to $B_{10}H_{10}^-$.

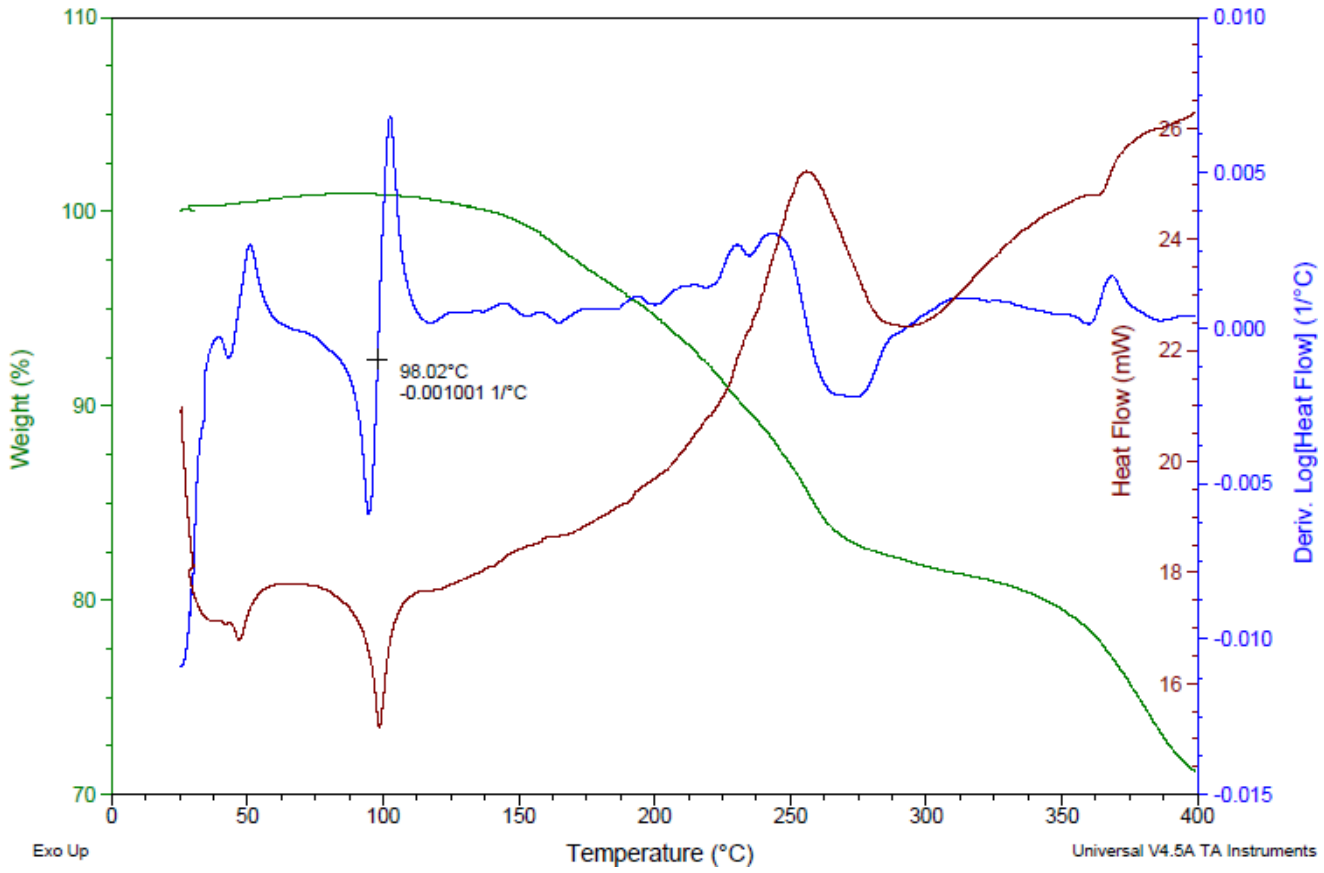

Figure 3.7: TGA-DSC of $Mg(BH_4)_2(THF)_{0.5}$

3.3.4 In-situ de-/re-hydrogenation studies of $Mg(BH_4)_2(THF)$

The melting observation of $Mg(BH_4)_2(THF)_{0.5}$ (Figure 3.7) was observed at 100 ^oC, however, dehydrogenation did not take place until 150 ^oC with reasonable kinetics were observed at 180 ^oC and 200 ^oC. This piqued our interest to further investigate phase changes in this material and their role in lowering the temperature for H_2 release, thus, we carried out an *in-situ* Powder Synchrotron X-Ray study in collaboration with the Norwegian Institute for Energy Research (IFE). The results of this study are presented in Figure 3.4. The as prepared THF-solvated $Mg(BH_4)_2$ showed good crystallinity and the Bragg peaks at room temperature, denoted as Phase 1, can be indexed as monoclinic unit cell (Figure

3.8a). Upon heating to 75 °C, Phase 1 underwent rapid transformation to a new phase, Phase 2. It can also be indexed on a monoclinic unit cell with virtually identical volume (1448.5 $Å^3$ for Phase 1 vs 1456.6 $Å^3$ for Phase 2), indicating a phase transition and not a desorption event. Soon after the complete transformation to Phase 2, the sample turned amorphous at 83 °C. The material stayed amorphous up to 180 °C and for 8 hours at the isothermal stage at 180 °C. The nature of the diffuse scattering from the amorphous sample, however, changed significantly in this period, indicating that short range structural changes take place in the amorphous state (Appendix, Figure S1). About 10 hours into the isothermal step, a new phase (Phase 3) started to crystallize. The crystalline did not change further after additional 2 hours at 180 °C (Figure 3.8b). The obtained *in-situ* Powder X-Ray data was encouraging as it verified the phase change observation of $Mg(BH_4)_2(THF)_{0.5}$ at 60 °C in the DSC, followed by melting observed at 100 °C, and hydrogen release at *ca* 250 °C (Figure 3.7).

a)

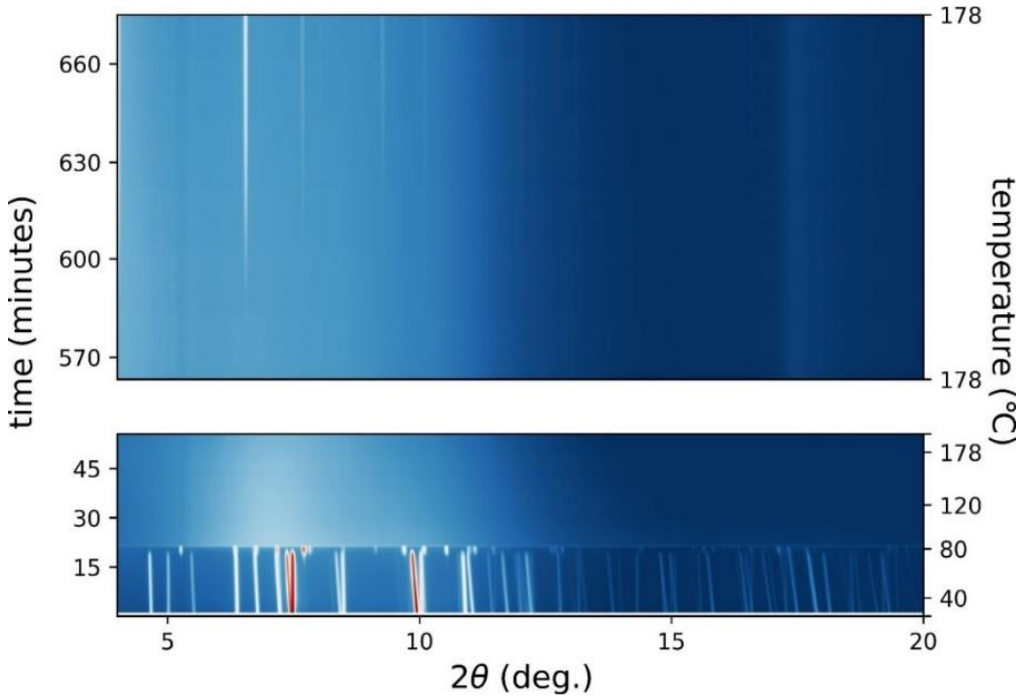

b)

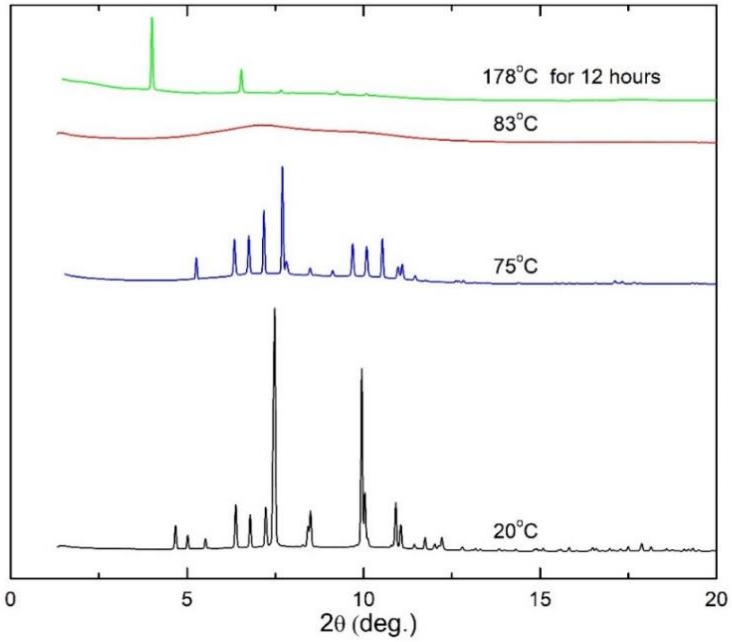

Figure 3.8: a) *In-situ* Powder X-Ray of THF-solvated $Mg(BH_4)_2$ b) X-Ray Powder Diffraction patterns of THF-solvated $Mg(BH_4)_2$ at different temperatures

We also conducted an *in-situ* MAS ^{11}B NMR study in collaboration with PNNL to follow the physical changes to the THF-adduct $Mg(BH_4)_2$ as a function of temperature to compare with the obtained DSC and XRD results. As shown in Figure 3.9, there appeared a set of complex boron resonances, one centered at -41 ppm and another pair centered at -44 ppm, indicated a mixture of BH_4^- phases existed at room temperature. The sealed rotor containing the THF-solvated $Mg(BH_4)_2$ was subsequently heated in stages and the ^{11}B NMR spectra were collected at 60, 120, 150, 180, and 200 ^oC. At 60 ^oC, the two peaks observed at room temperature began to decrease in amplitude and further coalesced into the concomitant signal of a larger lone BH_4^- peak at 120 ^oC. Heating to 150, 180, and finally 200 ^oC shows THF-solvated $Mg(BH_4)_2$ sample appears to be the predominant species.

These results indicated that room temperature the sample initially consists of serval phases of $Mg(BH_4)_2(THF)_x$ which convert to a single molten phase by 120 ˚C.

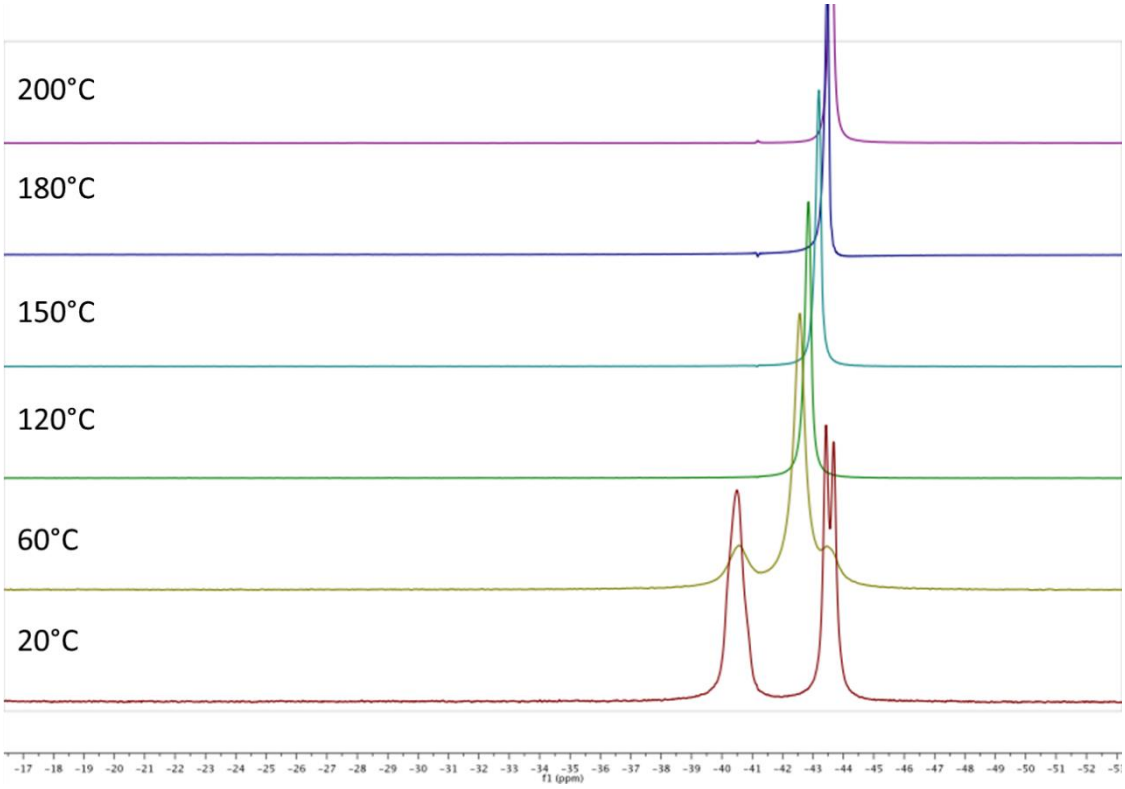

Figure 3.9: *In-situ* VT MAS ^{11}B NMR of THF-solvated $Mg(BH_4)_2$ at various temperatures

3.4 Conclusion

The dehydrogenation of unsolvated/ pure $Mg(BH_4)_2$ requires relatively high temperatures (~500 ˚C) to discharge its full hydrogen content to give MgB_2. At least dehydrogenation to $Mg(B_3H_8)_2$ can be accomplished at the less extreme temperature of 250 ˚C but the reaction slow, requiring weeks and releases at best 2.5 wt % hydrogen which is insufficient for onboard vehicular applications. We have found that upon solvating with sub-stoichiometric amounts of THF, dehydrogenation becomes rapid at 180 ^oC. Dehydrogenation from the molten THF complex is accomplished in 3 hours vs. 5 weeks. Additionally, the reaction becomes highly selectivity for $B_{10}H_{10}^{2-}$ rather than $B_3H_8^-$

(theoretical H_2 release 8.1 wt% vs. 2.5 wt.% in the absence of solvates), and produces only traces amounts of $B_{12}H_{12}^{2-}$, a kinetic and thermodynamic dead end. The use of hydrogen back pressure for the dehydrogenation study suppresses the competing dehydrogenation pathway, forming $B_3H_8^-$. I*n situ* synchrotron X-ray diffraction further verified the transformation of this material to an amorphous phase at 83 ˚C and also revealed a solid-state phase change at 75 ˚C as well as the emergence of a crystal phase from the amorphous phase upon prolonged heated and dehydrogenation. In summary, $Mg(BH_4)_2(THF)$ undergoes rapid dehydrogenation to $MgB_{10}H_{10}$ at moderate conditions. In view, of the observed rapid dehydrogenation kinetics high, 8.1 hydrogen cycling potential of $MgB_{10}H_{10}$, this material could potential be utilized in practical hydrogen storage applications. Our exploration of the reversibility of $MgB_{10}H_{10}$ species back to $Mg(BH_4)_2$ is the subject of Chapter 5.

CHAPTER 4: INVESTIGATION OF THE POSSIBLE INVOLVEMENT OF MAGNESIUM TETRABUTOXYBORATE IN THE $Mg(BH_4)_2/MgB_{10}H_{10}$-$MgH_2$ HYDROGEN CYCLING SYSTEM

4.1 Introduction

Chapter 3 describes the selective dehydrogenation of $Mg(BH_4)_2(THF)_x$ to $MgB_{10}H_{10}$ at 180-200 ^oC. We further observed formation of an additional product which was tentatively assigned this species as $Mg[B(OBu)_4]_2$ on the basis of its ^1H and ^{11}B NMR. We proposed that this product arises from attack of the THF by BH_4^- which results in formation of a B-O bond and ring opening of the ether as seen in Scheme 4.1. This raises the question as to whether $Mg[B(OBu)_4]_2$ acts as a promoter of the reversible dehydrogenation of $Mg(BH_4)_2(THF)_x$. This possibility is of further interest in light of the industrially important Brown-Schlesinger process for the production of $NaBH_4$ in which NaH is reacted with $B(OCH_3)_3$ or $NaB(OCH_3)_4$.[135] In order to test this hypothesis, we independently synthesized and characterized of $Mg[B(OBu)_4]_2$, and explored the utilization of this species as a promoter for the re-hydrogenation of $MgB_{10}H_{10}$ to $Mg(BH_4)_2$.

4.2 Experimental

All sample preparations and handling were conducted in a nitrogen glovebox or on a Schlenk line. Solvents were purified by a SPS system or distilled over a drying agent if required.

4.2.1 Synthesis of $Mg(OBu)_2$ (Bu = C_4H_9)

In a N_2 glovebox or using a Schlenk apparatus, 1g of Mg (41 mmol) was added to 15 mL 1-butanol (164 mmol). The mixture was heated to 150 ^oC for 8 hours with vigorous stirring, upon which the white precipitate formed gradually. The solution was allowed to cool to room temperature and the white precipitate of magnesium butoxide was isolated by filtration using coarse size frit filter followed by drying under vacuum overnight at 50 ^oC.

4.2.2 Synthesis of $Mg[B(OBu)_4]_2$

100 mg $Mg(OBu)_2$, 50 mg $B(OH)_3$ (1:1 molar ratio) and 20 mL 1-butanol were mixed together in a Schlenk flask. The mixture was refluxed at 150 ^oC for 72 hours and allowed to cool to room temperature. Final solution was filtered through a medium size frit filter in which the white precipitate was collected.

4.2.3 Preparation of $Mg(BH_4)_2$ with $Mg[B(OBu)_4]_2$

0.05 g $Mg(BH_4)_2$ was ballmilled with 0.15 g $Mg[B(OBu)_4]_2$ (4:1 molar ratio) at 300 RPM, for 30 minutes (5 minutes/cycle*6 cycles, 1 minute rest, reverse direction).

4.2.4 Preparation of $Mg[B(OBu)_4]_2$ with MgH_2

0.32 g $Mg[B(OBu)_4]_2$ was ballmilled with 0.05 g MgH_2 (1:4 molar ratio) at 300 RPM, for 30 minutes (5 minutes/cycle*6 cycles, 1 minute rest, reverse direction).

4.2.5 PCT isothermal de-/re-hydrogenation of THF-adduct $Mg(BH_4)_2$

De-/re-hydrogenation studies were carried out isothermally on a Suzuki Shokan PCT-2SDWIN Sievert type apparatus. Precise temperature control was achieved using customized heating mantle sleeves. Reactors with fixed volumes were filled with 4 bar H_2 back pressure prior to dehydrogenation. Appropriate hydrogen pressures were introduced to the reactors for hydrogenation experiments.

4.3 Results and Discussion

4.3.1 Proposed mechanism for the formation of $Mg[B(OBu)_4]_2$

The $Mg[B(OBu)_4]_2$ was proposed to arise from the THF ring opening due to BH_4^- attack (Scheme 4.1). Aided by heat, BH_4^- attacks the THF alpha carbon, resulting in ring opening to butoxide concerted with O lone pair attack on B leading to the formation of a B-O-Bu moiety. This process repeats until all hydrides on the borohydrides are replaced by butoxide groups to generate the tetrabutoxyborate anion species.

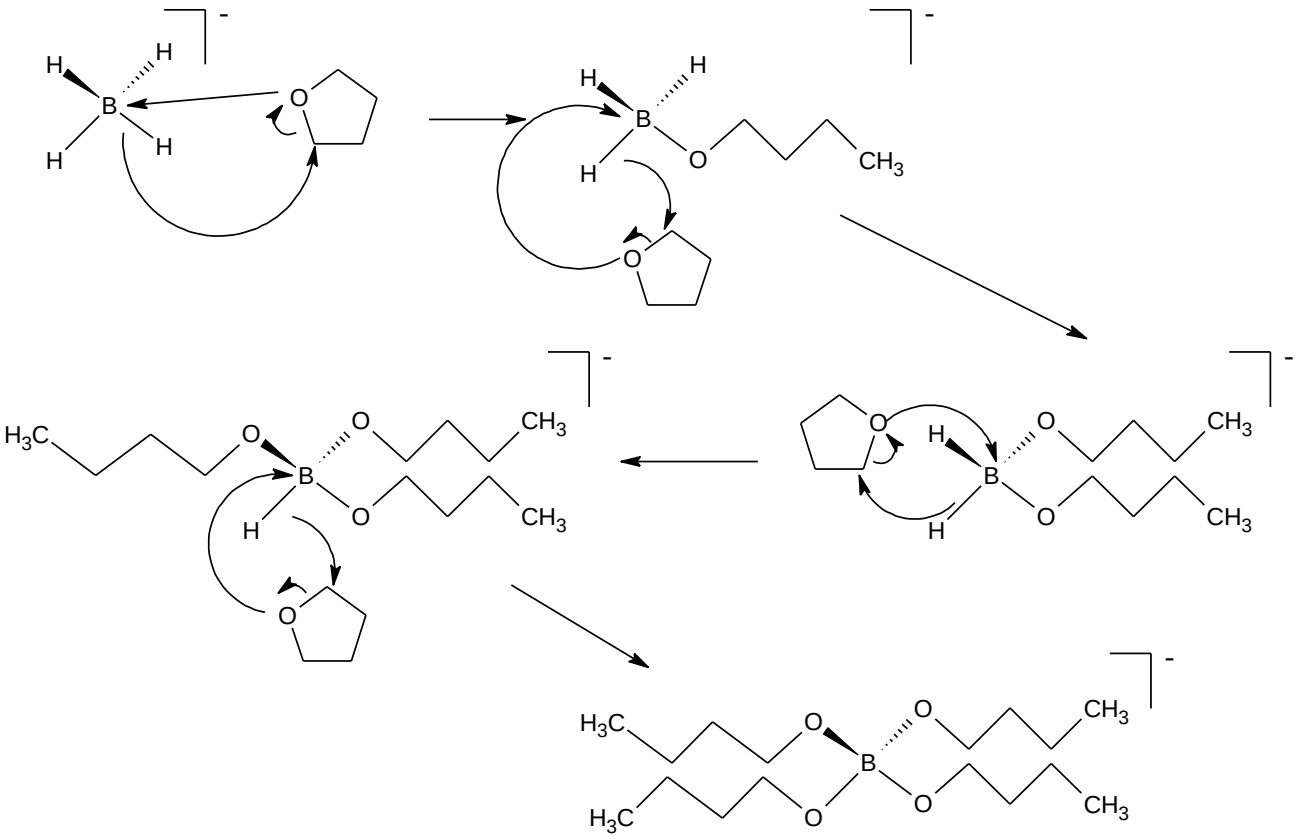

Scheme 4.1: Proposed formation mechanism of $B(OC_4H_9)_4^-$ species

4.3.2 Attempts to cycle between $Mg(BH_4)_2$ and $MgB_{10}H_{10}$ using $Mg[B(OBu)_4]_2$

4.3.2.1 Synthesis and characterization of $Mg[B(OBu)_4]_2$

The preparation of alkali metal alkoxides using alkali metals and corresponding alcohols have been reported in the literature.[119] Our subsequent modification of the method to yield the magnesium butoxide complex followed the reaction:

$$Mg + 2(1\text{-butanol}) \longrightarrow Mg(OBu)_2 + H_2 \qquad \textbf{(4.2)}$$

Due to the low reactivity of alkaline metal relative to the alkali metals, heating and vigorous stirring were necessary to drive the reaction to completion. The isolated $Mg(OBu)_2$ after filtration was mixed with boric acid in *n*-butanol followed by refluxing at

150 °C for 72 hours. The final product, $Mg[B(OBu)_4]_2$ was analyzed using solution ^1H NMR in D_2O (Figure 4.1), displayed 4 characteristic signals, δ 0.79 (t, C**H**$_3$), δ 1.24 (sex, C**H**$_2$), δ 1.42 (quin, C**H**$_2$), δ 3.50 (t, C**H**$_2$) and $^{11}B\{^1H\}$ NMR in D_2O, δ 1.65 (s, $B(OBu)_4^-$ (Figure 4.2).

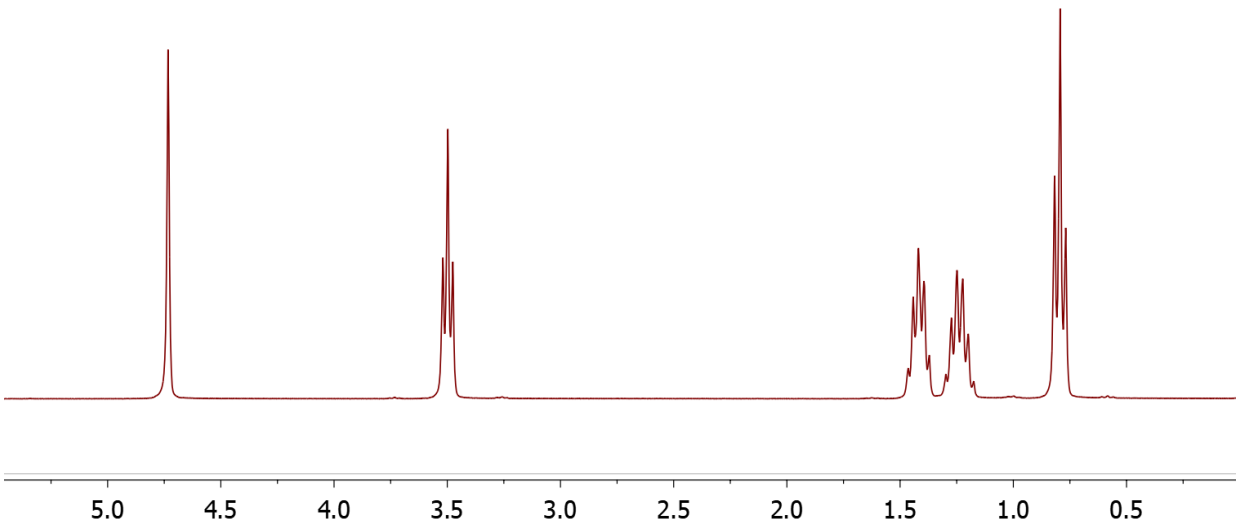

Figure 4.1: Solution ^1H NMR of $Mg[B(OBu)_4]_2$ in D_2O

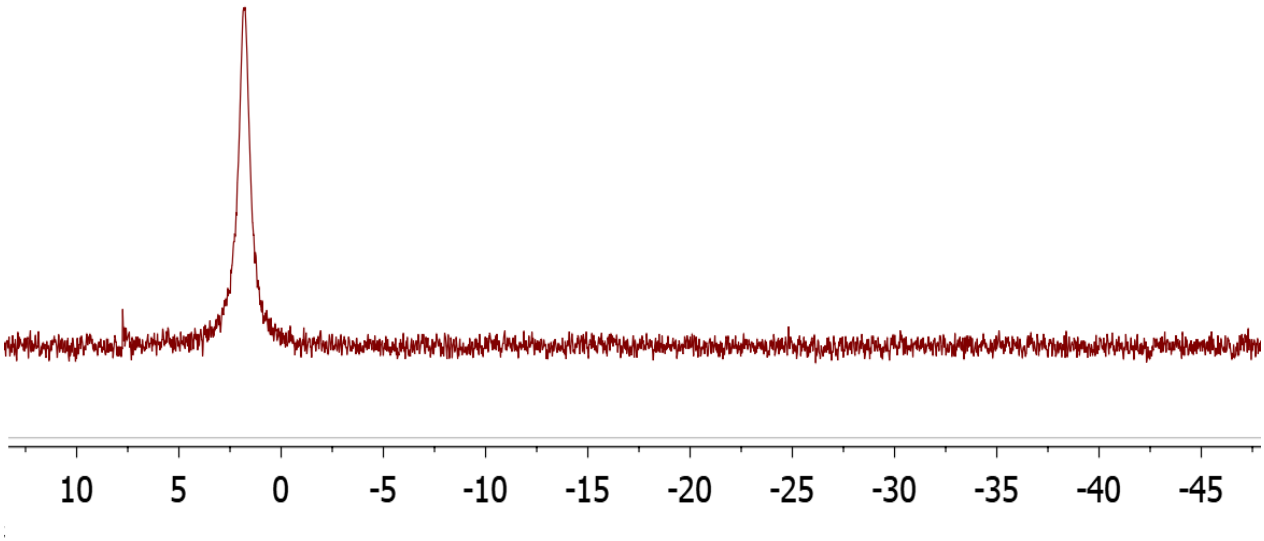

Figure 4.2: Solution $^{11}B\{^1H\}$ NMR of $Mg[B(OBu)_4]_2$ in D_2O

4.3.2.2 Cycling studies using $Mg[B(OBu)_4]_2$

Our initial attempts to use $Mg[B(OBu)_4]_2$ in place of THF for the dehydrogenation of $Mg(BH_4)_2$ to $MgB_{10}H_{10}$ were plagued with the contamination of *n*-butanol in the the borate product. Rigor removal *n*-butanol was achieved by heating the tetrabutoxyborate to 120 ˚C for 24 h under high vacuum.

A ball-milled mixture of $Mg(BH_4)_2$ and $Mg[B(OBu)_4]_2$ was dehydrogenated for 24 hours at 180 ^oC, followed by ^{11}B NMR characterization. A mixture of $B_{10}H_{10}^{2-}$ (δ 0 & -30 ppm) and $B_3H_8^-$ (δ -31 ppm) was observed besides BH_4^- (δ -42 ppm) (Figure 4.3). Upon further drying $Mg[B(OBu)_4]_2$ off *n*-butanol, no borane products were observed after prolonged heating of $Mg[B(OBu)_4]_2$ and $Mg(BH_4)_2$ mixture at 180 ^oC.

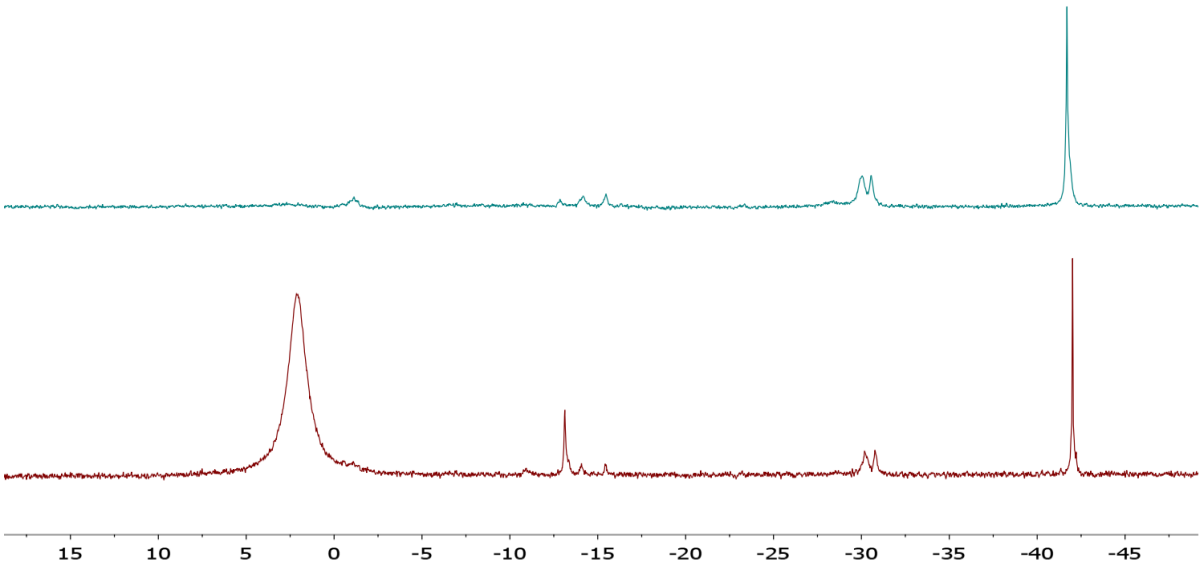

Figure 4.3: Solution $^{11}B\{^1H\}$ NMR of $Mg(BH_4)_2$ and $Mg[B(OBu)_4]_2$ after 24 hours at 180 ^oC a) in D_2O solvent b) in D_2O/THF

We further attempted to utilize *n*-butanol to promote hydrogen release from $Mg(BH_4)_2$. An equimolar mixture of $Mg(BH_4)_2$ / *n*-butanol first melted upon heating to 80 ^oC, then solidified at 120 ^oC. The mixture has then further heated to 180 ^oC for 24 hours.

Solution $^{11}B\{^{1}H\}$ NMR analysis indicated the product mixture to consist of over 80% $[B(OBu)_4]^-$, along with minor amounts of $B_{10}H_{10}^{2-}$ and BH_4^-. An attempt to reverse the generated $B_{10}H_{10}^{2-}$ was unsuccessful.

4.3.3 Dehydrogenation ballmilled mixture of $Mg[B(OBu)_4]_2$ and MgH_2

A ball-milled mixture of $Mg[B(OBu)_4]_2$ and MgH_2 (1:4 molar ratio) was dehydrogenated for 24 hours at 200 ^oC. The ^{11}B NMR spectrum of the product mixture contained only a signal for $Mg[B(OBu)_4]_2$ at 2 ppm. Notably, no trace of signal for BH_4^- at δ -41 ppm was observed.

4.4 Conclusions

Attempts to cycle between $Mg(BH_4)_2$ and $MgB_{10}H_{10}$ in the presence of independently synthesized, rigorously purified $Mg[B(OBu)_4]_2$ were unsuccessful. Notabilty, no reaction was found to occur between $Mg[B(OBu)_4]_2$ and MgH_2. Furthermore, no melting was observed for mixture of $Mg(BH_4)_2$ and $Mg[B(OBu)_4]_2$ upon heating. We conclude that the $Mg[B(OBu)_4]_2$ that is generated through the ring-opening side reaction of excess THF in the initial solid state dehydrogenation of $Mg(BH_4)_2(THF)_x$ plays no role in its subsequent moderate temperature, reversible dehydrogenation to $MgB_{10}H_{10}$.

CHAPTER 5: HYDROGENATION STUDIES OF THE INTERMEDIATE SPECIES $MgB_{10}H_{10}$

5.1 Introduction

Studies of the reversible dehydrogenation of $Mg(BH_4)_2$/ $Mg(B_3H_8)_2$ under moderate conditions highlighted the work of Chong *et al*.[83] Isothermal decomposition of $Mg(BH_4)_2$ for 5 weeks at 200 ^oC resulted in the selective formation of $Mg(B_3H_8)_2$, which could be re-hydrogenated completely back to $Mg(BH_4)_2$ at 250 ^oC under 120 bar H_2. The cycling between $Mg(BH_4)_2$ and $B_3H_8^-$ (2.5 wt.%) is promising, however, the rate for H_2 release and uptake is extremely slow, requiring long reaction or high temperatures and pressures.[82,83,127] Reports of extra measures to purify $Mg(BH_4)_2$ to assure formation of fewer impurities in the released H_2 upon dehydrogenation have also appeared.[127,128] However, the impurities appear to lower the reaction conditions and enhance the reaction kinetics.[87] Most notably, the hydrogenation of $Mg(B_3H_8)_2(THF)_2$ and MgH_2 to $Mg(BH_4)_2$ can be accomplished at 200 ^oC for 2 hours under 50 bar H_2.[130] Also as reported in Chapter 3, the selective formation of $[B_{10}H_{10}]^{2-}$ was observed upon dehydrogenation of $Mg(BH_4)_2(THF)_x$ (x = 0.25-3). Hydrogen cycling between BH_4^- and $B_{10}H_{10}^{2-}$ has a potential hydrogen cycling capacity of 8.1 wt.% H_2 and possesses favorable thermodynamics conducive to regeneration at moderate temperatures and pressures. Thus, we were highly motivated to explore this possibility.

Initial attempts at regenerations were frustrating and plagued with irreproducible results. To gain better insight that might allow consistency, we undertook a variety of studies aimed at developing a reliable procedure to enable hydrogen cycling.

5.2 Experimental

All sample preparations and handling were conducted in a nitrogen glovebox or on a Schlenk line. Solvents were purified by a SPS system or distilled over a drying agent if required.

5.2.1 Preparation of $MgB_{10}H_{10}$ with excess MgH_2

$Mg(BH_4)_2(THF)$ was dehydrogenated at 200 ^oC for 48 hours followed by washing with 3 aliquots of THF (~5 mL/wash) to remove soluble $Mg(BH_4)_2$. The after-washed material was dried under vacuum for 2 hours, subsequently analyzed by solution ^{11}B NMR for amount of $MgB_{10}H_{10}$. Pre-activated MgH_2 (450 RPM, 5 mins/cycle*24 cycles, 1 min rest, reverse direction) was added to $MgB_{10}H_{10}$, 10:1 molar ratio. The mixture was ball-milled at 300 RPM for 30 mins (5 mins/cycle for 6 cycles, 1 min rest, reverse direction) prior to hydrogenation studies.

5.2.2 Preparation of $Mg(BH_4)_2$ with $Mg[B(OBu)_4]_2$

0.05 g $Mg(BH_4)_2$ was ball-milled with 0.15 g $Mg[B(OBu)_4]_2$ (4:1 molar ratio) at 300 RPM, for 30 minutes (5 mins/cycle*6 cycles, 1 min rest, reverse direction).

5.2.3 PCT isothermal de-/re-hydrogenation of THF-adduct $Mg(BH_4)_2$

Dehydrogenation/re-hydrogenation studies were carried out isothermally on a Suzuki Shokan PCT-2SDWIN Sievert type apparatus. Precise temperature control was achieved using customized heating mantle sleeves. Reactors with fixed volumes were filled

with 4 bar H_2 back pressure prior to dehydrogenation. Appropriate hydrogen pressures were introduced to the reactors for hydrogenation experiments.

5.3 Results and Discussion

5.3.1 Initial Attempts to Re-hydrogenate $MgB_{10}H_{10}/MgH_2$

5.3.1.1 Re-hydrogenation of $MgB_{10}H_{10}$* without excess MgH_2

$MgB_{10}H_{10}$* ($MgB_{10}H_{10}$* = mixture of $MgB_{10}H_{10}$ + $4MgH_2$ + $Mg(BH_4)_2(THF)$) obtained from the dehydrogenation of $Mg(BH_4)_2(THF)$ (48 hours, 200 ^oC, 1 bar N_2) was placed under 110 bar H_2 and heated to 200^oC for 24 hours. Analysis of the resulting mixture by $^{11}B\{^1H\}$ NMR spectroscopy revealed no change in the relative integrated intensities of the signals for $B_{10}H_{10}^{2-}$ and BH_4^-, indicating no re-hydrogenation had occurred. Similarly, an attempt was made to re-hydrogenate a sample of $MgB_{10}H_{10}$* was ball-milled at 300 RPM, 5 mins/cycles*6 cycles, 1 min rest, reverse direction. The sample was placed under 110 bar H_2 and heated to 200^oC for 24 hours. Again, the $^{11}B\{^1H\}$ NMR spectrum (Fig. 5.1) revealed no change in the relative integrated intensities of the signals for $B_{10}H_{10}^{2-}$ and BH_4^-, indicating no re-hydrogenation had occurred (Table 5.1).

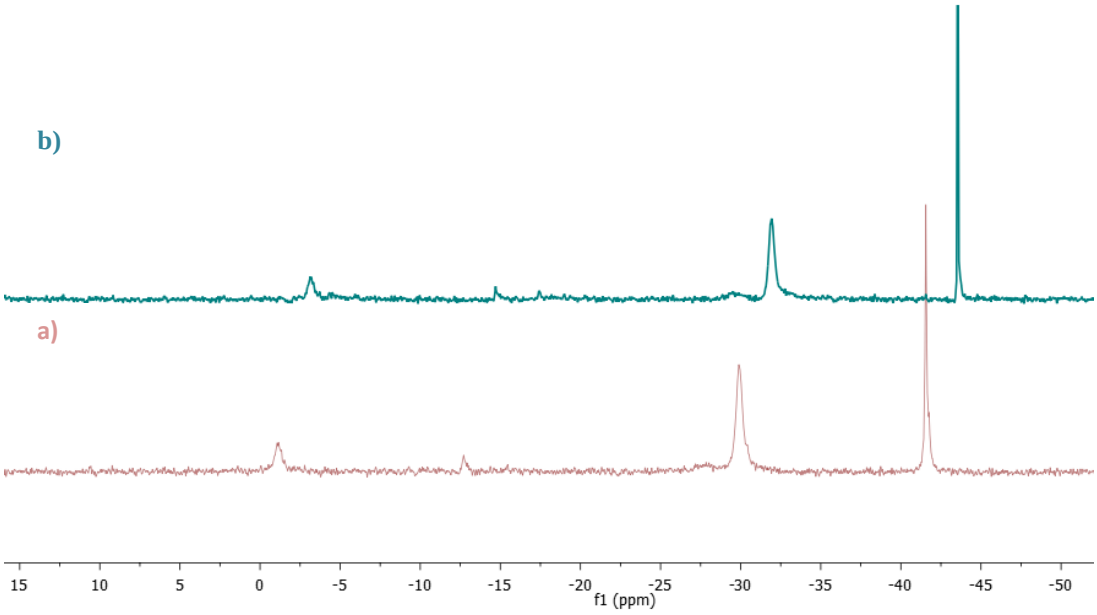

Figure 5.1: $^{11}B\{^{1}H\}$ NMR of a) Ballmilled-$MgB_{10}H_{10}$* b) Ballmilled $MgB_{10}H_{10}$* after attempted re-hydrogenation at 200°C for 24 hours under 110 bar H_2

Table 5.1: *% borane species based on solution $^{11}B\{^{1}H\}$ integration (in $2D_2O$/THF)*

Sample	**Conditions**	**Amount/Mol% Species / δ ^{11}B (ppm)**					
		$B(OBu)_4^-$ (2)	$[B_{10}H_{10}]^{2-}$ (0 & -30)	$[B_{12}H_{12}]^{2-}$ (-15)	$[BH_4]^-$ (-42)	$[B_3H_8]^-$ (-31)	Other
Ballmilled-$MgB_{10}H_{10}$*	**300 RPM, 5 min*6 cycles, 1 min rest**	-	64	-	36	-	-
Rehyd.-Ballmilled mixture	**200°C – 24 hours - 110 bar H_2**	-	64	-	36	-	-

5.3.1.2 Re-hydrogenation of $MgB_{10}H_{10}$* with excess MgH_2

Crystalline phases of $MgB_{10}H_{10}$ nor MgH_2 were observed in the powder XRD of $MgB_{10}H_{10}$*. We hypothesized that upon cooling, MgH_2 becomes tightly associated with $MgB_{10}H_{10}$ and forms a single crystalline phase. The stability of this phase of $MgB_{10}H_{10}$* hindered the re-hydrogenation back to $Mg(BH_4)_2$. We introduced excess MgH_2 to $MgB_{10}H_{10}$* in an attempt to regenerate a non-associated melt and promote the hydrogen

uptake of the material. A 1:10 molar ratio mixture of $MgB_{10}H_{10}$* (THF-washed to remove soluble $Mg(BH_4)_2$) and activated MgH_2 (300 RPM, 5 mins/cycle*6 cycles, 1 min rest, reverse direction) was ball-milled under N_2 for 30 minutes using stainless steel vessel. The ball-milled material was place under 110 bar H_2 of hydrogen and heated to 200 ^oC for 24h. The results of the solution ^{11}B NMR (Figure 5.2) analysis of the sample before and after hydrogenation is summarized in Table 5.2. It is apparent that hydrogenation occurred as there is a significant change in the relative integrated intensities of the signals for $B_{10}H_{10}^{2-}$ and BH_4^- 59:41 and 34:66, before and after respectively. Thus 25% of the boron in the sample was hydrogenated from $B_{10}H_{10}^{2-}$ to BH_4^- representing a realization of 2.0 of the theoretical 8.1 wt % gravimetric hydrogen capacity of the borane ion.

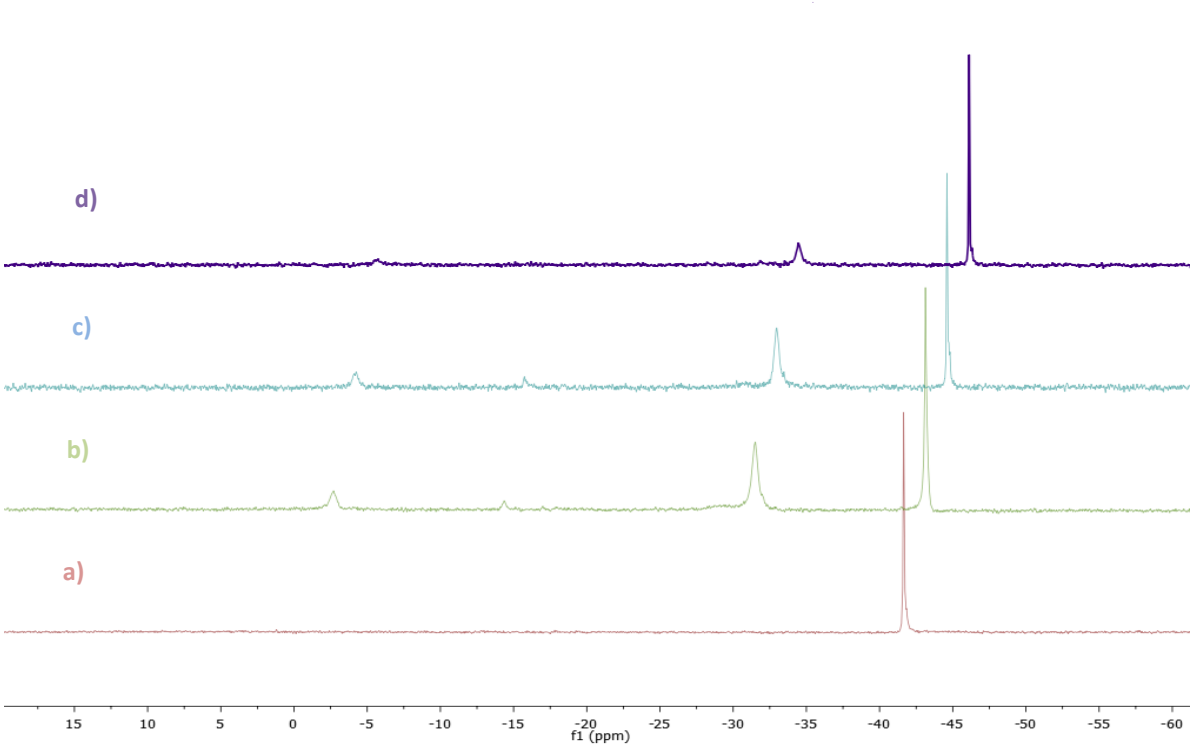

Figure 5.2: Solution $^{11}B\{^1H\}$ NMR in $2D_2O$ / THF of a) $Mg(BH_4)_2$ b) $Mg(BH_4)_2(THF)$ – 200°C – 48h – 1 bar N_2 c) Ballmilled $MgB_{10}H_{10}$* + 10 MgH_2 d) Mixture after rehydrogenation – 200°C – 24h- 110 bar H_2

Table 5.2: *% borane species based on solution $^{11}B\{^{1}H\}$ integration (in $2D_2O$/THF)*

Sample	Conditions	Amount/Mol% Species / δ ^{11}B (ppm)					
		$B(OBu)_4^-$ (2)	$[B_{10}H_{10}]^{2-}$ (0 & -30)	$[B_{12}H_{12}]^{2-}$ (-15)	$[BH_4]^-$ (-42)	$[B_3H_8]^-$ (-31)	Other
Ballmilled-$MgB_{10}H_{10}$* + 10 MgH_2	**300 RPM, 5 min*6 cycles, 1 min rest**	-	59	-	41	-	-
Hyd.-ballmilled mixture	**200°C - 24h - 110 bar H_2**	-	34	-	66	-	-

5.3.2 PCT de-/re-hydrogenation studies of THF-adduct $Mg(BH_4)_2$

We next explored whether maintaining the liquid-like phase could serve as an entry point for the hydrogen cycling system between $Mg(BH_4)_2$ and $MgB_{10}H_{10}$. Investigation into the reversibility was carried out using Pressure-Composition-Temperature experiments. Initially, the cycling study started with dehydrogenation process of THF-adduct $Mg(BH_4)_2$ at 200 °C under 4 bar H_2 back pressure for 12 hours; while rehydrogenation of the generated species, $MgB_{10}H_{10}$, lasted for 1 hour under 90 bar H_2 without cooling down the reactor (Figure 5.3). Approximately 2.8 wt. % H_2 was release in the 1st dehydrogenation half cycle after 12 hours while *ca.* 1 wt.% was being absorbed after 1 hour. The 2nd dehydrogenation half cycle recorded a release of ca. 0.8 wt.% with 0.6 wt.% H_2 was observed on the rehydrogenation half cycle. From the obtained PCT data, the dehydrogenation tended to plateau out after 4 hours while the re-hydrogenation curve was continuing to dip indicating the absorption process might proceed further. However, the material was not further dehydrogenated as the *in-situ* XRD showed that solidification results upon prolonged heating which curtails subsequent hydrogen uptake and thus precludes hydrogen cycling.

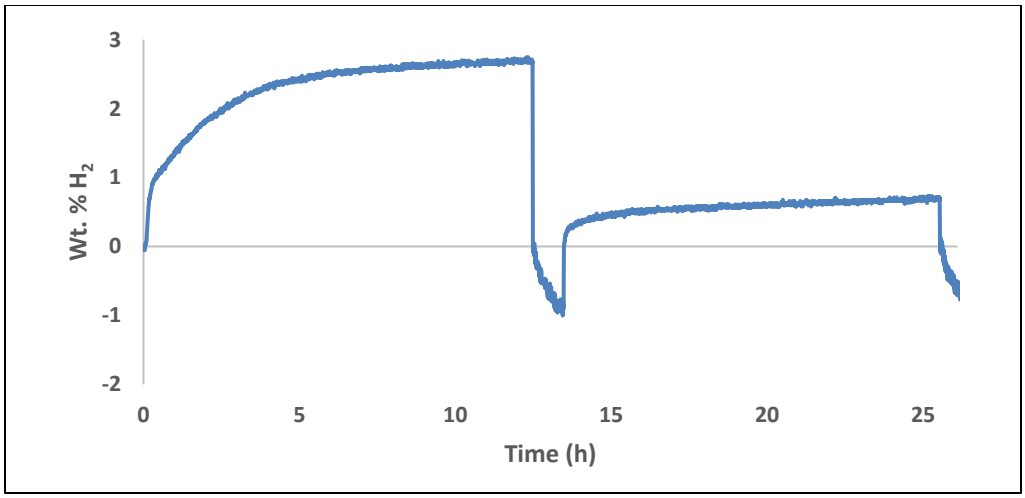

Figure 5.3: PCT cycling of THF-adduct $Mg(BH_4)_2$ at 200 ºC for 2 cycles (dehydrogenation - 12h - 4 bar H_2; rehydrogenation – 1h – 90 bar H_2)

This finding led us to conduct another PCT cycling study under similar reaction conditions but allowing only 3 hours for each de-/ re-hydrogenation half cycle (Figure 5.4). Approximately 2.8 wt.% H_2 was recorded on the 1st dehydrogenation half cycle and ca 1.6 wt.% H_2 was absorbed on the re-hydrogenation half cycle. Interestingly, consistent 1.6 wt.% H_2 was obtained in the 2nd and 3rd cycle.

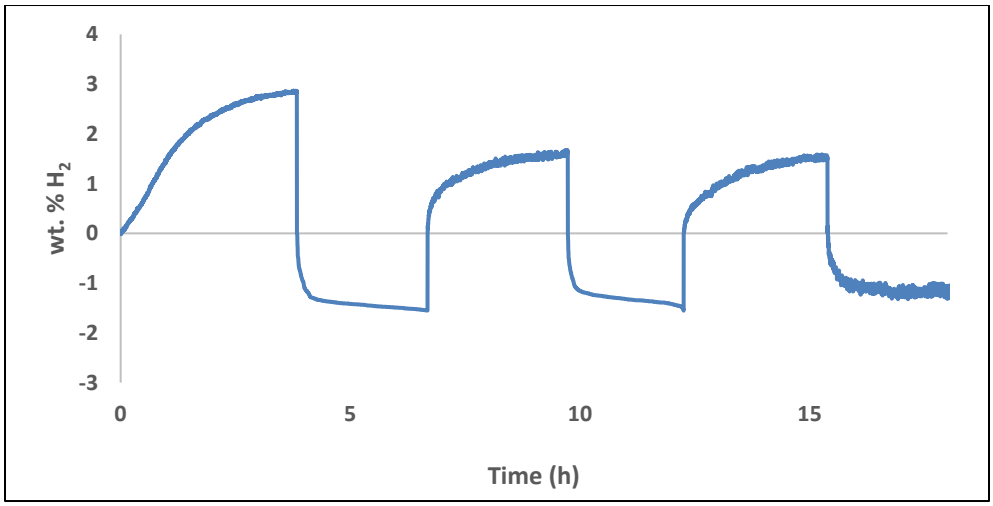

Figure 5.4: PCT cycling of THF-adduct $Mg(BH_4)_2$ at 200 ºC for 3 cycles (dehydrogenation - 3h - 4 bar H_2; re-hydrogenation – 3h – 90 bar H_2)

The products after PCT cycling at various cycles were characterized using solution ^{11}B NMR. Two predominant species were observed, $B_{10}H_{10}^{2-}$ with characteristic chemical shifts 0 & -30 ppm and resonance at the -42 ppm chemical shift for BH_4^- (Figure 5.5). One can note that, the relative intensities of $B_{10}H_{10}^{2-}$ and BH_4^- signals changed, depending on the cycling stage, *i.e.* dehydrogenation or re-hydrogenation. Detailed amounts of $B_{10}H_{10}^{2-}$ and BH_4^- changed were reported in table 5.3. *Ca.* 30% of BH_4^- and $B_{10}H_{10}^{2-}$ was being cycled going from 1, 1.5 to 2 cycles.

Table 5.3: *% borane species in products, based on solution $^{11}B\{^1H\}$ integration, after PCT cycling at various cycles*

# cycles*	Amount/Mol%							NMR solvent	
	Species / δ ^{11}B (ppm)								
	$B(OBu)_4^-$ (3)	$[B_{10}H_{10}]^{2-}$ (0 & -30)	-13 ppm	$B_{12}H_{12}^{2-}$ (-15)	-27 ppm	$B_3H_8^-$ (-31)	BH_4^- (-41)	D_2O	D_2O/THF
1	-	31	-	-	-	-	69		X
1.5	-	70	-	-	-	-	30		X
2		28	3	1	-	-	68		X
1	9	25	-	-	-	-	66	X	
1.5	15	65	-	-	-	-	20	X	
2	8	23	1	1	-	-	65	X	

*cycle = 200 °C – 3h – 4 bar – 3h – 90 bar H_2

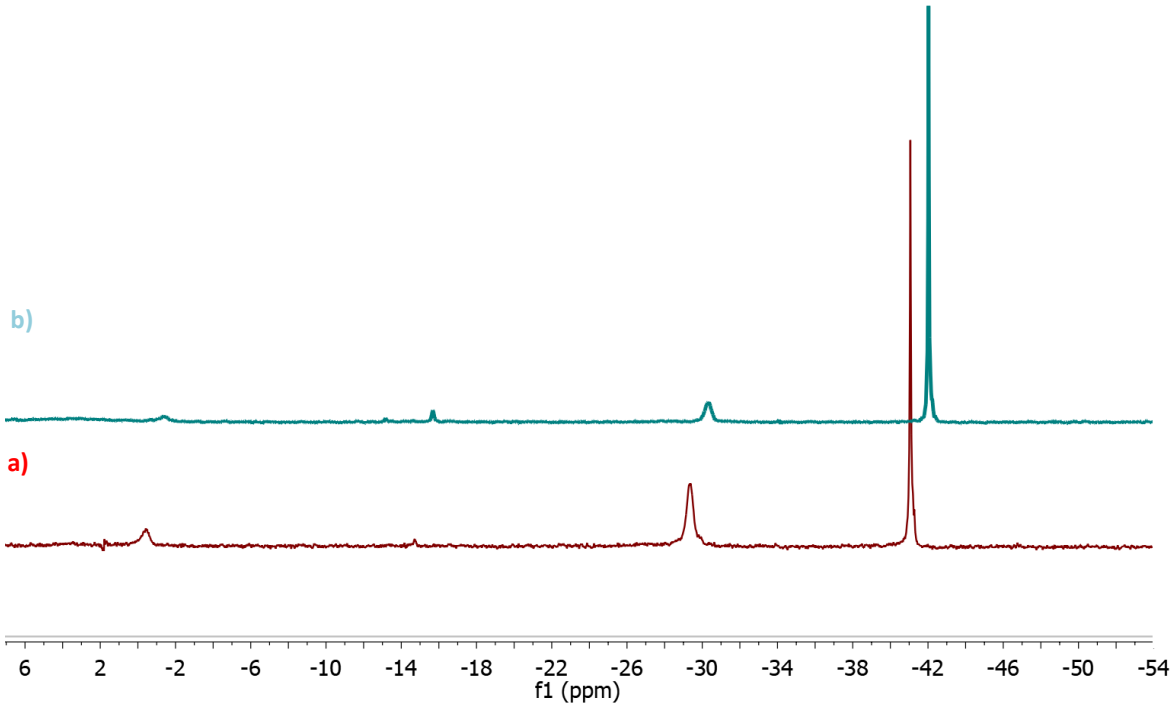

Figure 5.5: Solution ^{11}B NMR in 2D2O/THF of THF-adduct $Mg(BH_4)_2$ after a) 200 ^oC – 3h – 4 bar b) 3 cycles- 200 ^oC – 3h – 4 bar – 3h – 90 bar H_2

Table 5.4 summarizes species observed after various PCT cycles and their corresponding ^1H NMR integration values. THF signals at δ 1.71 and 3.57 were integrated against BH_4^- signal at 0.5 ppm, an estimated of 0.1 equivalent of THF existed in the cycling mixture after 1 and 2 cycles. One should keep in mind, however, that the amount of THF was slightly underestimated due to the overlapping in chemical shifts of BH_4^- and equatorial $B_{10}H_{10}^{2-}$ in the ^1H NMR. Attempt to prepare $Mg(BH_4)_2$ sample with <0.25 THF/Mg ratio followed by cycling study, however, was sporadically successful, owning to the incomplete THF solvation of $Mg(BH_4)_2$, resulted in only partial melting of the starting material.

Table 5.4: *Species present in products, based on solution ^{1}H NMR integration, after PCT cycling at various cycles*

		THF		butoxide				BH_4^-
		^{1}H NMR/ integration value						
	δ (ppm)	1.71	3.57	0.71	1.17	1.34	3.43	-0.25
# cycles	0	0.32	0.31					1
	1	0.10	0.11	0.57	0.37	0.37	0.38	1
	2	0.11	0.12	0.57	0.39	0.41	0.37	1

5.3.3 Kinetic studies of $Mg(BH_4)_2(THF)_{0.25}$ at 150°C, 180°C, 200°C

To better understand the kinetic performance of THF adduct-$Mg(BH_4)_2$ at various temperatures, dehydrogenation trials of $Mg(BH_4)_2(THF)_{0.25}$ was carried out at 150 °C, 180 °C, and 200 °C for 15 hours (Figure 5.6). Significant amounts of H_2 came off within the first 5 hours of dehydrogenation in all three temperatures. At 150°C, the reaction tended to slow down as time progressed. At 180 °C, 3.3 wt.% H_2 were obtained within only 15 hours. The highest amount of H_2 came off, 3.7 wt%, was collected at 200 °C. Subsequent ^{11}B NMR analysis of the products after these short dehydrogenations trials revealed similar results to that of long trials reported earlier, with the selectivity favored the formation of $B_{10}H_{10}^{2-}$.

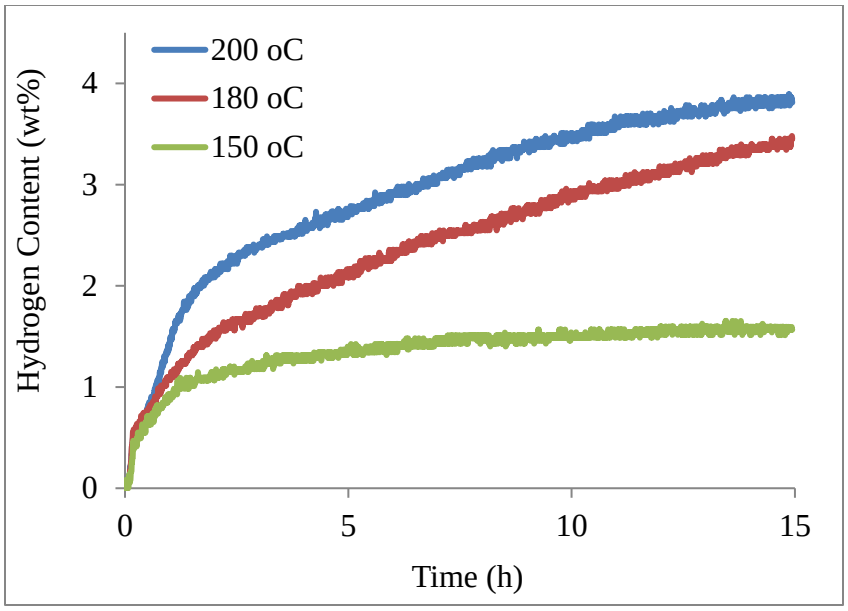

Figure 5.6: PCT dehydrogenation profile of $Mg(BH_4)_2(THF)_{0.25}$ measured at 150 °C, 180 °C, and 200 °C

5.3.4 Isothermal kinetic analysis of $Mg(BH_4)_2$ – $MgB_{10}H_{10}$ cycling system

We have developed critical strategies for cycling of H_2 between $MgB_{10}H_{10}$ and $Mg(BH_4)_2$ at moderate temperatures and pressures. Most important is the maintenance of an amorphous or liquid-like phase throughout the cycling between $MgB_{10}H_{10}$ and $Mg(BH_4)_2$. We also investigated the rate of each dehydrogenation and re-hydrogenation reaction (Appendix, Figure S2-7). A linear relationship is observed for the plots wt.% vs. time for 1st and 2nd re-hydrogenation reaction. Thus, the re-hydrogenation reactions follow 0th order or pseudo-0th order kinetics. The 2nd and 3rd dehydrogenation reactions follow similar reaction order, pseudo-0th order kinetics.

5.4 Conclusions

We have demonstrated for the first time the cycling of H_2 release and uptake between BH_4^- and $B_{10}H_{10}^{2-}$. The reversibility can be maintained in the melt. Prolonged

heating beyond 10 hours at 180 ^{o}C or cooling to room temperature curtails reversibility. We anticipate greater H_2 cycling capacity will be achieved upon extension of the compositional limits of the molten state. We have not solved the practical problem; however, we have achieved the reversible interconversion of BH_4^- and $B_{10}H_{10}^{2-}$ under moderate conditions was previously believed impossible due to the high kinetic stability of the *closo*-$B_{10}H_{10}^{2-}$ cluster.

CHAPTER 6: SYNTHESIS AND ATTEMPTED HYDROGENATION of $MgB_{12}H_{12}(THF)_3$

6.1 Introduction

A wide variety of hydrogen storage materials have been investigated in the search for a viable candidate with the potential to reversibly store hydrogen. Due to the combined high volumetric and gravimetric hydrogen densities, light metal complex hydrides have been widely studied for application in solid-state hydrogen storage. Among them, magnesium borohydride, $Mg(BH_4)_2$, with a high hydrogen capacity (14.9 wt.% H_2), is currently one of the most-discussed complex hydrides. The dehydrogenation of $Mg(BH_4)_2$ shows a stepwise decomposition results in the formation of a wide range of potential borane B_xH_y products.[5,53,81] In previous work, cycling between $Mg(BH_4)_2$ and range of borane intermediates varying from $Mg(B_3H_8)_2$ (2.5 wt.% H_2) to MgB_2 (11 wt.% H_2) were reported, however, the rate for H_2 release and uptake are extremely slow, requiring high temperature, high pressure, and long reaction times.[82,83,127]

The addition of Lewis bases has been shown to be an effective mean of improving kinetics of the dehydrogenation of $Mg(BH_4)_2$ to $MgB_{10}H_{10}$[120], hydrogenation of $Mg(B_3H_8)_2$ to $Mg(BH_4)_2$[87], and hydrogenation of MgB_2 to $Mg(BH_4)_2$.[129] In the absence of Lewis bases, the dehydrogenation of $Mg(BH_4)_2$ to $Mg(B_3H_8)_2$ takes over 5 weeks at 200 ^oC, which in turn requires 120 bar of H_2 and heating to 250 ^oC for 48 hours to cycle back to $Mg(BH_4)_2$.[83] However, quantitative yield of $Mg(BH_4)_2$ was obtained upon re-hydrogenation of $Mg(B_3H_8)_2(THF)_2$ after only 2 hours at 200 ^oC under 50 bar H_2.[87] Recent studies of THF complexed $Mg(BH_4)_2$ demonstrated the kinetics enhancement, shown to enable the rapid

release of H_2 at <200 ^oC to yield $MgB_{10}H_{10}$ as the selective product.[87] Moreover, interaction of MgB_2 and THF, promoted by mechano-chemical process, allows the transformation of MgB_2 to $Mg(BH_4)_2$ to be accomplished at 300 ^oC under 700 bar H_2,[129] in relative to 400 ^oC and 900 bar of H_2 for the bulk MgB_2.[127] Of further note is the successful cycling of hydrogen release and uptake between $Mg(BH_4)_2$ and $MgB_{10}H_{10}$ upon maintaining the melt, aided by THF, throughout the entire course of the reversible reaction.[128]

Recent theoretical and experimental results show that an intermediate phase, $MgB_{12}H_{12}$, forms during hydrogen desorption from $Mg(BH_4)_2$ prior to the formation of final products.[85,114,115] The $MgB_{12}H_{12}$ intermediate, having strong B-B bonds in a stable, *closo* icosahedral boron cage, has been widely regarded as an obstacle for the re-hydrogenation to $Mg(BH_4)_2$.[79] In spite of the important role of this intermediate, its properties such as stability and reactivity are still unknown and its role in the $Mg(BH_4)_2$ reaction process has not yet been fully understood, partly due to the synthesis challenge of $MgB_{12}H_{12}$.

Salts of $B_{12}H_{12}^{2-}$ are generally synthesized using wet chemistry metathesis reactions followed by the thermolysis of their hydratates.[123-125] Attempt to dehydrate $Mg(H_2O)_6B_{12}H_{12}\cdot 6H_2O$, however, result in the formation of polyhydroxylated complex, $Mg(H_2O)_{(3-x)}(\mu\text{-}OH)_xB_{12}H_{(12-x)}$.[130] Attempt to prepare a THF solvated complex of $MgB_{12}H_{12}$ v*ia* the reaction between $B_{10}H_{14}$ and $Mg(BH_4)_2$ in THF was also hindered by difficulties in the purification of the final product.[130] Further attempts have been made to synthesize solvent-free $MgB_{12}H_{12}$ employing $Mg(BH_4)_2$/carbon nanocomposite ball-milling in B_2H_6/H_2 atmosphere[131] and sintering $Mg(BH_4)_2$ with $B_{10}H_{14}$.[132] However, no further attempt to re-hydrogenate the synthesized $MgB_{12}H_{12}$ back to $Mg(BH_4)_2$ was

reported, owning to the presumed high kinetics barrier and unfavorable thermodynamic toward hydrogenation of $MgB_{12}H_{12}$.

The finding of kinetics enhancement of solvent-coordinated borane complexes motivates us to investigate the reversibility of THF-adduct $MgB_{12}H_{12}$, given the successful synthesis of the thus-synthesized species. In this work, we employed the solid-gas reaction of $Mg(B_3H_8)_2(THF)_3$ with B_2H_6/ H_2 gas mixture, a synthesis that yielded THF-solvated $MgB_{12}H_{12}$ quantitatively. Alternative synthesis route to *closo*-borane clusters, yielding 4:1 molar ratio $B_{12}H_{12}^{2-}$ to $B_{10}H_{10}^{2-}$ involves the pyrolysis of $Mg(B_3H_8)_2(THF)_2$. Preliminary re-hydrogenation study of the synthesized THF-adduct $MgB_{12}H_{12}$ was investigated using Pressure-Composition-Temperature (PCT) followed by NMR analysis of the reaction products. Structures of THF-adduct $MgB_{12}H_{12}$, derived from NMR, IR, and X-Ray Diffraction, was also proposed.

6.2 Experimental

All sample preparations and handling were conducted in a nitrogen glovebox or on a Schlenk line. Solvents were purified by a SPS system or distilled over a drying agent if required.

6.2.1 Preparation of THF-adduct $Mg(B_3H_8)_3$

Similar synthesis procedure to the aforementioned $Mg(B_3H_8)_2(THF)_2$ in chapter 2 was carried out with minor modification. The white precipitate was dried overnight under vacuum without the applied heat.

6.2.2 Synthesis of $Mg(BH_4)_2$

$Mg(BH_4)_2$ was prepared according to an established synthesis in the literature.[12] Under N_2 atmosphere, di-*n*-butyl-magnesium (50 mL, Sigma Aldrich, 1M solution in heptane) was slowly added dropwise to a solution of borane-dimethyl sulfide (90 mL, Acros Organics, 2 M in toluene). The solution was allowed to stir for five hours after which the mixture was transferred through a medium frit filter and washed with toluene. The resulting white powder, magnesium borohydride dimethyl sulfide complex, $Mg(BH_4)_2 \bullet \frac{1}{2}S(CH_3)_2$ was dried *in vacuo* at room temperature overnight after which afforded solvent free magnesium borohydride, $Mg(BH_4)_2$

6.2.3 Synthesis of THF solvated-$MgB_{12}H_{12}$

0.2g ballmilled $Mg(BH_4)_2$ or THF-solvated $Mg(B_3H_8)_2$ (400 RPM, 4 cycles, 15 minutes/ cycle, 1 minute break, 30:1 ball to powder ratio) was loaded into an autoclave (Parr Instrument) followed by direct filling of 4% B_2H_6/ H_2 (BOC GASES) to desired pressure. Reaction vessel temperature was controlled *via* heating mantle. The obtained product was either dried *in vacuo* at 50 ^oC to remove loose bound THF or remained as synthesized prior to further characterization.

6.2.4 Pyrolysis of THF-solvated $Mg(B_3H_8)_3$

0.2g $Mg(B_3H_8)_2(THF)_3$ was loaded into a bomb flask and heated up to 180 ^oC for 7 hours in an oil bath. The obtained white products were characterized using NMR.

6.2.5 Ballmilling of obtained $MgB_{12}H_{12}$ and MgH_2

Obtained mixture from $Mg(B_3H_8)_2(THF)_3$ pyrolysis was ballmilled with 5 molar equivalent of MgH_2 (to $MgB_{12}H_{12}$) at 300 RPM for 30 minutes.

6.2.6 Isothermal re-hydrogenation

Re-hydrogenation experiments were carried out on a Suzuki Shokan PCT-2SDWIN Sievert type apparatus. Precise temperature was achieved using customized heating mantle sleeves. Reactors with fixed volumes were initially evacuated prior to hydrogen pressurization.

6.2.7 NMR characterization

^{11}B NMR spectroscopic experiments were performed on a Varian Unity Innova 500 MHz spectrometer with ^{11}B chemical shifts referenced to $BF_3 \cdot OEt2$ (δ =0 ppm) at 25 ^oC. Spectra were recorded both with and without decoupling. D_2O and 2:1 volume ratio of D_2O/THF were used as NMR solvents due to the highest dissolution rate and resolution of closed-cage structure boranes.

6.2.8 Infrared Vibrational Spectroscopy

In recent works about borohydrides, the KBr technique has been avoided because BH_4^- can exchange with Br^-, due to their similar ionic radii.[97] In the present case, the radius of $B_3H_8^-$ is much larger and should not give this problem. To exclude spurious effects, however, we performed infrared spectroscopy measurements in two different configurations: in transmission geometry using a pure pellet (without KBr or other salts)

or by means of an Attenuated Total Reflectance accessory (ATR) on the hydride powders. The first method gives saturated bands in the B-H stretching region but provides well-defined spectra below 1700 cm^{-1}, where the intensity of bands is much lower. On the other hand, the second method is well-suited in the B-H stretching region. It must be noted, however, that ATR displays the same features obtained in the case of the pure pellet below 1700 cm^{-1}, but with a lower quality of the measurement. Therefore, in the following, we report data obtained by ATR between 1800 and 3300 cm^{-1} and by transmission measurements on the pure pellet in the frequency range 600-1700 cm^{-1}. In this framework, infrared spectroscopy measurements below 1800 cm^{-1} were performed at room temperature by means of an Agilent Cary 660 spectrometer equipped with a ceramic source, a MCT detector, and a KBr beam splitter. A small amount of the sample was pressed in a dye to obtain a self-standing pellet. The pellet was placed in a vacuum tight cell during measurements. Above 1800 cm^{-1}, data were collected by means of a Bruker Alpha spectrometer equipped with an ATR accessory. Sample handling was performed in a Ar glovebox to avoid contaminations.[98,99] All absorption spectra were collected with a spectral resolution of 2 cm^{-1}.

6.2.9 Density Functional Theory Calculation

Ab-initio and DFT calculations were performed starting from those geometries by means of the Firefly package.[101] In all cases, we used the 6-31G** basis set. The wxMacMolPlt software was used to visualize the molecular geometries and vibrations.[102] After calculation of the infrared active vibrations, the IR spectrum was simulated by

summing Lorentzian curves centered at each calculated IR vibration frequency with a fixed 10 cm^{-1} peak width.

6.3 Results and Discussion

6.3.1 Characterization of the synthesized THF-adduct $MgB_{12}H_{12}$

Phase 1 – $MgB_{12}H_{12}(THF)_{1.5}$

The THF-adduct of $MgB_{12}H_{12}$ was prepared by the reaction of bulk $Mg(B_3H_8)_2(THF)_3$ in 20 bar of 4% B_2H_6/ H_2 gas mixture for 6 hours at 125 ^oC. Upon drying in vacuum at 50 ^oC, the obtained sample was investigated by solution ^{11}B NMR using D_2O as the solvent (Figure 6.1). In figure 6.1, the prominent doublet at -15 ppm indicated the formation of $MgB_{12}H_{12}$. Trace amount of $Mg(BH_4)_2$ (quintet, δ -42 ppm), $MgB_{10}H_{10}$ (doublet, δ -30 ppm and doublet, δ -1 ppm), and unknown borane at δ -21 ppm (doublet) can also be observed.

The ^1H NMR, taken in D_2O, of the product contained a large characteristic signal of $B_{12}H_{12}^{2-}$ at 1.1 ppm (Figure 6.2). Two prominent signals of THF, 1.75 and 3.6 ppm, were also observed besides signal for D_2O solvent at 4.7 ppm. On the basis of ^1H NMR integration, the complex had the empirical formula of $MgB_{12}H_{12}(THF)_{1.5}$.

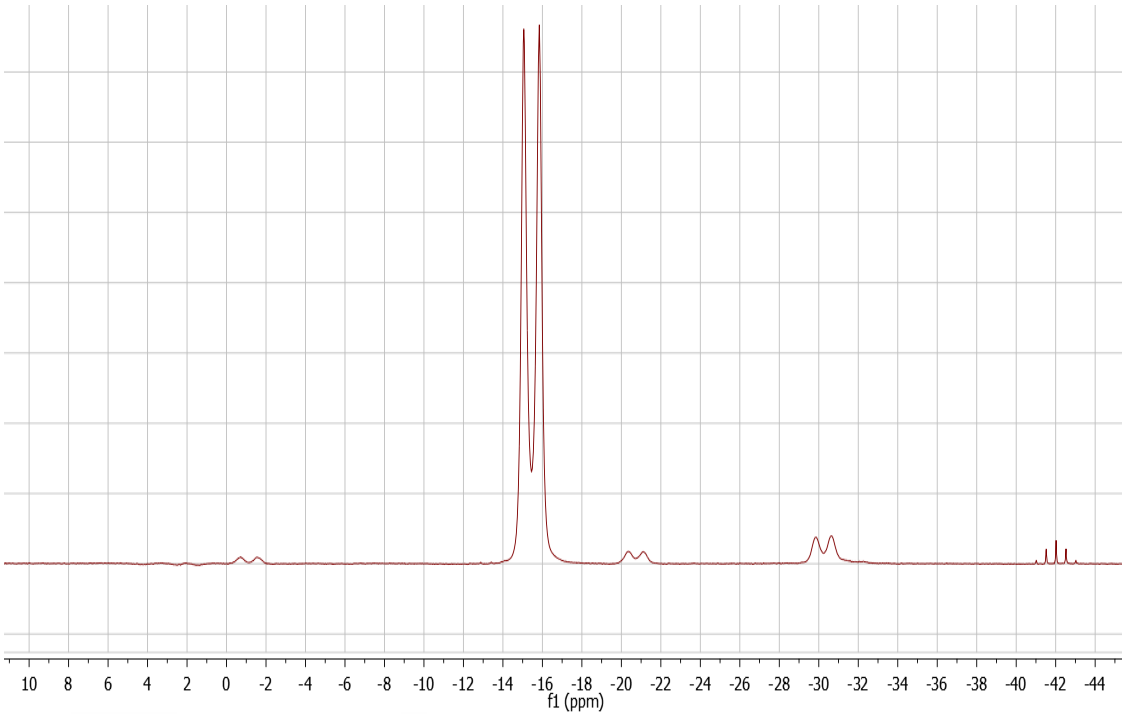

Figure 6.1: Solution ^{11}B NMR in D_2O of $Mg(B_3H_8)_2(THF)_3$ after heating at 125 ^oC under 4% B_2H_6/ H_2 for 6 hours

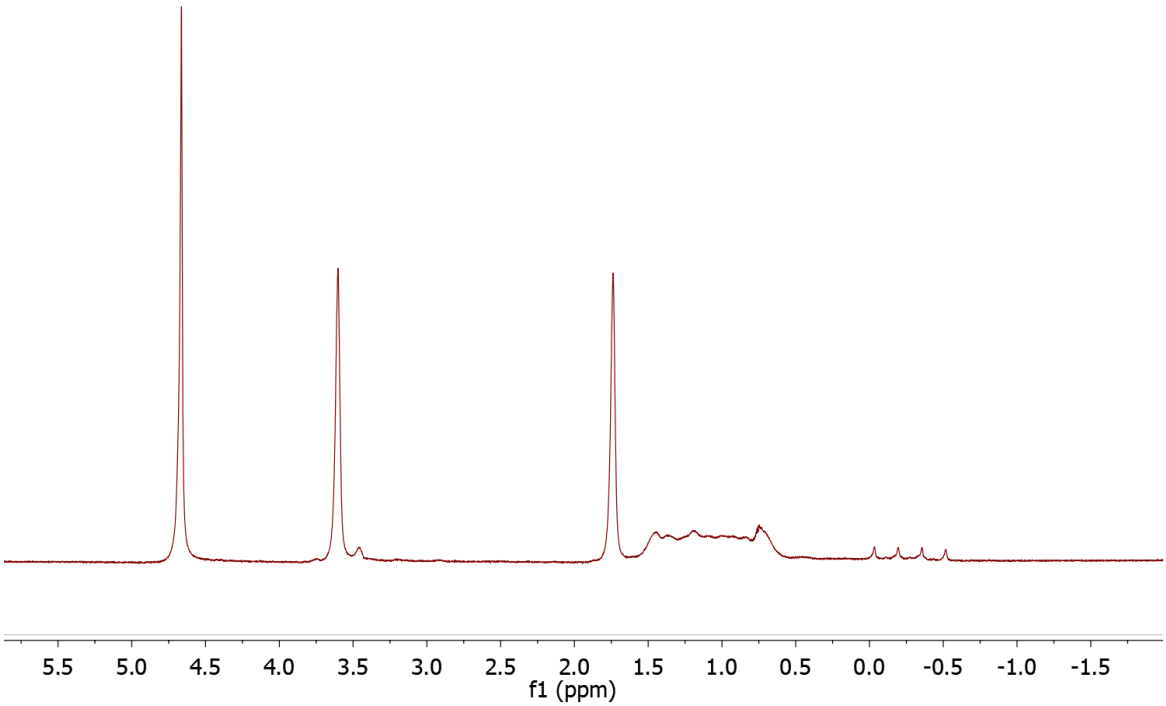

Figure 6.2: ^1H NMR in D_2O of $Mg(B_3H_8)_2(THF)_3$ after heating at 125 ^oC under 4% B_2H_6/ H_2 for 6 hours

To gain better insight into the coordination mode of THF with $MgB_{12}H_{12}$ complex, we measured the IR spectrum of $MgB_{12}H_{12}(THF)_{1.5}$ in the far and mid-infrared region from 50 to 3500 cm^{-1}. The B-H stretching, 2450 cm^{-1}, is a single peak, no splitting or additional peak due to the coordination of $B_{12}H_{12}^{2-}$ to Mg^{2+} was observed. Therefore, the $B_{12}H_{12}^{2-}$ retains its high symmetry, icosahedral (Figure 6.3). The single B-H stretch at 2450 cm^{-1} can be further interpreted by group theory, corresponds to T_{1u} symmetry species. The $MgB_{12}H_{12}(THF)_{1.5}$ has a similar IR spectrum in the B-H stretching region to of sample without THF (Figure S8).[133]

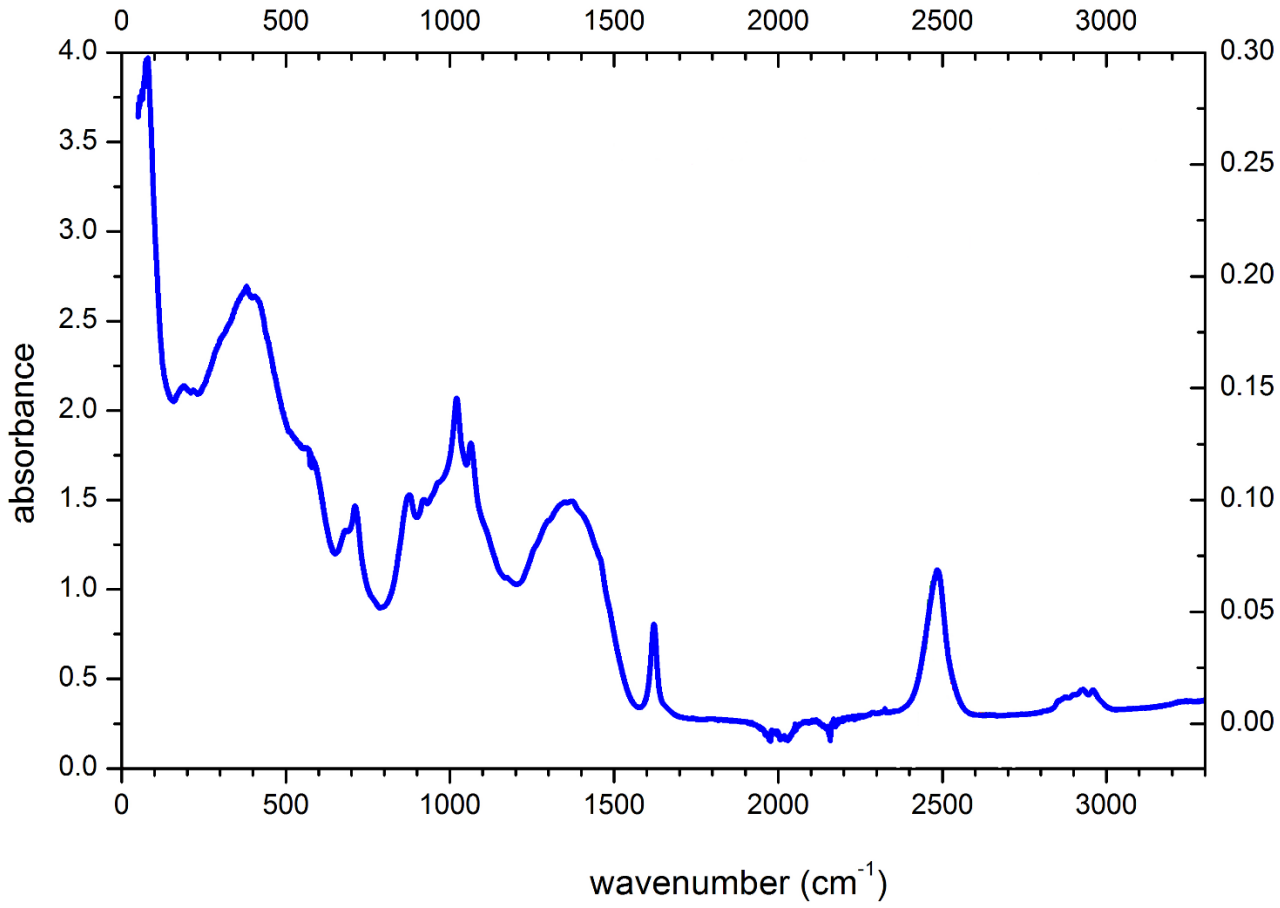

Figure 6.3: Measured IR absorption of $MgB_{12}H_{12}(THF)_{1.5}$

Phase 2 – $MgB_{12}H_{12}(THF)_3$

Following the same synthesis procedure of the aforementioned $MgB_{12}H_{12}(THF)_{1.5}$ with minor modification in the final drying step, a crystalline phase of THF-adduct $MgB_{12}H_{12}$ was obtained. Collaborative studies were carried out with Dr. Mark Bowden at Pacific Northwest National Laboratories in which Powder X-Ray Diffraction was employed to obtain the crystal structure of the complex. To our surprise, the suggested crystal structure gave rise to a molecule with empirical formula of $MgB_{12}H_{12}(THF)_3$ where Mg^{2+} binds to one $B_{12}H_{12}^{2-}$ and three THF molecules (Figure 6.4).

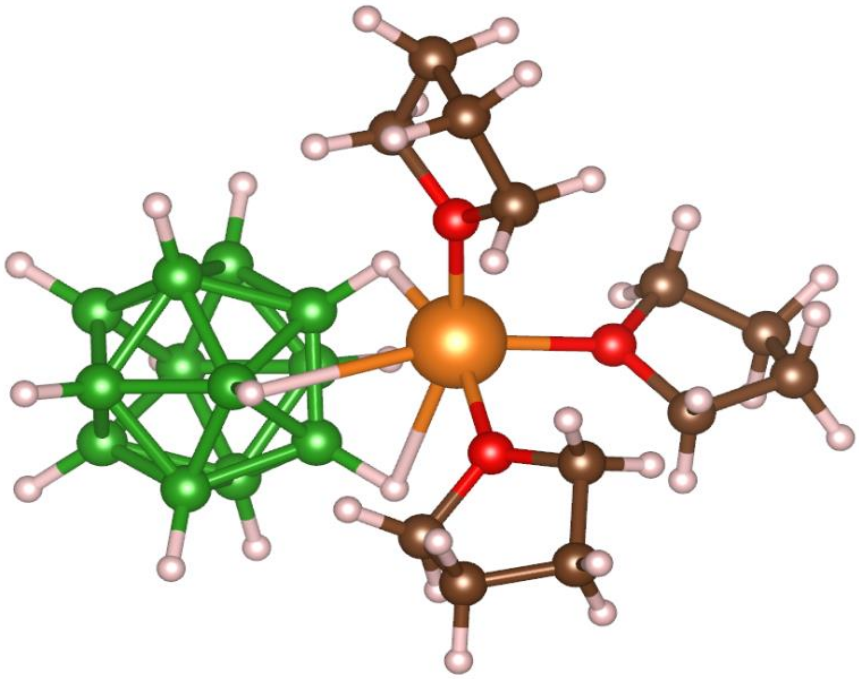

Figure 6.4: Crystal structure of $MgB_{12}H_{12}(THF)_3$

We next optimized geometries and calculated IR absorption spectra of isolated $B_{12}H_{12}^{2-}$ anion $MgB_{12}H_{12}(THF)_3$ (Figure S9, 10). The calculated IR spectrum of isolated $B_{12}H_{12}^{2-}$ show the presence of single B-H stretch at 2500 cm^{-1}, closely related to what was

observed in the literature (Figure S8).[133] The calculated IR spectrum of $MgB_{12}H_{12}(THF)_3$, however, shows multiple B-H stretches in the 2300 – 2500 cm^{-1} region. Utilizing group theory, stretching mode analysis is performed on the $MgB_{12}H_{12}(THF)_3$ molecule and the results are report in Table 6.1. With the THF coordination, the $MgB_{12}H_{12}(THF)_3$ is suggested to possess C_{3v}, which gives rise to ten symmetry species, $7A_1$, A_2, and 2E after irreducible representations. From the C_{3v} character table (Table S4, Appendix), one can note that besides A_2 symmetry species, $7A_1$ and 2E have basis on z and (x,y) axis; thus, these 9 symmetry species are IR active. The obtained results from group theory agree with the observations of multiple overlapping B-H stretches in the calculated IR spectrum of $MgB_{12}H_{12}(THF)_3$

Table 6.1: *Stretching mode analysis on $MgB_{12}H_{12}(THF)_3$*

C_{3v}	E	$2C_3$	$3\sigma_v$
γ_{B-H}	12	6	6

6.3.2 Hydrogenation studies of THF-adduct $MgB_{12}H_{12}$

6.3.2.1 Pyrolysis of THF-solvated $Mg(B_3H_8)_3$

Due to the toxic nature utilizing B_2H_6 to obtained $MgB_{12}H_{12}(THF)_3$, an alternative $MgB_{12}H_{12}$ synthesis route, pyrolysis of THF-adduct $Mg(B_3H_8)_2$, was developed. In a bomb flask, $Mg(B_3H_8)_2(THF)_3$ was loaded followed by ramping up to 180 ^oC and held for 7 hours, yielded a 4:1 molar ratio mixture of $MgB_{12}H_{12}$ and $MgB_{10}H_{10}$ (Eqn. 6.1).

$$^{11}/_{3}Mg(B_3H_8)_2(THF)_3 \xrightarrow[7h,\ 180^\circ C]{1\ atm\ N_2} MgB_{12}H_{12}(THF)_x + MgB_{10}H_{10}(THF)_{11-x} + {}^{5}/_{3}\ MgH_2 + {}^{50}/_{3}\ H_2 \qquad \textbf{(6.1)}$$

We next explored whether a mixture of THF-adduct $MgB_{12}H_{12}$ and MgH_2 could serve as an entry point for the hydrogen cycling system between $MgB_{12}B_{12}$ and $Mg(BH_4)_2$. Accordingly, a mixture of 1:5 molar ratio of $MgB_{12}H_{12}$ and activated MgH_2 was ballmilled for 30 minutes followed by solution ^{11}B and ^{1}H NMR analysis. The solution ^{11}B NMR of the ballmilled mixture in D_2O/THF indicated the presence of 4:1 molar ratio of $MgB_{12}H_{12}$ (δ -15 ppm) to $MgB_{10}H_{10}$ (δ -30, -1 ppm) (Figure 6.5). The solution ^{1}H NMR in D_2O indicated the prominent presence of THF (δ -1.75, 3.6 ppm) and $B_{12}H_{12}^{2-}$ (δ 1 ppm) (Figure 6.6). Broad signal of equatorial $B_{10}H_{10}^{2-}$ was also observed at 0 ppm.

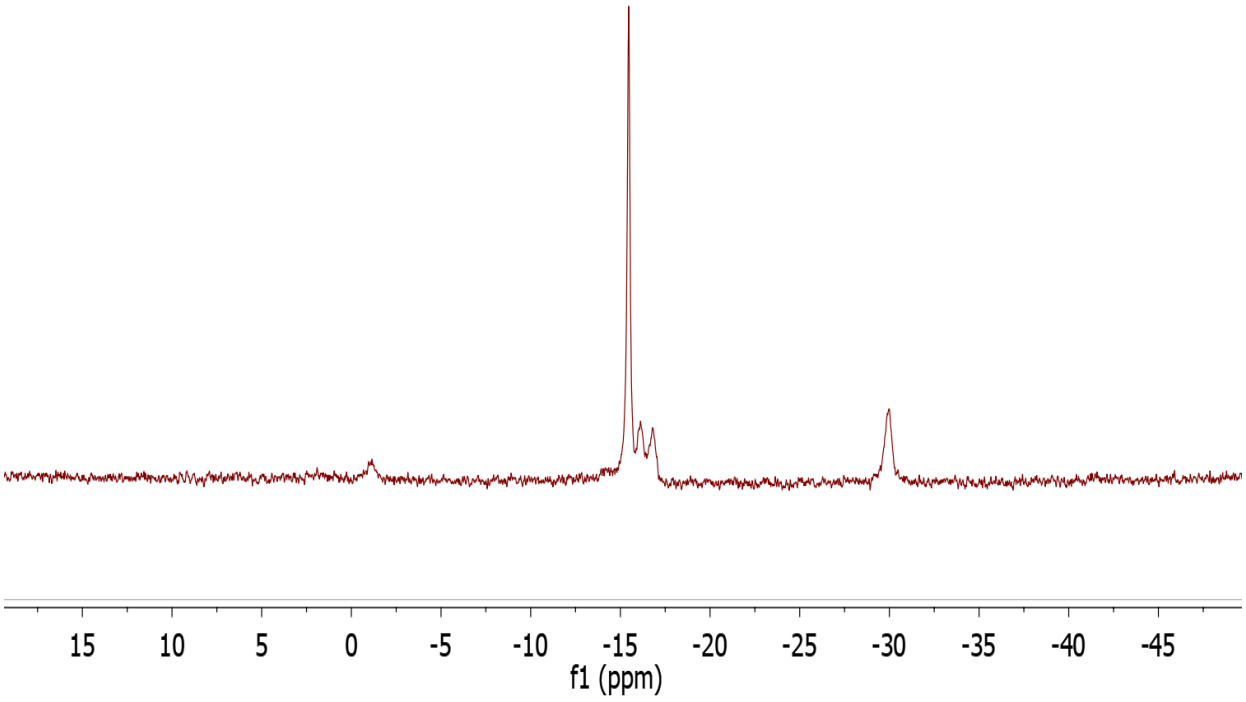

Figure 6.5: Solution $^{11}B\{^{1}H\}$ NMR in D_2O/THF of ballmilled mixture obtained $MgB_{12}H_{12}$ and activated MgH_2

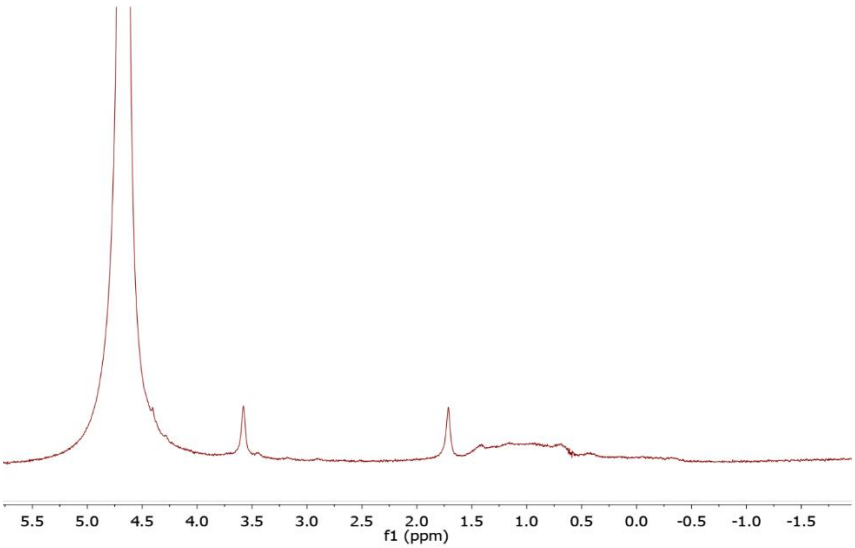

Figure 6.6: Solution ^{1}H NMR in D_2O of ballmilled mixture obtained $MgB_{12}H_{12}$ and activated MgH_2

The ball-milled mixture of $MgB_{12}H_{12}(THF)_x$ and MgH_2 was heated to 200 ^{o}C under 90 bar H_2 for 10 hours. The solution $^{11}B\{^{1}H\}$ NMR in D_2O/THF of the ball-milled mixture after hydrogenation showed no change in either $B_{12}H_{12}^{2-}$ or $B_{10}H_{10}^{2-}$ and no BH_4^- (δ -41 ppm) was observed (Figure 6.7)

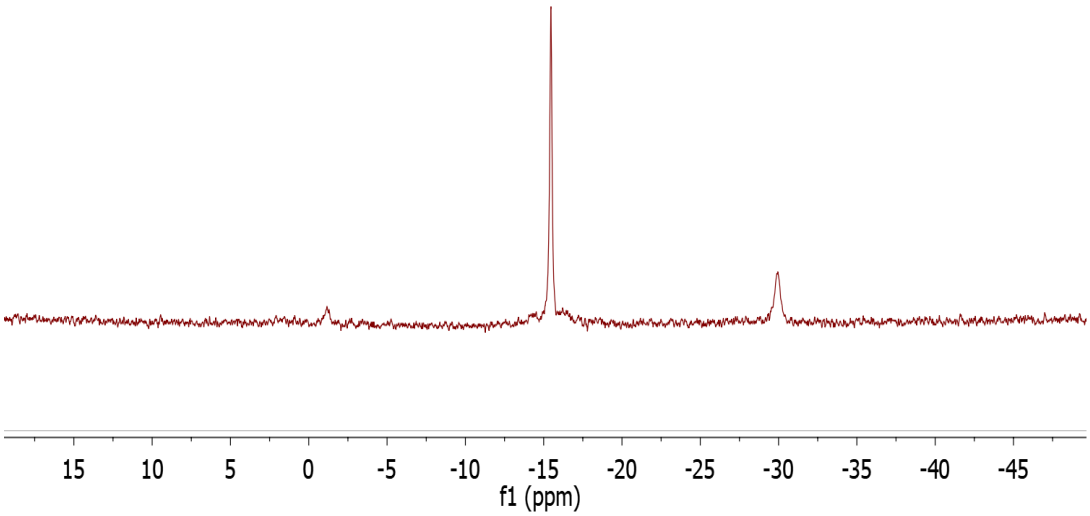

Figure 6.7: Solution $^{11}B\{^{1}H\}$ NMR in D_2O/THF of ballmilled mixture obtained $MgB_{12}H_{12}$ and activated MgH_2 after 10 hours heating under 90 bar H_2

The solution ^{1}H NMR in D_2O of the ball-milled mixture after hydrogenation indicated the THF (δ -1.75, 3.6 ppm) remained through the hydrogenation, $B_{12}H_{12}^{2-}$ (δ 1 ppm) and small amount of butoxide (δ 0.75, 1.15, 1.32, 3.4 ppm) was also formed. No BH_4^- (δ -1 ppm) was observed (Figure 6.8).

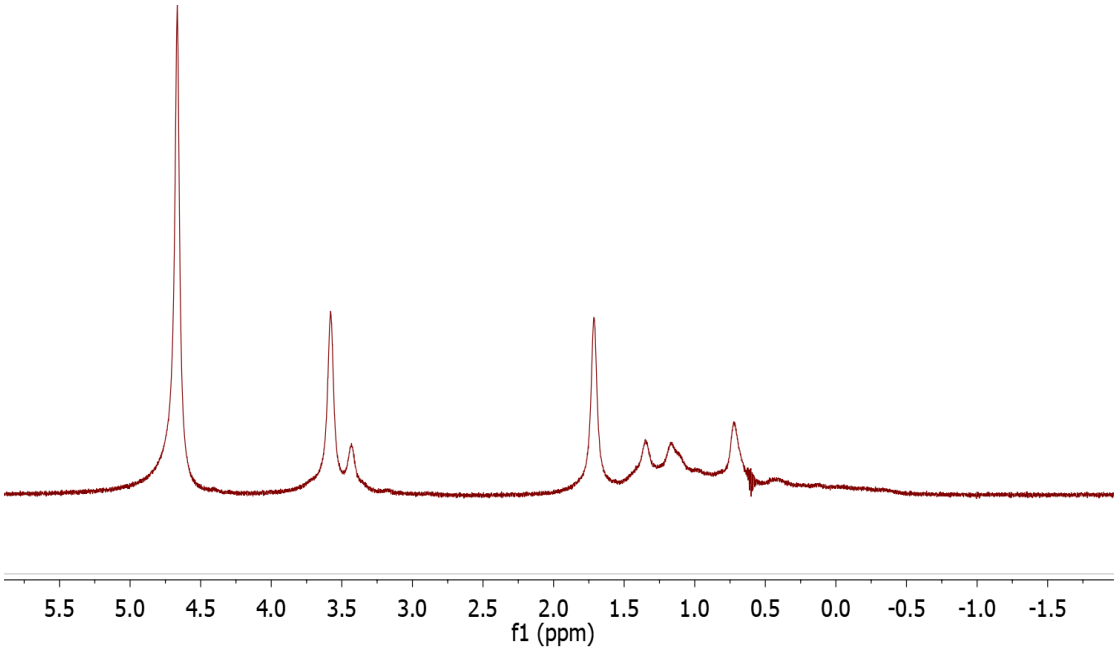

Figure 6.8: Solution ^{1}H NMR in D_2O of ballmilled mixture obtained $MgB_{12}H_{12}$ and activated MgH_2 after 10 hours heating under 90 bar H_2

6.4 Conclusion

We have demonstrated the successful synthesis of THF-adduct $MgB_{12}H_{12}$. We investigated whether the presence of the THF adduct could possibly help overcome the high thermodynamic stability of unsolvated $MgB_{12}H_{12}$ and enable its hydrogenation $Mg(BH_4)_2(THF)_x$. Quantitative yield of THF-adduct $MgB_{12}H_{12}$ was achieved via a gas-solid reaction between $Mg(B_3H_8)_2$ and B_2H_6. The product was readily soluble in D_2O with a chemical shift of -15 ppm in solution ^{11}B NMR. Structure elucidation of the synthesized

product using different analysis proposed the presence of two different phases. NMR and IR analysis of amorphous $MgB_{12}H_{12}(THF)_{1.5}$, indicated that no coordination of THF to Mg. Whereas Powder X-Ray Diffraction of the crystalline phase, $MgB_{12}H_{12}(THF)_3$ shows the presence of direct THF-Mg coordination.

Alternative route to the synthesis of THF-solvated $MgB_{12}H_{12}$ was developed through the pyrolysis of $Mg(B_3H_8)_2(THF)_3$, yielded a 4:1 molar ratio mixture of $B_{12}H_{12}^{2-}$ and $B_{10}H_{10}^{2-}$. Attempted hydrogenation of the 4:1 ball-milled mixture of $MgB_{12}H_{12}/MgB_{10}H_{10}$ and activated MgH_2 back to $Mg(BH_4)_2$ at 200 ^oC under 90 bar H_2 for 10 hours proved unsuccessful. ^{11}B NMR analysis showed no change in the relative amounts of $B_{12}H_{12}^{2-}$ and $B_{10}H_{10}^{2-}$ as well as no formation BH_4^-. It is noted that THF remained throughout the hydrogenation, indicated by ^1H NMR analysis.

CHAPTER 7: CONCLUSIONS AND FUTURE DIRECTIONS

7.1 Conclusions

In the search for advanced hydrogen storage materials, magnesium borohydride has been attacked great interest as a potential candidates. Slow rates of hydrogen sorption and the thermodynamic of the major dehydrogenation product, $MgB_{12}H_{12}$, remain as critical challenges.

While nearly all-previous studies have focused on the solid-state decomposition pathway, this body of work investigated the effect of additive, *i.e.* THF, on the reversibility of $Mg(BH_4)_2$ at moderate conditions. The ^{11}B and ^{1}H spectra revealed the selective formation of $MgB_{10}H_{10}$ at temperature < 200 ^{o}C upon dehydrogenation of THF-solvated $Mg(BH_4)_2$, circumvented the formation of the highly stable $MgB_{12}H_{12}$ species. We have demonstrated for the first time the cycling of H_2 release and uptake between BH_4^- and $B_{10}H_{10}^{2-}$. The reversibility can be maintained in the melt. Prolonged heating beyond 10 hours at 180 ^{o}C or cooling to room temperature curtails reversibility. Moreover, cycling kinetics, 3 hours each dehydrogenation/ hydrogenation half cycle, are within the realm of practicality for hydrogen storage material development.

Exploration into molecular structures of different THF adducts, *e.g.* $Mg(B_3H_8)_2$, $MgB_{12}H_{12}$ utilizing different analytical techniques, NMR, IR, Powder X-Ray Diffraction and computational modelling was demonstrated. Different coordination modes of THF to the magnesium boranes were proposed, however, their roles in the sorption cycle between $Mg(BH_4)_2$ and $Mg(B_3H_8)_2$, $MgB_{10}H_{10}$, and $MgB_{12}H_{12}$ pique for further studies.

The detailed synthesis utilizing $Mg(B_3H_8)_2(THF)_3$ and B_2H_6/H_2, afforded quantitative yield of THF-solvated $MgB_{12}H_{12}$, was thoroughly documented. Alternative synthesis route, pyrolysis of $Mg(B_3H_8)_2(THF)_3$, resulted in a 4:1 molar ratio mixture of $B_{12}H_{12}$ and $MgB_{10}H_{10}$, was developed. The preliminary reversibility screening of the material mixture was demonstrated. Despite the aided role of THF in $Mg(BH_4)_2$/ $MgB_{10}H_{10}$ cycling system, no reversibility of $MgB_{12}H_{12}$ back to $Mg(BH_4)_2$ was observed at the experimental conditions.

7.2 Future work

The full cycling potential between $Mg(BH_4)_2$ and $MgB_{10}H_{10}$ is 8.1 wt.%, however, only consistent cycling of 1.5 wt.% H_2 was exhibited, owning to the crystallization upon prolong heating. We anticipate greater H_2 cycling capacity will be achieved upon extension of the compositional limits of the molten state. Furthermore, for practical usage in the Proton-Exchange-Membrane (PEM) fuel cell, the purity of the release H_2 should be further examined.

While the destabilization of magnesium boranes using additives has been demonstrated, currently no studies were found in the literature focus on using solvent as an additive. Further investigation on adduct coordination number and stabilities for a series of ethers would prove insightful in the understanding of this system.

Appendix A:

Table S1: *Energies of different optimized geometric structures of $Mg(B_3H_8)_2(THF)_2$ (in Hartree) at various theory levels.*

	η1	**η2**
MP2	-821.2082062	-821.2220657
B97-D	-823.3737212	-823.3898445
B3LYP	-823.8287362	-823.8345862

Table S2: *Main bond length of $Mg(B_3H_8)_2(THF)_2$ at different levels of theory and comparison with the experimental values reported for $Mg(B_3H_8)_2(Et_2O)_2$, $Mg(B_3H_8)_2(Me_2O)_2$, and $Cp_2Mg(THF)$ obtained by means of XRD measurements.*[89]

	This work			**Experimental values[89]**		
	η2 - MP2	η2 - B3LYP	η2 - B97-D	$Mg(B_3H_8)_2(Et_2O)_2$	$Mg(B_3H_8)_2(Me_2O)_2$	$Cp_2Mg(THF)$
B1-H4	1.19-1.22	1.2	1.21	1.12-1.17	1.08-1.14	
B1-H10	1.24-1.25	1.25-1.26	1.26-1.27	1.02	1.10-1.17	
B2-H10	1.41-1.44	1.42-1.45	1.45-1.49	1.43	1.38-1.45	
B2-B6	1.19	1.2	1.21	1.02	1.11-1.17	
B1-B2	1.81	1.81-1.82	1.81-1.82	1.795	1.780-1.803	
B1-B3	1.79	1.79	1.81	1.779	1.777-1.795	
B3-Mg	2.51	2.52	2.58	2.575	2.559	
B1-Mg	2.54	2.5	2.62	2.591	2.572	
H5-Mg	1.95	1.97	1.96	1.99	1.91	
H6-Mg	1.97	1.99	1.99	2.01	1.98	
Mg-O	2.1	2.12	2.1			2.093
H5-B1	1.22	1.22-1.23	1.23-1.24	1.17	1.14-1.19	

Table S3: *Calculated energies of molecular or complexes at the MP2 level. All values are expressed in Hartree.*

Molecular/complex	**Energy (Hartree)**
THF	-231.7338875
Me_2O	-154.5518258
Et_2O	-232.9264952
$Mg(B_3H_8)_2$	-357.6679207
$Mg(B_3H_8)_2(THF)_2$	-821.2220657
$Mg(B_3H_8)_2(Me_2O)_2$	-666.8475019
$Mg(B_3H_8)_2(Et_2O)_2$	-823.5982098

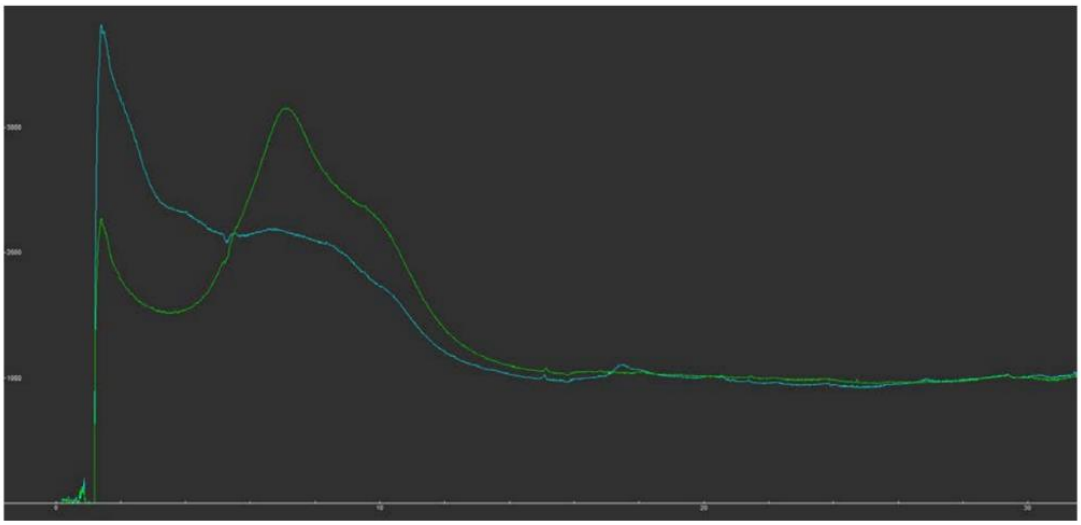

Figure S1: Diffuse scattering from sample right after amorphization (green) and after 8 hours at 180 ^oC (light blue)

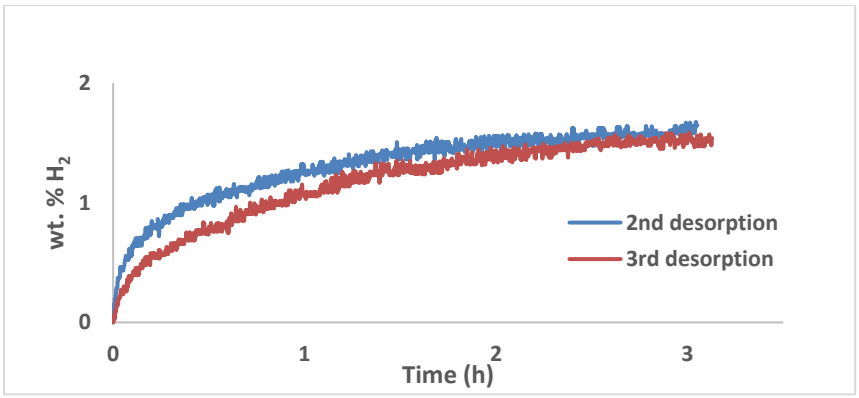

Figure S2: Overlay of 2nd and 3rd dehydrogenation reaction, extracted from PCT cycling data (Figure 5.5)

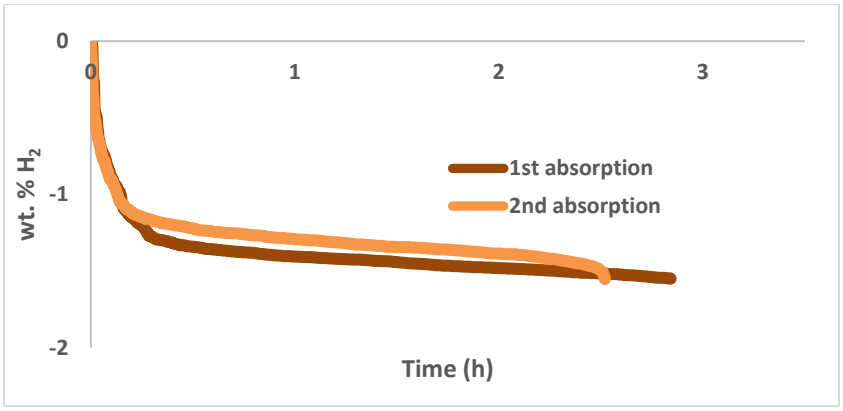

Figure S3: Overlay of 1st and 2nd re-hydrogenation reaction, extracted from PCT cycling data (Figure 5.5)

a)

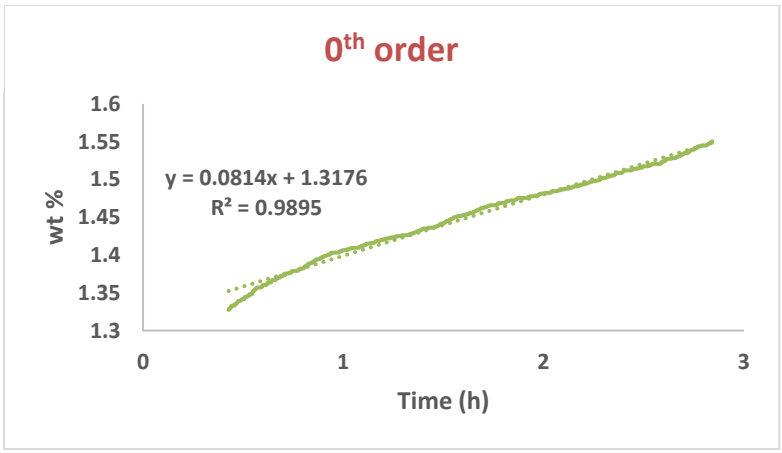

b)

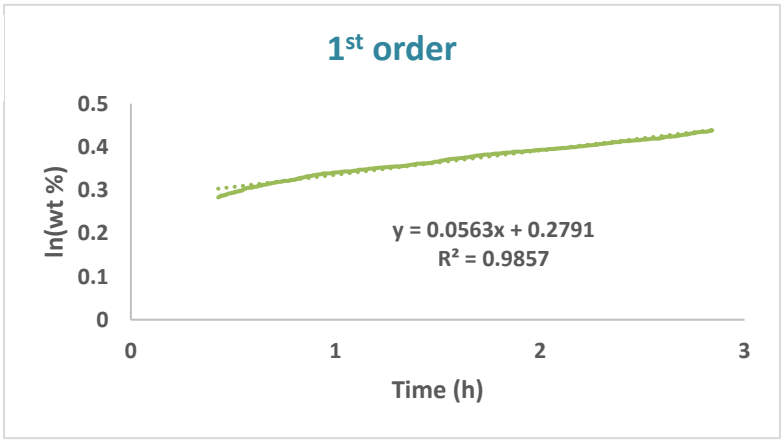

c)

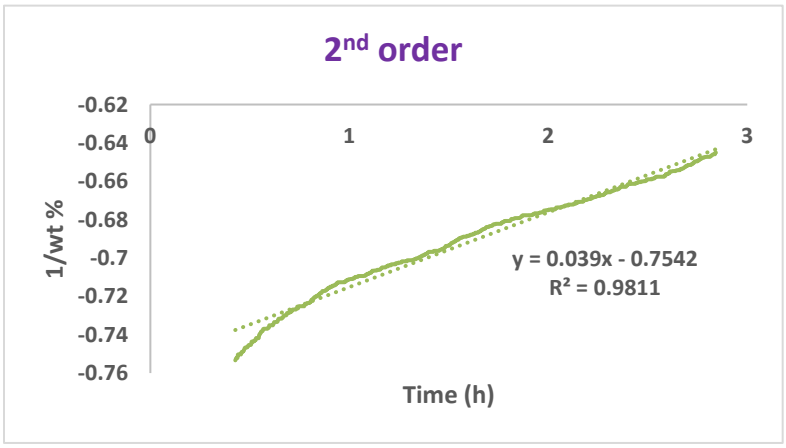

Figure S4: Order of the reaction – 1st absorption

a)

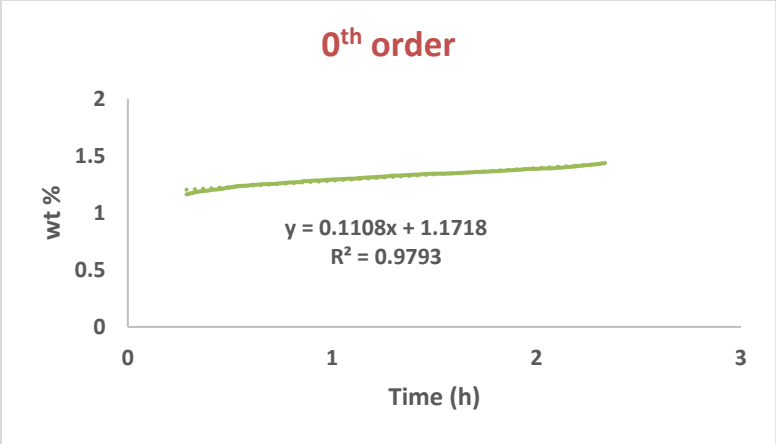

b)

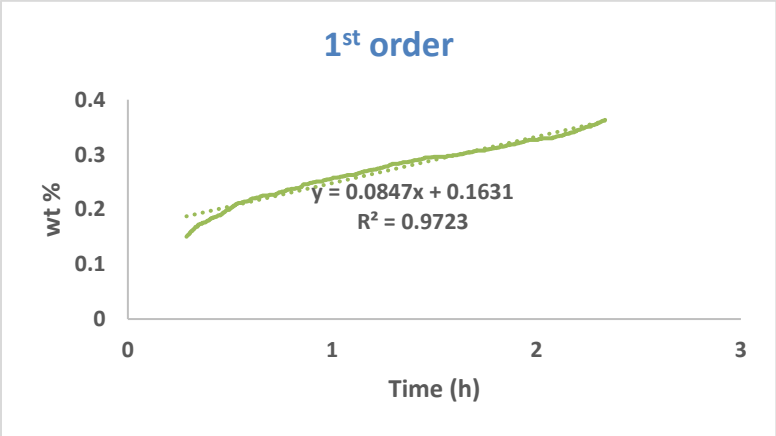

c)

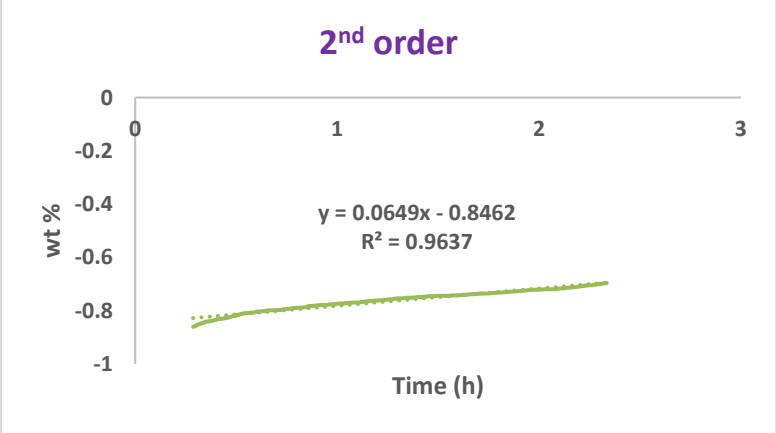

Figure S5: Order of the reaction – 2nd absorption

a)

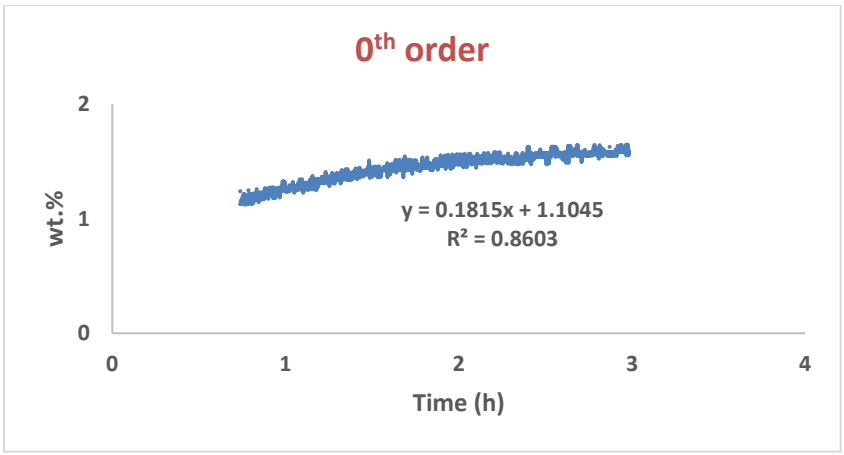

b)

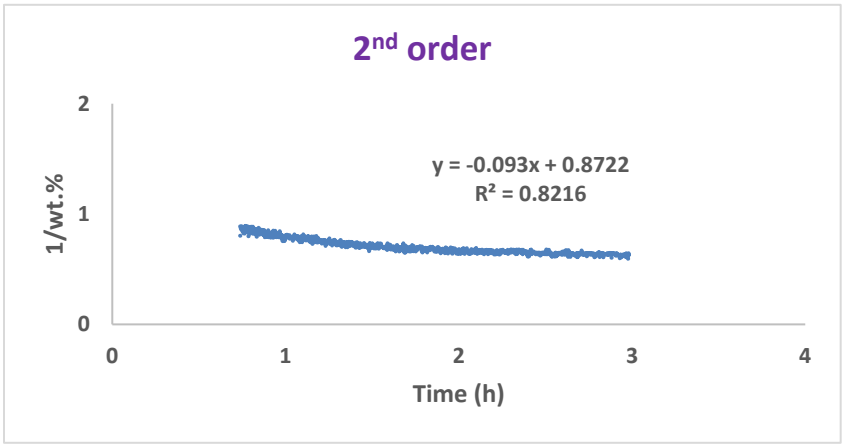

c)

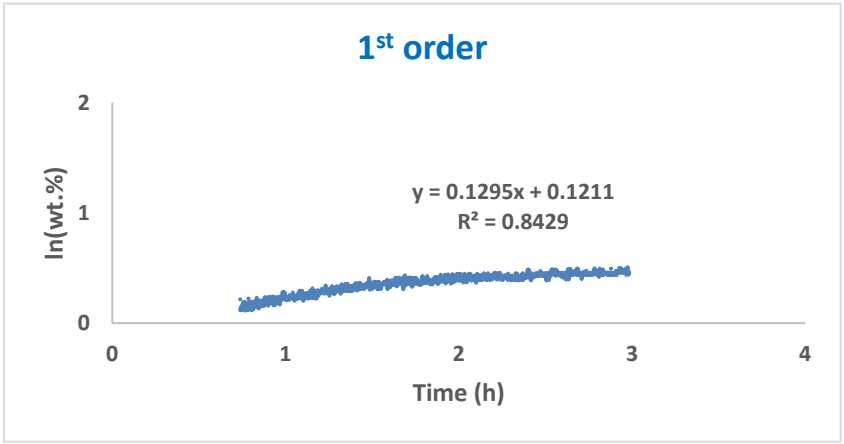

Figure S6: Order of the reaction – 2nd desorption

a)

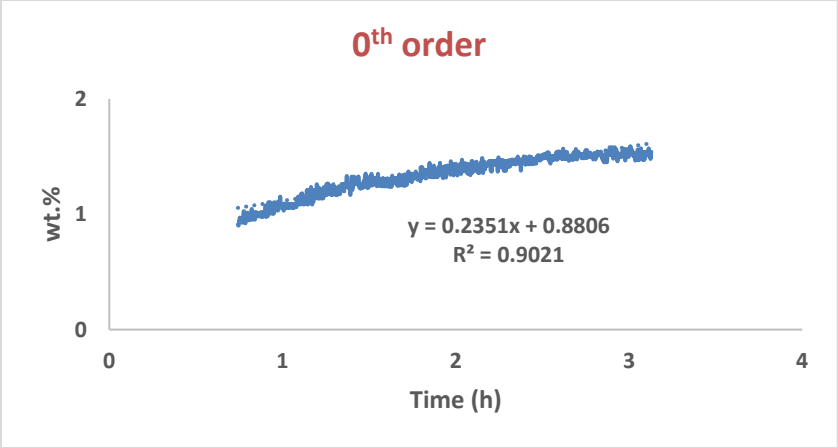

b)

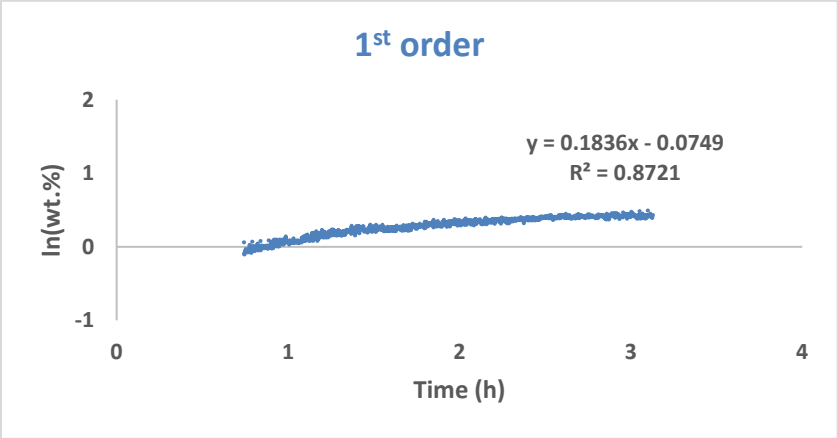

c)

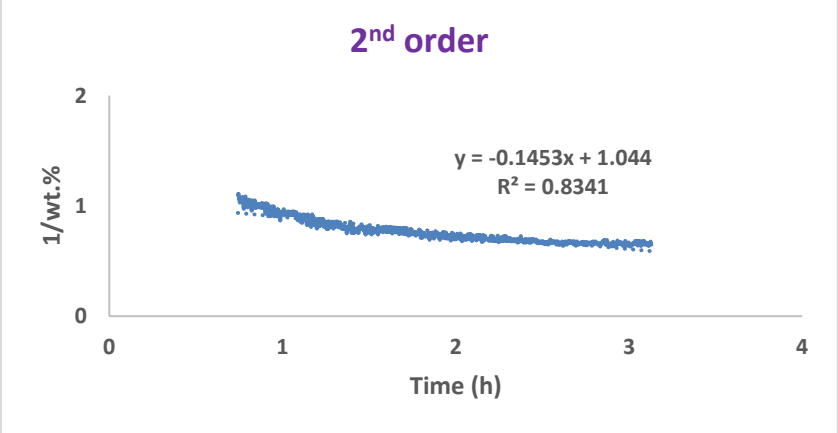

Figure S7: Order of the reaction – 3rd desorption

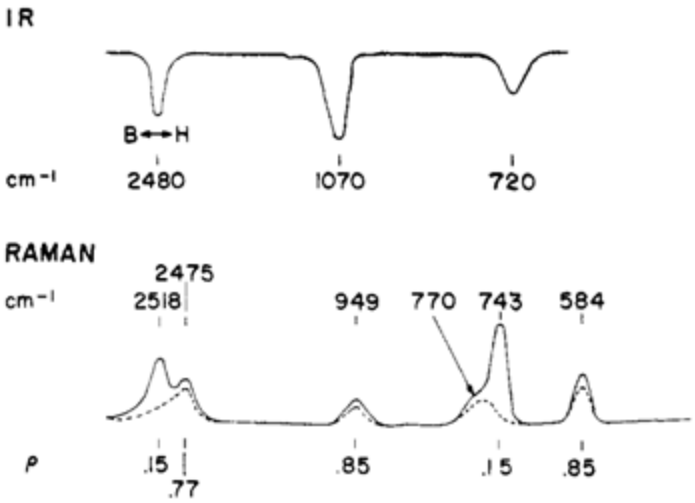

Figure S8: IR and Raman spectra of $B_{12}H_{12}^{2-}$ reproduced from reference 133

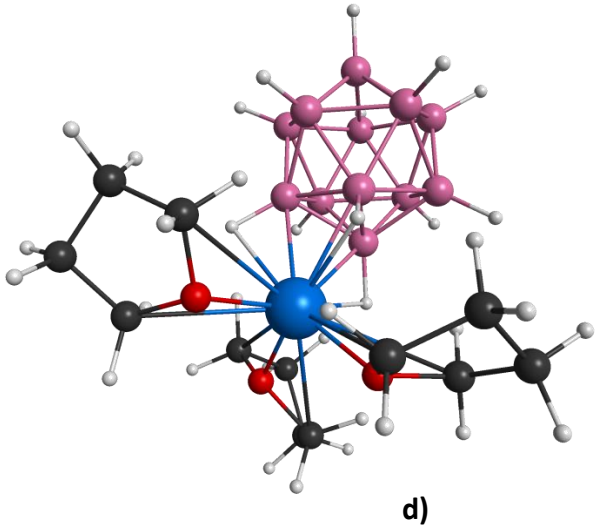

Figure S9: Optimized structure of $MgB_{12}H_{12}(THF)_3$

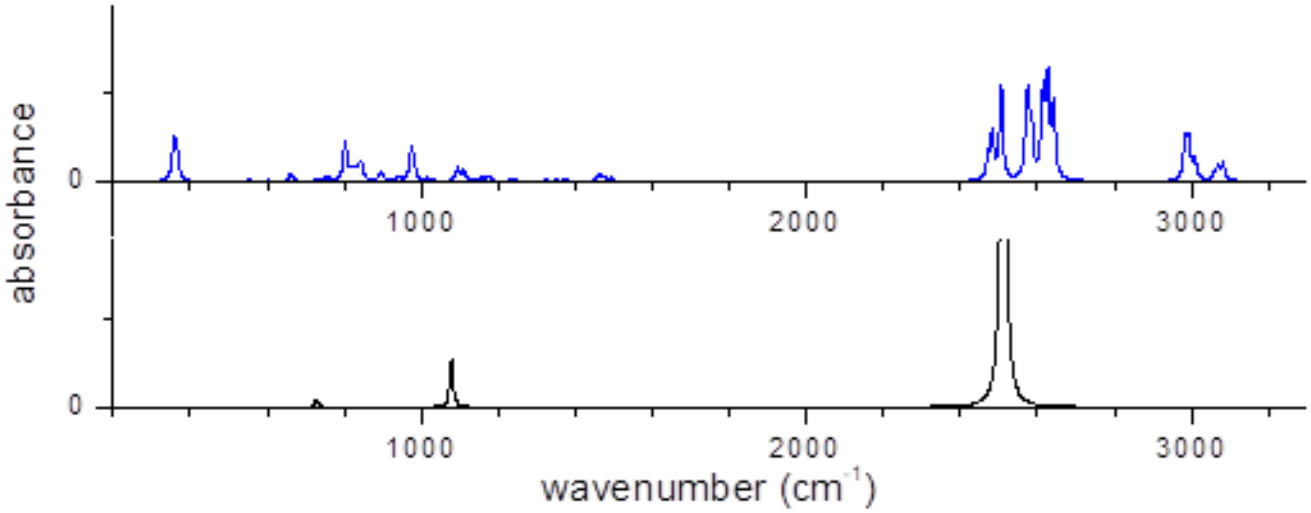

Figure S10: Calculated IR absorption spectrum of isolated $B_{12}H_{12}^{2-}$ (black) and $MgB_{12}H_{12}(THF)_3$ (blue)

Table S4: *Character table, C_{3v} point group*

C_{3v}	E	$2C_3$	$3\sigma_v$			
A_1	1	1	1	z	x^2+y^2, z^2	$z^3, x(x^2-3y^2)$
A_2	1	1	−1	R_z		$y(3x^2-y^2)$
E	2	−1	0	$(x, y), (R_x, R_y)$	$(x^2-y^2, xy)(xz, yz)$	$(xz^2, yz^2), [xyz, z(x^2-y^2)]$
$\Gamma_{x,y,z}$	3	0	1			

REFERENCES

1. BP Statistical Review of World Energy 2016 http://www.bp.com/content/dam/bp/pdf/energy-economics/statistical-review-2016/bp-statistical-review-of-world-energy-2016-full-report.pdf
2. International Energy Outlook 2017 https://www.eia.gov/outlooks/ieo/
3. Global Climate Change Indicators https://www.ncdc.no0061a.gov/monitoring-references/faq/indicators.php
4. Hydrogen Storage https://energy.gov/eere/fuelcells/hydrogen-storage
5. Hydrogen Fuel Cells https://www.energy.gov/sites/prod/files/2015/11/f27/fcto_fuel_cells_fact_sheet.pdf
6. Type of Fuel Cells https://energy.gov/eere/fuelcells/types-fuel-cells
7. Springer, *PEM Fuel Cells with Bio-Ethanol Processor Systems*, London, **2012**
8. Borup, R.; Myers, D.; Wilson, M.; Garzon, F.; Wood, D.; Zelenay, P.; More, K.; Stroh, K.; Zawodzinski, T.; Boncella, J.; McGrath, J. E.; Inaba, M.; Miyatake, M.; Hori, M.; Ota, K.; Ogumi, Z.; Miyata, S.; Nishikata, A.; Siroma, Z.;Uchimoto, Y.; Yasuda, K.; Kimijima, K.; Iwashita, N. *Chem. Rev.* **2007**, *107*, 3904
9. U.S. Department of Energy: Hydrogen Storage Targets https://energy.gov/eere/fuelcells/doe-technical-targets-onboard-hydrogen-storage-light-duty-vehicles
10. Zuttel, A.; Sclapbach, L. *Nature*. **2001**, *414*, *15*

11. California Energy Commission. Compressed Natural Gas (CNG) as a Transportation Fuel: Fact Sheet. http://www.energy.ca.gov/afvs/vehicle fact sheets/cng.html

12. Zuttel, A. *Materials Today*, September, **2003**, 24

13. Niemann, M.U.; Srinivasan, S.S.; Phani, A.R.; Kumar, A.; Goswami, D.Y.; Stefanakos, E.K. *J. Nanomater,* **2008**, *1–9*

14. Yang J.; Sudik, A.; Wolverton, C.; Siegel, D.J. *Chem. Soc. Rev.* **2010**, *39*, *656–75*

15. Züttel, A. *Naturwissenschaften* **2004**, *91*, 157–172.

16. Panella, B.; Hirscher, M. *Adv. Mater.* **2005**, *17(5)*, 538

17. Panella, B.; Hirscher, M.; Putter, H.; Muller, U. *Adv. Funct. Mater.* **2006**, *16(4)*, 520

18. Van den Berg, A. W. C.; Areán, C. O. *Chem. Commun.* **2008**, 668

19. Koh, K.; Wong-Foy, A.G.; Matzger, A.J. *J. Am. Chem. Soc.* **2009**,*131*, 41845

20. Ma, S.; Eckert, J.; Forster, P.M.; Yoon, J.W.; Hwang, Y.K.; Chang, J.-S. *J. Am .Chem. Soc*. **2008**, *130*, 15896–902.

21. Latroche, M.; Surble, S.; Serre, C.; Mellot-Draznieks, C.; Llewellyn, P.L.; Lee, J.-H.; Chang, J.-S.; Jhung, S. H.; Ferey, G. *Angew. Chem. Int. Ed.* **2006**, *45*, 8227–31

22. Walker, G. *Solid State Hydrogen Storage, Materials and Chemistry*, Wood Head, Publishing Limited, USA, **2008**

23. EERE, *Fuel Cell Technologies Program, Hydrogen Storage*, April, **2009.** http://www1.eere.energy.gov/hydrogenandfuelcells/storage/

24. Badwal, S. P. S.; Giddey, S.; Munnings, C., *Wiley Interdisciplinary Reviews: Energy and Environment*, **2013,** *2*, 473-487.

25. Bičáková, O.; Straka, P., *Int. J. Hydrog. Energy*, **2012,** *37*, 11563-1157.

26. Rönnebro, E. C. E.; Majzoub, E. H., *MRS Bulletin*, **2013,** *38*, 452-458

27. Grochala, W.; Edwards, P.P.; *Chem Rev.*, **2004**, *104*, 1283–315.

28. Yang, J.; Sudik, A.; Wolverton, C.; Siegel, D. J., *Chem. Soc. Rev.*, **2010,** *39*, 656-675.

29. Vitalie, S.; Lennie, K.; John, V.; Ping, C., In *Hydrogen Storage Technology: Materials and Applications;* L. Klebanoff, Ed.; Taylor & Francis, **2012**, pp. 133-212

30. EERE, *Hydrogen Storage Technical Team Roadmap*, **2013** http://www1.eere.energy.gov/vehiclesandfuels/pdfs/program/hstt_roadmap_June2013.pdf

31. Orimo, S.; Nakamori, Y.; Kato, T.; Brown, C.; Jensen, C. M., *Appl. Phys. A*, **2006,** *83*, 5-8

32. Walker, G. *Solid State Hydrogen Storage, Materials and Chemistry*, Wood Head Publishing Limited, USA, **2008**

33. EERE, Chemical Hydrogen Storage Materials https://www.energy.gov/eere/fuelcells/chemical-hydrogen-storage-materials

34. Zidan, R.; Garcia-Diaz, B. L; Fewox, C. S.; Stove, A. C.; Gray, J. R.; Harter, A. C. *Chem. Commun.* **2009**, 3717

35. Sandrock, G.; Reilley, J.; Graetz, J.; Zhou, W.-M. Zhou, Johnson, J.; Wegrzyn, J. *Appl. Phys. A*, **2005**, *80*, 687

36. Ashby, E. C. J. *J. Am. Chem. Soc.*, **1964**, *86*, 1882

37. Graetz, J. *J. Phys. Chem. C*, **2007**, *111*, 19148

38. James, B. D.; Wallbridge, M. G. H. *Prog. Inorg. Chem.*, **1970**, *11*, 99–231

39. Zhang, J. S.; Fisher, T. S.; Gore, J. P.; Hazra, D.; Ramachandran, P. V. *Int. J. Hydrog. Energy*, **2006**, *31*, 2292–2298

40. Suryanarayana, C. *Prog. Mater. Sci.* **2001**, *46*, 1–184

41. Shevlin, S. A.; Guo, Z. X., *J. Phys. Chem. C*, **2013,** *117*, 10883-10891

42. Sandrock, G. Compilation of IEA/DOE/SNL Hydride Databases

43. Bobet, J. L.; Even, C.; Nakamura, Y.; Akiba, E.; Darriet, B., *J. Alloys Compd.*, **2000,** *298*, 279-284.

44. Lu, H. B.; Poh, C. K.; Zhang, L. C.; Guo, Z. P.; Yu, X. B.; Liu, H. K., *J. Alloys Compd.*, **2009,** *481*, 152-155.

45. Huot, J.; Liang, G.; Schulz, R. *Appl. Phys. A* **2001**, *19571*, 187–195.

46. Barkhordarian, G.; Klassen, T.; Bormann, R. *Scr. Mater.* **2003**, *49*, 213–217.

47. Gutfleisch, O.; Dal Toè, S.; Herrich, M.; Handstein, A.; Pratt, A. *J. Alloys. Compd.* **2005**, *404-406*, 413–416

48. U.S. Department of Energy Hydrogen Program. Go/no-go recommendation for sodium borohydride for on-board vehicular hydrogen storage. https://www1.eere.energy.gov/hydrogenandfuelcells/pdfs/42220.pdf; 2007. NREL/MP-150e42220.

49. G. Sandrock, *J. Alloys Compd.*, **1999**, *293–295*, 877

50. Bogdanovic, B.; Schwickardi, M. *J. Alloys Compd.* **1997**, *253-254*, 1–9

51. Ashby, E. C.; Kobetz, P. *Inorg. Chem.* **1966**, *5*, 1615

52. Dymova, T. N.; Eliseeva, N. G.; Bakum, S. I.; Dergachev, Y. M. *Dokl. Akad. Nauk SSSR.* **1974**, *215*, 1369

53. Orimo, S.-I.; Nakamori, Y.; Eliseo, J. R.; Züttel, A.; Jensen, C. M. *Chem. Rev.* **2007**, *107*, 4111

54. Chen, P.; Xiong, Z. T.; Luo, J. Z.; Lin, J. Y.; Tan, K. L. *Nature*, **2002**, *420*, 302

55. Nakamori, Y.; Orimo, S. *J. Alloys Compd.*, **2004**, *370*, 271

56. Orimo, S.; Nakamori, Y.; Kitahara, G.; Miwa, K.; Ohba, N.; Towata, S.; Zuttel, A. *J. Alloys Compd*. **2005**, *404*, 427

57. Graham, D. D.; Culnane, L. F.; Sulic, M.; Jensen, C. M.; Robertson, I. M. *J. Alloys Compds.* **2007**, *446-447*, 255

58. Lide, D.R. CRC Handbook of Chemistry and Physics, 88th ed.; CRC Press: Boca Raton, FL, USA, 25 June 2007; ISBN 0-8493-0488-1

59. Block, J.; Gray, A.P. *Inorg. Chem.* **1965**, *4*, 304–305.

60. Chen, J.; Kuriyama, N.; Xu, Q.; Takeshita, H.T.; Sakai, T. *J. Phys. Chem. B* **2001**, *105*, 11214–11220

61. Liu, X.; McGrady, G.S.; Langmi, H.W.; Jensen, C.M. *J. Am. Chem. Soc.* **2009**, *131*, 5032–5033

62. Graetz, J.; Wegrzyn, J.; Reilly, J.J. *J. Am. Chem. Soc.* **2008**, *130*, 17790–17794

63. Graetz, J.; Wegrzyn, J.; Reilly. *J. Am. Chem. Soc.* **2008**, *130*, 17790

64. Ashby, E. C.; Brendel, G. J.; Redman, H. E. *Inorg. Chem.* **1963**, *2*, 499

65. Chen, P.; Xiong, Z.; Luo, J.; Lin, J.; Tan, K. L. *Nature*. **2002**, *420*, 21

66. Schlesinger, H. J.; Brown, H. C. J. Am. Chem. Soc. 1940, 62, 3429

67. Koster, R. *Angew. Chem.* **1957**, *3*, 94

68. Cerny, R.; Filinchuk, Y.; Hagemann, H.; Yvon, K. *Angew. Chem., Int. Ed.* **2007**, *46*, 1

69. Nakamori, Y.; Li, H.; Miwa, K.; Towata, S.; Orimo, S. *Mater. Trans.* **2006**, *47 (8)*, 1898.

70. Jeon, E.; Cho, Y. W. *J. Alloys Compd*. **2006**, *422*, 273.

71. Fedneva, E. M.; Alpatova, V. L.; Mikheeva, V. I. *Russ. J. Inorg. Chem.* **1964**, *9*, 826.

72. Stasinevich, D. S.; Egorenko, G. A. *Russ. J. Inorg. Chem*. **1968**, *13 (3)*, 341.

73. Nakamori, Y.; Miwa, K.; Ninomiya, A.; Li, H.; Ohba, N.; Towata, S.; Züttel, A.; Orimo, S. *Phys. Rev. B* **2006**, *74*, 1

74. Vajo, J. J.; Skeith, S. L. *J. Phys. Chem. B* **2005**, *109*, 3719.

75. Rönnebro, E.; E. Majzoub,E. *J. Phys. Chem. B*, **2007**, *111*, 12045.

76. Kim, J-H.; Jin, S-A.; Shim, J-H.; Cho, Y. W. *Scripta Materialia.* **2008**, *58*, 481

77. Matsunaga, T.; Buchter, F.; Miwa, K.; Towata, S.; Orimo, S.; Züttel, A. *Renew. Energy*, **2008**, *33*, 193.

78. Chlopek, K.; Frommen, C.; Leon, A.; Zabara, O.; Fichtner, M. *J. Mater. Chem.* **2007**. *17*, 349

79. Li, H. W.; Kikuchi, K.; Nakamori, Y.; Ohba, N.; Miwa, K.; Towata, S.; Orimo, S. *Acta. Mater.* **2008**, *56*, 1342.

80. Newhouse, R. J.; Stavila, V.; Hwang, S. J.; Klebanoff, L. E.; Zhang, J. Z. *J. Phys. Chem. C*, **2010**, *114*, 5224.

81. Soloveichik, G. L.; Gao. Y.; Rijssensbeek, J.; Andrus, M.; Kniajanski, S.; Bowman Jr., R. C.; Hwang, S.-J.; Zhao, J.-C. *Int. J. Hydrogen Energy*, **2009**, *34*, 916.

82. Severa, G.; Ronnebro, E.; Jensen, C. M. *Chem. Commun.* **2010**, *46*, 421–423.

83. Chong, M.; Karkamkar, A.; Autrey, T.; Orimo, S.; Jalisatgi, S.; Jensen, C. M. *Chem. Commun*. **2011**, *47*, 1330-1332

84. Zhang, Y.; Majzoub, E.; Ozolins, V.; Wolverton, C. *J. Phys. Chem. C* **2012**, *116*, 10522–10528

85. Li, H.-W.; Miwa, K.; Ohba, N.; Fujita, T.; Sato, T.; Yan, Y.; Towata, S.; Chen, M. W.; Orimo, S. *Nanotechnology* **2009**, *20*, 204013

86. Newhouse, R. J.; Stavila, V.; Hwang, S.-J.; Klebanoff, L. E.; Zhang, J. Z. *J. Phys. Chem. C* **2010**, *114*, 5224-5232.

87. Chong, M.; Matsuo, M.; Orimo, S.; Autrey, T.; Jensen, C.M. *Inorg. Chem.* **2015**, *54*, 4120–4125

88. Nakamoto, K. *Infrared and Raman spectra of inorganic and coordination compounds, part A: theory and applications in inorganic chemistry*. 5th ed. New York: J. Wiley and Sons Inc.; **1997**

89. Kim, D. Y.; Yang, Y.; Abelson, J.R.; Girolami, G.S. *Inorg. Chem.* **2007**, 46, 9060

90. Hermanek, S.; Plesek, J. Collect. Czech. *Chem. Commun.* **1966**, *31*, 177-89

91. Titov, L. V.; Levicheva, M. D.; Psikha, S. B. *Zh. Neorg. Khim.* **1984**, *29*, 668

92. Bykov, A.Y.; Zhizhin, K.Y.; Kuznetsov, N.T.; *Russ. J. Inorg. Chem.* **2014**, *59*, 1539.

93. Dunbar, A.C.; Macor, J.A.; Girolami, G.S. *Inorg. Chem.* **2014**, *53*, 822

94. Hildebrandt, S.J.; Gaines, D.F.; Calabrese, J.C. *Inorg. Chem.* **1978**, *17*, 790

95. Serrar, C.; Es-Sofi, A.; Boutalib, A.; Ouassas, A.; Jarid, A. *J. Phys. Chem. A* **2001**, *105*, 9776.

96. Serrar C.; Es-Sofi, A.; Boutalib, A.; Ouassas, A.; Jarid, A. *Inorg. Chem.* **2000**, *39*, 2224

97. Palumbo, O.; Cantelli, R.; Paolone, A.; Jensen, C.M.; Srinivasan, S.S. *J. Phys. Chem. B* **2005**, *109*, 1168

98. Paolone, A.; Vico, F.; Teocoli, F.; Sanna, S.; Palumbo, O.; Cantelli, R., Knight, D. A.; Teprovich Jr., J. A.; Zidan, R. *J. Phys. Chem. C* **2012**, *116*, 16365

99. Fichtner, M.; Chlopek, K.; Longhini, M.; Hagemann, H. *J. Phys. Chem. C* **2008**, *112*, 11575

100. Hanwell, M.D.; Curtis, D.E.; Lonie, D.C.; Vandermeersch, T.; Zurek, E.; Hutchison, G.R.; *J. Cheminformatics*, **2012**, *4*, 17.

101. Schmidt, M.W.; Baldridge, K.K.; Boatz, J.A.; Elbert, S.T.; Gordon, M.S.; Jensen, J.H.; Koseki, S.; Matsunaga, N.; Nguyen, K. A.; Su, S.; Windus, T. L.; Dupuis, M.; Mongomery Jr, J. A. *Comput. Chem.* **1993**, *14*, 1347

102. Bode, B.M.; Gordon, M.S. *J. Mol. Graph. Model* **1998**, *16*, 133

103. Serrar, C.; Es-sofi, A.; Boutalib, A.; Ouassas, A.; Jarid, A. *J. Phys. Chem. A* **2001**, *105*, 9778

104. Guggenberger, L.J. *Inorg. Chem.* **1970**, 368

105. Mitchell, G.F.; Welch, A.I. *J. Chem. Soc. Dalton Trans.* **1987**, 1017

106. Serrar, C.; Es-Sofi, A.; Boutalib, A.; Ouassas, A.; Jarid, A. *Inorg. Chem.* **2000**, *39*, 2224

107. Shurvell, H.F.; Southby, M.C. *Vib. Spectrosc.* **1997**, *15*, 137

108. Fu, H.; Wang, X.; Shao, Y.; Chen, J.; Zhang, X.; Fu, H.; Zheng, J.; Li, X. *Int. J. Hydrog. Energy* **2016**, *41*, 384.

109. Carbonniere, P.; Hagemann, H. *J. Phys. Chem. A* **2006**, *110*, 9927

110. Paolone, A.; Teocoli, F.; Sanna, S.; Palumbo, O.; Autrey, T. *J. Phys. Chem. C* **2013**, *117*, 729

111. Huang, J.; Yan, Y.; Remhof, A.; Zhang, Y.; Rentsch, D.; Au, Y.S.; de Jongh, P.E.; Cuevas, F.; Ouyang, L.; Zhu, M.; Zuttel, A. *Dalton Trans.* **2016**, *45*, 3687

112. Matsunaga, T.; Buchter, F.; Mauron, P.; Bielman, M.; Nakamori, Y.; Orimo, S.; Ohba, N.; Miwa, K.; Towata, S.; Züttel, A. *J. Alloys Compd.* **2008**, *459*, 583

113. Riktor, M.D.; Sørby, M.H.; Chłopek, K.; Fichtner, M.; Buchter, F.; Züttel, A.; Hauback, B.C. *J. Mater. Chem.* **2007**, *17*, 4939–4942

114. Ozolins, V.; Majzoub, E. H.; Wolverton, C. *J. Am. Chem. Soc.* **2009**, *131*, 230.

115. Hwang, S.-J.; Bowman Jr. R. C.; Reiter, J. W.; Rijssenbeek, J.; Soloveichik, G. L.; Zhao, J.-C.; Kabbour, H.; Ahn, C. C. *J. Phys. Chem. C.* **2008**, *112*, 3164

116. Kim, K. C.; Allendorf, M. D.; Stavila, V.; Sholl, D. S. *Phys. Chem. Chem. Phys.* **2010**, *12*, 9918.

117. Pitochelli, A. R.; Hawthorne, M. F. *J. Am. Chem. Soc.* **1960**, *82*, 3228.

118. Shore, S. *Pure Appl. Chem.* **1977**, *49*, 717

119. Talalaeva, T. V.; Tsareva, G. V.; Simonov, A. P.; Kocheskov, K. A. *Bull. Acad. Sci. USSR, Div. Chem. Sci.* **1964**, *13*, 595

120. Chong, M.; Autrey, T.; Jensen, C. M. *Inorganics*, **2017**, *5*, 89

121. Zanella, P.; Crociani, L.; Masciocchi, N.; Giunchi, G. *Inorg. Chem.*, **2007**, *46*, 9039

122. Hanada, N.; Chlopek, K.; Frommen, C.; Lohstroh, W.; Fichtner, M. *J. Mater. Chem.*, **2008**, *18*, 2611

123. Muetterties, E. L.; Balthis, J. H.; Chia, Y. T.; Knoth, W. H. *Inorg. Chem.* **1964**, *3*, 444

124. Stavila, V.; Her, J. H.; Zhou, W.; Hwang, S. J.; Kim, C.; Ottley, L. A. M.; Udovic, T. J.; *J. Solid State Chem.*, **2010**, *183*, 1133.

125. Verdal, N.; Zhou, W.; Stavila, V.; Her, J. H; Yousufuddin, M.; Yildirim, T.; Udovic, T. J. *J. Alloys Compd.*, **2011**, *509*, S694

126. Paskevicius, M.; Ley, M. B.; Sheppard, D. A.; Jensen, T. R.; Buckley, C. E. *Phys. Chem. Chem. Phys*. **2013**, *15*, 19774

127. Wegner, W.; Jaron, T.; Dobrowolski, M.A.; Dobrzycki, Ł.; Cyranski, M.K.; Grochala, W. *Dalton Trans.* **2016**, *45*, 14370

128. This study, chapter 4

129. Sugai, C.; Kim, S.; Severa, G.; White, J. L.; Leick, N.; Martinez, M. B.; Gennett, T.; Stavilla, V.; Jensen, C. M. *Chem. Phys. Chem.* **2019**, *20*, 1301

130. Chen, X.; Liu, Y.-H.; Alexander, A.-M.; Gallucci, J. C.; Hwang, S.-J.; Lingam, H. K.; Huang, Z.; Wang, C.; Li, H.; Zhao, Q.; Ozkan, U. S.; Shore, S. G.; Zhao, J.-C. *Chem. Eur. J.* **2014**, *20*, 7325

131. Remhof, A.; Yan, Y.; Rentsch, D.; Borgschulte, Jensen, C. M.; Zuttel, A. *J. Mater. Chem. A* **2014**, *2*, 7244

132. He, L.; Li, H.-W.; Tumanov, N.; Filinchuk, Y.; Akiba, E. *Dalton Trans.* **2015**, *44*, 15882

133. Muetterties, E. L.; Merrifield, R. E.; Miller, M. C.; Knoth, W. H.; Downing, J. R. *J. Am. Chem. Soc.* **1962**, *84*, 2506

134. Grimme, S. *J. Comput. Chem.* **2006**, *27*, 1787; Becke, A. D. *J. Chem. Phys.* **1993**, *98*, 5648; Møller, C.; Plesset, M. S. *Phys. Rev.* **1934**, *46*, 618.

135. Schlesinger, H. I.; Brown, H. C.; Finholt, A. E. *J. Am. Chem. Soc.* **1953**, *75*, 205